ABSTRACT

Title of Document:	A STUDY OF HEAT TRANSFER AND FLOW CHARACTERISTICS OF RISING TAYLOR BUBBLES
	Alexander David Scammell, Ph.D. Mechanical Engineering, 2016
Directed By:	Professor Jungho Kim, Department of Mechanical Engineering

Practical application of flow boiling to ground- and space-based thermal management systems hinges on the ability to predict the system's heat removal capabilities under expected operating conditions. Research in this field has shown that the heat transfer coefficient within two-phase heat exchangers can be largely dependent on the experienced flow regime. This finding has inspired an effort to develop mechanistic heat transfer models for each flow pattern which are likely to outperform traditional empirical correlations. As a contribution to the effort, this work aimed to identify the heat transfer mechanisms for the slug flow regime through analysis of individual Taylor bubbles.

An experimental apparatus was developed to inject single vapor Taylor bubbles into co-currently flowing liquid HFE 7100. The heat transfer was measured as the bubble rose through a 6 mm inner diameter heated tube using an infrared thermography technique. High-speed flow visualization was obtained and the bubble film thickness measured in an adiabatic section. Experiments were conducted at various liquid mass fluxes (43-200 kg/m^2s) and gravity levels (0.01g-1.8g) to characterize the effect of bubble drift velocity

on the heat transfer mechanisms. Variable gravity testing was conducted during a NASA parabolic flight campaign.

Results from the experiments showed that the drift velocity strongly affects the hydrodynamics and heat transfer of single elongated bubbles. At low gravity levels, bubbles exhibited shapes characteristic of capillary flows and the heat transfer enhancement due to the bubble was dominated by conduction through the thin film. At moderate to high gravity, traditional Taylor bubbles provided small values of enhancement within the film, but large peaks in the wake heat transfer occurred due to turbulent vortices induced by the film plunging into the trailing liquid slug. Characteristics of the wake heat transfer profiles were analyzed and related to the predicted velocity field. Results were compared and shown to agree with numerical simulations of colleagues from EPFL, Switzerland.

In addition, a preliminary study was completed on the effect of a Taylor bubble passing through nucleate flow boiling, showing that the thinning thermal boundary layer within the film suppressed nucleation, thereby decreasing the heat transfer coefficient.

A STUDY OF HEAT TRANSFER AND FLOW CHARACTERISTICS OF RISING TAYLOR BUBBLES

By

Alexander David Scammell

Dissertation submitted to the Faculty of the Graduate School of the
University of Maryland, College Park, in partial fulfillment
of the requirements for the degree of
Doctor of Philosophy
2016

Advisory Committee:
Professor Jungho Kim, Chair
Professor Christopher Cadou, Dean's Representative
Professor Marino di Marzo
Professor Kenneth Kiger
Professor Amir Riaz

ACKNOWLEDGEMENTS

Throughout my formative educational years, and in particular my pursuit of a Ph.D., there have been many who have influenced, inspired, and supported me. First, I would like to thank my advisor Prof. Jungho Kim, whose constant motivation and encouragement were crucial in my development as an engineer and researcher. As the author Richard Rhodes said, great academic mentors guide their students in, “learning the feel of proof; learning judgement; learning which hunches to play; learning which stunning calculations to rework, which experimental results not to trust.” Prof. Kim has worked to instill these qualities in me, and I am sincerely grateful for it.

I am also indebted to the incredible opportunities and financial support provided by NASA through the Space Technology Research Fellowship program. My fellowship allowed me to travel to 6 countries, attend numerous highly informative conferences, build a network of colleagues, and accrue experiences that will not soon be forgotten. I am greatly appreciative of the influence of Mr. John McQuillen, who not only served as my grant monitor, but as a mentor during my affiliation with NASA.

On a daily basis, no one had a larger effect on me and my work than my lab mates at UMD. In particular, Valentin and Pedro provided endless support, fruitful discussions, and entertainment along the way. I am also grateful for the many colleagues I have had the pleasure of working with, especially Mirco, Esli, Dong, Marine, Balazs, and Prof. Colin.

Finally, I thank my family for their unconditional love and support through this journey. My parents, Cindy and Jonathan, inspired me from a young age to pursue a career in science and have worked tirelessly to provide my siblings and I every opportunity to follow our

dreams. I will be ever thankful to my sister, Emily, for being an example of personal drive and determination; and to my brother, Adam, who reminds me to never take life too seriously.

TABLE OF CONTENTS

Acknowledgements ii

Table of Contents iv

List of Figures vi

List of Tables xi

Nomenclature xii

Chapter 1: Introduction 1

1.1 Background/Motivation 1

1.2 Microgravity Research 3

1.3 Single Elongated Bubble Research 7

1.3.1 Taylor Bubble Hydrodynamics 9

1.3.2 Taylor Bubble Heat Transfer 14

1.3.3 Capillary Bubble Heat Transfer 15

1.4 Objectives 19

Chapter 2: Experiment Description 20

2.1 Flow Loop 21

2.2 IR Technique 26

2.2.1 Validation 32

2.2.2 Uncertainty analysis 36

2.3 Data Collection 38

Chapter 3: Results and Discussion 42

3.1 Bubble Dynamics 43

3.2 Heat Transfer 51

3.3 Comparison to Numerical Simulations 66

3.3.1 Simulation Parameters 66

3.3.2 Shape and Hydrodynamics Comparison 67

3.3.3 Heat Transfer Comparison 70

3.4 Implications for Slug Flow Model Development 76

Chapter 4: Bubble Effect on Nucleate Boiling 84

Chapter 5: Conclusions 92
5.1 Intellectual Contributions 92
5.1.1 Adaptation of Flow Boiling Experiment 92
5.1.2 Characterization of Elongated Bubbles 93
5.1.3 Taylor Bubble Effect on Nucleate Flow Boiling 94
5.2 Recommendations for Future Work 95
Appendix A: Calibrations and Uncertainty 98
A.1 Uncertainty Overview 98
A.1.1 Bias Uncertainty 99
A.1.2 Random Uncertainty 99
A.1.3 Curve Fitting Uncertainty 100
A.2 Individual Measurement Analyses 100
A.2.1 Temperature 100
A.2.2 Flow 102
A.2.3 Pressure 104
A.2.4 Fluid Properties 104
A.2.5 Film Thickness 105
A.2.6 Optical Properties 110
A.2.7 Effective T_∞ Calibration and Uncertainty 114
A.2.8 Heat Transfer 116
Appendix B: Film Velocity Derivation 119
References 120

LIST OF FIGURES

Figure 1.1: Schematic of common flow boiling regimes for vertical-upward flow within a heated tube: a) bubbly flow, b) slug flow, c) churn flow, and d) annular flow. 2

Figure 1.2: Time trace of heat transfer coefficient and acceleration with corresponding flow visualization images for G=150 kg/m^{2}s. Figure from Ohta [6] (used with permission). 5

Figure 1.3: Diagram describing the liquid flow pattern around a rising Taylor bubble. 8

Figure 1.4: Diagram of velocity profiles ahead of the bubble and in the near wake region in the laboratory (left) and bubble (right) reference frames. 9

Figure 1.5: Wake patterns described by Campos and Carvalho [23]: a) laminar, closed, axisymmetric, toroidal vortex with internal recirculatory flow; b) asymmetric, closed, toroidal vortex; c) open, turbulent vortices. Used with permission. ..13

Figure 1.6**:** Diagram of the three-zone heat transfer model for the elongated bubble regime in microchannels, illustrating a triplet comprised of a liquid slug, an elongated bubble, and a vapor slug (from Thome et al. [40], used with permission). 16

Figure 1.7: Schematic of microchannel slug flow decomposition into adherent film and recirculation region within the liquid slug (from Magnini et al. [42], used with permission). 18

Figure 2.1: Experimental rig in parabolic flight configuration. 21

Figure 2.2: Schematic of rig flow loop. 22

Figure 2.3: Schematic of bubble generation section: flow pattern (left); isometric view with valve handle extension (right). 23

Figure 2.4: Schematic of heat transfer test section. 25

Figure 2.5: Mirrors to provide simultaneous heat transfer measurements and flow visualization (left image), and cross-sectional view of silicon tube with coated polyimide tape (right image). 27

Figure 2.6: Representative IR image showing tube "halves" observed using mirror arrangement. The top half was used for visual observation of the internal flow, while the bottom half allowed for temperature measurements to be made. 28

Figure 2.7: Schematic of silicon tube and tape multilayer showing the thermal gradients present due to heating of the tube and cooling from forced convection and boiling. 29

Figure 2.8: Experimental heat transfer coefficient compared to the Dittus-Boelter correlation with the Al-Arabi correction for the parameters: HFE 7100, Re=5545, T_{sub}=20°C, q"=20 kW/m^2....35

Figure 2.9: Experimental heated wall temperature offset by the liquid inlet temperature as a function of axial length along the tube compared to correlations for mixed convection. The conditions were: G=50 kg/m^{2}s, Re=790, T_{in}=45°C, and q''= of 1.4 kW/m^2 and 2.5 kW/m^2....35

Figure 2.10: Comparison of two-phase data collected by UMD and IMFT with similar experiments at conditions – UMD: G=100 kg/m^{2}s, q''=10 kW/m^2; IMFT: G=100 kg/m^{2}s, q''=9.8-36 kW/m^2 (figure adapted from Narcy et al. [53]). 36

Figure 2.11: Description of parabolic flight campaign: a) NASA C9 aircraft; b) parabolic flight profile (photo and graph courtesy of NASA)....40

Figure 3.1: Bubble velocity as a function of liquid velocity for a/g=0.01, 0.34, 1, and 1.8. 44

Figure 3.2: Images of representative bubbles at varying accelerations and drift velocities: a) a/g = 0.02, U_d = 20 mm/s, Bo = 0.97, L=17 mm; b) a/g = 0.02, U_d = 41 mm/s, Bo = 0.97, L=18 mm; c) a/g = 0.34, U_d = 94 mm/s, Bo = 16.6, L=13 mm; d) a/g = 1, U_d = 106 mm/s, Bo = 48.7, L=13 mm; e) a/g = 1.8, U_d = 214 mm/s, Bo = 87.7, L=13 mm. 46

Figure 3.3: Representative tail profiles for two bubbles rising in co-current flow with U_l=37 mm/s....47

Figure 3.4: Bubble nose profiles at U_d=20, 41, 94, 175, and 214 mm/s. The theoretical profile of Dumitrescu for U_d=81 mm/s is also shown. 47

Figure 3.5: Bubble shape profiles for U_d=20 mm/s (left) and U_d=41 mm/s (right) under microgravity conditions. 49

Figure 3.6: Film thickness at the bubble tail as a function of bubble length at various drift velocities for Taylor bubbles (U_d>94 mm/s). 51

Figure 3.7: Representative heat transfer coefficient profiles: a) capillary bubble (U_d=20 mm/s, U_l=70 mm/s, L_b=16 mm, a/g=0.01, q''=800 W/m^2, h_{SP}=101 W/m^{2}K); b) Taylor bubble (U_d=124 mm/s, U_l=70 mm/s, L_b=14 mm, a/g=1, q''=1440 W/m^2, h_{SP}=148 W/m^{2}K). 53

Figure 3.8: Representative IR images of the near wake region for bubbles presented in Figure 3.7: a) capillary bubble and b) Taylor bubble. 54

Figure 3.9: Scaled heat transfer coefficient as a function of distance behind the bubble tail for bubble drift velocity U_d =163 mm/s, tube heat flux of q"=1.0 kW/m^2, average single-phase heat transfer coefficient h_{SP}=192 W/m^{2}K, and bubble lengths L_b/D=3.2, 4.2, 5, 5.8, and 7.7. 55

Figure 3.10: Representative wake heat transfer signature characteristics identification. ..56

Figure 3.11: Schematic showing high velocity wall jets (red) plunging into the wake. Separation of the jet occurs at the penetration length. Bubble photograph courtesy of Dr. Mirco Magnini. 57

Figure 3.12: Wake heat transfer coefficient contours (left) and representative profiles (right) at a/g=1 for various conditions. 59

Figure 3.13: Wake heat transfer coefficient contours (left) and representative profiles (right) at a/g=1.8 for various conditions. 60

Figure 3.14: Wake vortex frequency as a function of the relative velocity between the film and bulk liquid velocity for a/g=0.34, 1, and 1.8. 62

Figure 3.15: Velocity of vortices as they move away from the bubble tail (fixed reference frame at bubble tail) with respect to bubble velocity at a/g=1.8 and a/g=1. ..63

Figure 3.16: Heat transfer coefficient enhancement as a function of distance behind the bubble tail for a) near-wake region and b) far-wake regions at the conditions: U_d=105, 124, 163, 144, 173, and 208 mm/s; tube heat flux of q''=1400, 1470, 1700, 1140, 1330, and 1320 W/m^2, respectively; average single-phase heat transfer coefficient of h_{SP}=130, 148, 192, 104, 112, and 146 W/m^{2}K, respectively. 65

Figure 3.17: Comparison of representative bubbles under normal gravity conditions with U_l=37 mm/s from: a) experiments (L=17 mm, adiabatic); b) simulations (L=18 mm, q''=1380 W/m^2). Simulation image courtesy of Dr. Mirco Magnini. 68

Figure 3.18: Comparison of measured and simulated film thickness for a short bubble (L_{exp}=14 mm, L_{num}=17 mm) rising within liquid with U_l=37 mm/s at a/g=1. The bubble from which the experimental film thickness was measured is shown above the figure. Numerical data courtesy of Dr. Mirco Magnini. 69

Figure 3.19: Comparison of experimentally measured bubble velocities to those obtained from numerical simulations. Numerical data courtesy of Dr. Mirco Magnini. 70

Figure 3.20: Comparison of wake heat transfer coefficient profiles obtained from experiments and numerical simulations for G=50 kg/m^{2}s, q''=1380 W/m^2, and a/g=1. Numerical data courtesy of Dr. Mirco Magnini. 71

Figure 3.21: Instantaneous flow and temperature field simulated for a bubble with the conditions: G=50 kg/m^{2}s, L/D=6, q''=1380 W/m^2, T_{in}=55.2ºC, T_{sat}=59.5ºC, and a/g=1. Data courtesy of Dr. Mirco Magnini. 74

Figure 3.22: Local heat transfer coefficient plotted as a function of axial position in the wake for the a) left and b) right sides of the cross-section. The averaged bubble parameters were G=50 kg/m^{2}s, L/D=6, q''=1380 W/m^2, T_{in}=55.2ºC, and a/g=1. Data courtesy of Dr. Mirco Magnini. 75

Figure 3.23: Schematic of slug liquid partitioning proposed by Orell and Rembrand [72].....79

Figure 3.24: Schematic of slot injection geometry, adapted from Bittlinger et al. [73]. ...79

Figure 3.25: Heat transfer coefficient profiles for isothermal blowing $T\infty = Tf = 270°C$ for various blowing ratios from Bittlinger et al. [73] (used with permission). Here positive x indicates distance into the wake. 81

Figure 3.26: Comparison of predicted heat transfer coefficient by Seban [74] for slot injection film cooling to experimental results for Taylor bubble wake (experimental conditions: G=200 kg/m^{2}s, a/g=1, q''=1700 W/m^2, h_{SP}=192 W/m^{2}K).....83

Figure 3.27: Comparison of experimentally measured film heat transfer coefficient the correlations of Colburn [68] and Chun & Seban [71]. The conditions were: $Ul = 37$ mm/s, $Ub = 142$ mm/s, $Uf = 851$ mm/s, $Rel = 791$, and q'' = 1370 W/m^2. 83

Figure 4.1: Schematic of initial conditions for single Taylor bubble influence on nucleate boiling tests. 85

Figure 4.2: Heat transfer coefficient as a function of distance from the bubble tail as the bubble passes through nucleate boiling with G=100 kg/m^{2}s and q"=6630, 9520, and 14160 W/m^2. 87

Figure 4.3: Wake heat transfer contours for G=100 kg/m2s and heat fluxes: a) q″=6630 W/m2 and b) q″=9500 W/m2. 88

Figure 4.4: Representative IR image showing the passing of a Taylor bubble where nucleation is present in the liquid film. The testing conditions were G=100 kg/m^{2}s, q''=14160 W/m^2, T_{sub}=2.1 °C.....89

Figure 4.5: Schematic of Taylor bubble rising through nucleate boiling with representative graphs of the measured heat transfer coefficient, wall temperatures, and approximated thermal boundary layer.....90

Figure 4.6: Heat transfer coefficient as a function of distance from the bubble tail as the bubble passes through nucleate boiling with G=185 kg/m^{2}s and q"=9340, 13620, and 18050 W/m^2. 91

Figure A.1: Description of measurement uncertainty categories.....98

Figure A.2: Calibration curves for a) experiment and calibration thermocouples, b) infrared camera. 101

Figure A.3: Calibration data and curve for FLR1009 flowmeter. 103

Figure A.4: Absolute pressure transducer calibration.....104

Figure A.5: Schematic of triangulation technique used by film thickness sensor. 106

Figure A.6: Schematic of parallel calibration setup.....106

Figure A.7: Calibration curve for Keyence film thickness sensor: a) flat configuration and b) angled configuration. 107

Figure A.8: Schematic of angled calibration setup. 108

Figure A.9: Calibration of visual film thickness measurements: a) 0.5 mm grid inserted in tube and submerged with HFE 7100, b) calibration curve relating raw radial position to known grid distances. 109

Figure A.10: Comparison of film thicknesses measured by a Keyence laser displacement sensor and analysis of high-speed visual images. 110

Figure A.11: Experimental setup for multi-layer optical property determination: a) apparent transmissivity measurement, b) apparent reflectivity measurement. 111

Figure A.12: Representative wall temperature profile showing thermal gradients at tube connections. 115

Figure A.13: Bias uncertainty in heat flux as a function of measured heat flux.....117

Figure A.14: Bias uncertainty in heat transfer coefficient as a function of measured heat transfer coefficient. 118

LIST OF TABLES

Table 2.1: Summary of HFE 7100 properties at saturations conditions for 1 bar. 21

Table 2.2: Typical uncertainties for important system parameters and measurements. 26

Table 3.1: Summary of data parameters. 42

Table 3.2: Comparison of measured $U_{b,0}$ to those calculated from published correlations. 44

Table 3.3: Summary of comparative experimental and numerical parameters. 67

Table 4.1: Summary of nucleate boiling test parameters.....85

Table A.1: Summary of important temperature uncertainties. 102

Table A.2: Summary of fluid property uncertainties. 105

Table A.3: Uncertainties associated with optical property determination. 114

NOMENCLATURE

General

Symbol	Definition	Units
C	velocity drift constant	[-]
D	tube diameter	[mm]
g	gravitational acceleration	[m/s^2]
G	liquid mass flux	[kg/m^2s]
h	heat transfer coefficient	[W/m^2K]
h_{lv}	latent heat of vaporization	[MJ/kg]
k	thermal conductivity	[W/m-K]
L	length	[mm]
P	pressure	[bar]
q''	heat flux	[W/m^2]
r	radial position	[mm]
R	tube radius	[mm]
T	temperature	[°C]
U	velocity	[mm/s]
x	vapor quality	[-]
z	axial distance	[mm]
Z	length to fully developed film	[mm]

Greek

Symbol	Definition	Units
α	absorptivity	[1/m]
δ	film thickness, uncertainty	[µm,-]
μ	dynamic viscosity	[Pa-s]
ν	kinematic viscosity	[m^2/s]
ρ	density	[kg/m^3]
σ	surface tension	[N/m]

Subscripts

Symbol	Definition
abs	absolute
act	actual
b	bubble
cam	IR camera
d	drift
f	film
l	liquid
meas	measured
p	polyimide, plunging, penetration
sat	saturation
Si	Silicon
SP	single-phase
v	vapor, vortex
0	stagnant conditions

Dimensionless Groups

Symbol	Name	Relationship	Definition
Bo	Bond Number	$\frac{body\ force}{surface\ tension\ force}$	$Bo = \frac{(\rho_l - \rho_v) g D^2}{\sigma}$
Ca	Capillary Number	$\frac{viscous\ force}{surface\ tension\ force}$	$Ca = \frac{\mu U_b}{\sigma}$
Ga	Galileo Number	$\frac{body\ force}{viscous\ force}$	$Ga = \frac{(gD^3)}{v^2}$
Gr	Grashof Number	$\frac{thermal\ body\ force}{viscous\ force}$	$Gr = \frac{g\beta(T_w - T_m)D^3}{v^2}$
N_f	Inverse Viscosity Number	$\frac{body\ force}{viscous\ force}$	$N_f = \frac{(gD^3)^{1/2}}{v}$
Pr	Prandtl Number	$\frac{momentum\ diffusivity}{thermal\ diffusivity}$	$Pr = \frac{c_p \mu}{k}$
Re	Reynolds Number	$\frac{convective\ momentum\ transport}{viscous\ momentum\ transport}$	$Re = \frac{\rho U L}{\mu}$

Acronyms

Symbol	Definition
EPFL	École Polytechnique Fédérale de Lausanne
ID	inner diameter
IR	infrared
NASA	National Aeronautics and Space Administration
PIV	particle image velocimetry
TRL	Technology Readiness Level

CHAPTER 1: INTRODUCTION

1.1 BACKGROUND/MOTIVATION

Flow boiling is a type of heat transfer that combines convective and phase-change characteristics of the working liquid to improve the efficiency of thermal management systems. Traditional single-phase heat exchangers often require high liquid flow rates, and subsequently large pumping power, to effectively cool high power density loads. The addition of boiling to the flow provides significant heat transfer enhancement due to the latent heat of the fluid and convective forces contributed by the vapor. Depending on the mass flow rate, vapor quality (defined as the mass fraction of vapor to total mass flow), and wall heat flux applied, the flow may assume several regimes. The most common flow patterns for vertical-upward flow boiling in a tube are illustrated in Figure 1.1. Bubbly flow (Figure 1.1a) is characterized by small bubbles which are nucleated from the heated tube wall and travel upward with the flow. As more vapor (bubbles) are added downstream, the small bubbles coalesce to form larger vapor plugs that are nearly the diameter of the tube and are separated by liquid slugs. This regime is classified as slug flow (Figure 1.1b). Further increase of the vapor quality leads to churn flow (Figure 1.1c) in which the individual plugs break down into a chaotic and oscillatory column of vapor surrounded by liquid on the wall. Annular flow (Figure 1.1d) is obtained when the shear force exerted by the vapor core becomes strong enough to maintain a steady liquid film on the tube wall.

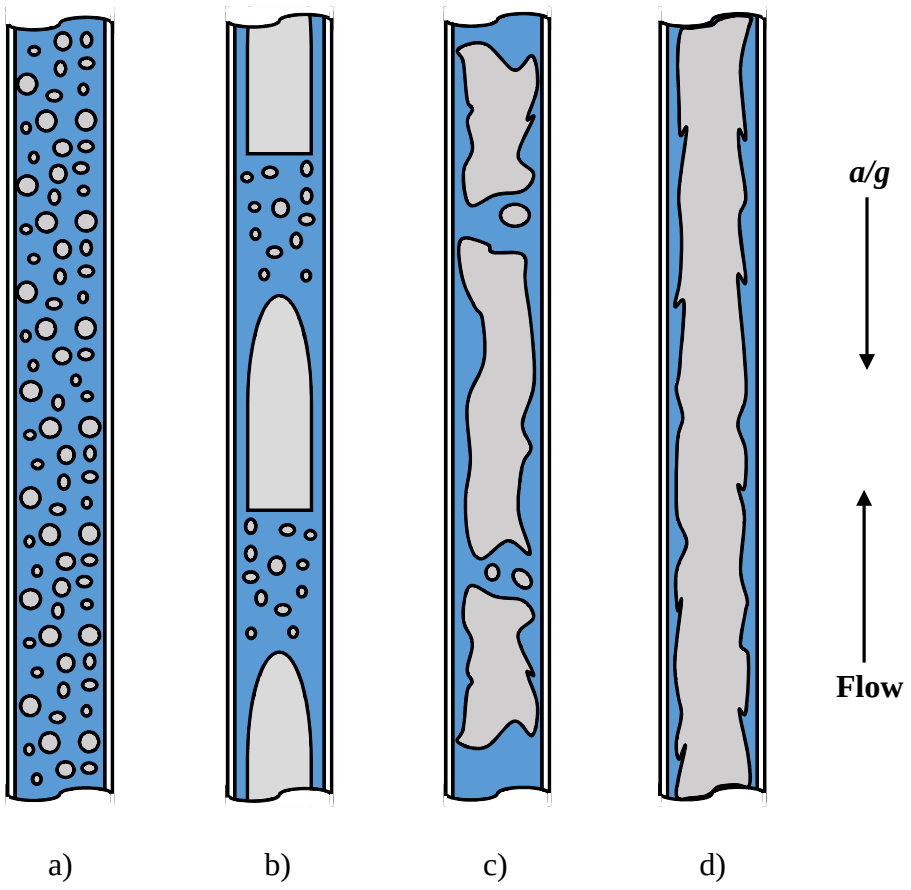

Figure 1.1: Schematic of common flow boiling regimes for vertical-upward flow within a heated tube: a) bubbly flow, b) slug flow, c) churn flow, and d) annular flow.

The study of flow boiling under reduced gravity conditions has gained interest in recent decades due to the growing heat dissipation requirements placed on space-based heat exchanger systems. As one of its top technical challenges, NASA has targeted two-phase heat transfer loops as a way to more efficiently transfer large amounts of heat with little temperature change of the thermal load [1]. An effort to advance the technology readiness level of these systems to TRL 6 will require a more thorough understanding of heat transfer mechanisms in partial or microgravity ($a/g < 0.01$) environments. Thermal control systems can then be designed to utilize two-phase loops as a means to dissipate heat from high power density electronics, while reducing launch weight and volume. To acquire the

necessary understanding and expertise in the field, NASA and other national space agencies have looked to two-phase researchers to study the effect of gravity on flow boiling heat transfer.

1.2 MICROGRAVITY RESEARCH

One of the earliest studies on flow boiling under reduced gravity conditions was by Saito et al. [2]. Their work analyzed the flow of water over a heated rod oriented parallel to the length of a square channel and horizontally with respect to the ground (or aircraft floor). Data collected during parabolic flights illustrated larger bubble departure diameters during the microgravity phase due to the reduction of buoyancy force acting on the bubbles. This acted to decrease the heat transfer coefficient on the underside of the heated rod and increase it on the top. The variation in heat transfer coefficient, however, was fairly small in comparison to the large differences in flow regime.

Around the same time, Lui et al. [3] carried out flow boiling heat transfer experiments with subcooled R113 in a 12 mm ID tubular test section. Heat transfer coefficients were found to increase by 5 to 20% under microgravity conditions, typically increasing with quality. Turbulence caused by greater movement of vapor was given as the reason for the trend. Contradictory results to Lui et al. were found by both Fore et al. [4] and Rite and Rezkallah [5] who conducted experiments on bubbly and slug flows in tubular channels. A decrease in heat transfer coefficient by as much as 50% at microgravity was seen by Rite and Rezkallah at low gas qualities, but the discrepancy between microgravity and normal gravity heat transfer became much smaller as the quality neared annular flow transition. Fore et al. also found lower heat transfer coefficients in microgravity slug and bubbly flow. In both cases, the decrease in heat transfer at low qualities under microgravity conditions

was attributed to the reduction in turbulence behind bubbles, resulting from a smaller relative velocity between the bubbles and liquid (the drift velocity) in the absence of buoyancy force.

Ohta [6] also found the effect of flow dynamics important in his study of R113 evaporation in an 8 mm ID tubular channel. Unlike Fore et al. and Rite and Rezkallah, Ohta observed little difference in heat transfer coefficient for bubbly flow despite much larger microgravity bubble departure diameters at low flow rates (G=150 kg/m^{2}s), as can be seen in Figure 1.2. He asserted that this confirmed the importance of turbulence near the heated wall generated by bubble nucleation, rather than the bubble behavior in the central flow. When nucleation was suppressed, however, as in moderate vapor quality and low to moderate heat fluxes, a variation in heat transfer coefficient with gravity was observed: it was enhanced in high gravity (2g) and decreased in microgravity. It was explained that the frequency and length of the passing disturbance waves in the annular flow pattern increased in the 2g period and decreased in microgravity, leading to a thinning and thickening of the liquid film thickness, respectively. When the wall heat flux was increased under the same quality conditions to the extent that nucleation occurred within the liquid film, Ohta found that the heat transfer coefficient was again unaffected by gravity level.

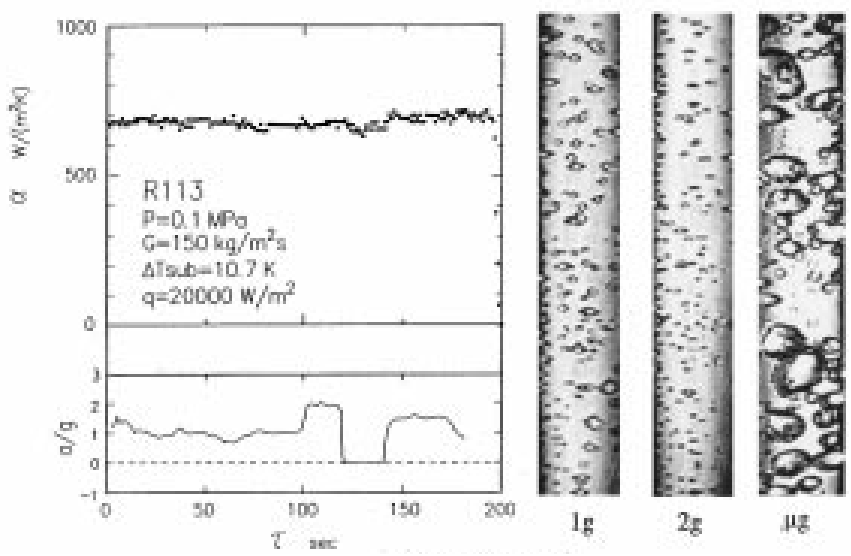

Figure 1.2: Time trace of heat transfer coefficient and acceleration with corresponding flow visualization images for G=150 kg/m^{2}s. Figure from Ohta [6] (used with permission).

The group of Celata and Zummo have completed extensive work on the characterization of microgravity heat transfer and the determination of gravity's mechanistic effects. Utilizing a Pyrex tube heated using a helical resistor, visualization and heat transfer measurements were obtained for boiling FC-72. Early results [7] found that for subcooled boiling at low mass fluxes, a decrease in heat transfer was experienced at microgravity, while for high mass fluxes, no variation was seen. Additionally, it was observed that regardless of mass flux, vapor qualities higher than 0.3 saw little change in heat transfer coefficient between normal and microgravity. The authors suggest that a growth in bubble size in microgravity is typically accompanied by a difference in heat transfer, while similar bubble sizes and distribution lead to negligible difference.

More recently, Zummo et al. [8] found that the variation in tube wall temperature and heat transfer coefficient during the microgravity period depended on the axial measurement location in the tube. They also reiterated their previous findings that above a critical value

of fluid velocity, inertial forces dominate over surface tension and buoyancy forces acting on the bubbles, leading to little change in bubble size with gravity variation. As a result, the turbulence created by the bubbles that disrupt the thermal boundary layer will be similar for all gravity levels, and one should expect that the wall temperature will not be affected.

In agreement with many of the previous works, Narcy et al. [9] found that at high mass fluxes (G > 400 kg/m^{2}s) the flow regime and heat transfer coefficients were unchanged by a variation in gravity level. When the mass flux was reduced to G = 200 kg/m^{2}s, the heat transfer coefficient seemed to be smaller under microgravity conditions than in normal gravity, but further work was suggested. Their experiment consisted of a 6 mm ID sapphire tube heated resistively with a thin indium tin oxide (ITO) coating which allowed for simultaneous heat transfer measurements and high speed flow visualization. After collecting more data, Narcy et al. [10] concluded that for mass fluxes between G = 100 kg/m^{2}s and G = 400 kg/m^{2}s, saturated boiling heat transfer is weakly affected by gravity level. However, they found that at low heat flux and subcooled conditions, the heat transfer coefficient is 20% lower while in a microgravity environment. They theorized that the degradation is caused by lower bubble formation frequency in microgravity.

Narcy and Colin [11] provided further comparison between normal and microgravity heat transfer, noting that at G = 200 kg/m^{2}s and qualities smaller than 0.15, where bubbly and slug flow regimes were present, microgravity heat transfer coefficients were smaller than those in normal gravity. Regardless of quality and flow regime, it was found that a mass flux of G = 50 kg/m^{2}s always yielded a lower heat transfer coefficient in microgravity. They suggested that the nucleate boiling regime remained dominant even when annular flow was present.

While not explicitly commenting the effect of gravity on heat transfer, Westheimer and Peterson [12] found that smaller heat fluxes were needed to cause flow regime transitions in reduced gravity environments. Through observations of boiling R113 in a glass annular heat exchanger, they showed that a flow regime characteristic of higher vapor quality in normal gravity could be seen at a lower quality in microgravity, while maintaining constant flow and heating conditions. This trend has been partly noted in work described above and plays an important role in this proposed study. Specifically, it has been shown in recent years that the variation of heat transfer coefficient with gravity level is likely attributed to differences in flow dynamics and flow regime. This, then, highlights the necessity for two main areas of research important for the prediction of gravity's effect: reduced gravity flow regime maps and mechanistic heat transfer studies for each flow regime. Numerous studies have been conducted to create accurate flow pattern maps under different gravity conditions, and results are strongly influenced by the fluid used as well as the experimental setup. However, of greater need is the determination of the specific heat transfer mechanisms at work for the flow regimes experienced in microgravity conditions. Slug flow is of particular interest for this study.

1.3 SINGLE ELONGATED BUBBLE RESEARCH

Slug flow is characterized by elongated bubbles separated by liquid slugs and can be broken down into "unit cells", each consisting of an individual bubble as shown in Figure 1.3. For the vertical, upward co-current flow configuration, the bubble rises with a velocity (U_b) greater than the liquid (U_l) due to buoyancy and the non-uniform velocity profile present in the tube. The relative velocity between the bubble and liquid can be defined as the drift velocity, $U_d = U_b - U_l$. In order to replace the volume left behind the bubble as

it rises, liquid from the leading slug falls around the bubble, forming a film with thickness δ. The film falls due to gravity and is balanced by the shear force experienced at the tube wall. At the tail, the film plunges as a circular wall jet into the trailing slug creating vortices whose complexity depend on U_d. The bubble shape is dictated by the ratio of buoyancy to surface tension forces as described by the Bond number, $Bo = \frac{(\rho_l - \rho_v) g D^2}{\sigma}$.

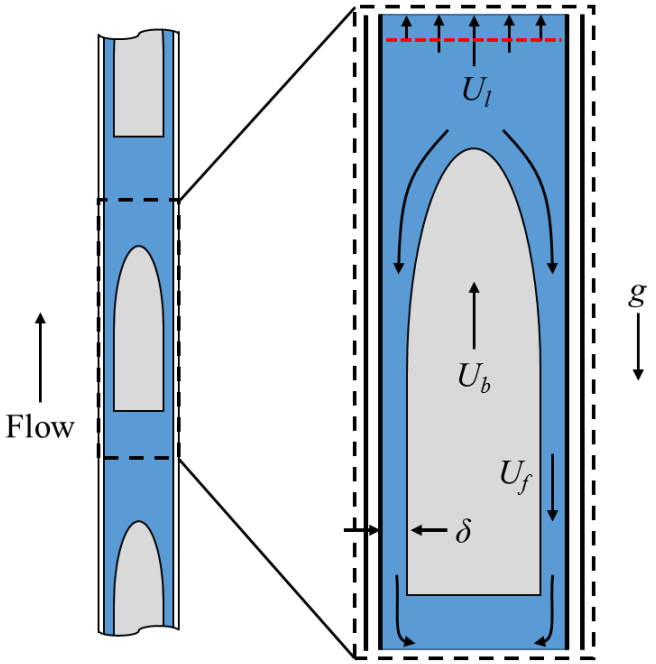

Figure 1.3: Diagram describing the liquid flow pattern around a rising Taylor bubble.

In detailed analysis of the flow field around a bubble, two reference frames can be used: a laboratory reference frame where the bubble rises in a stationary tube and a bubble reference frame which moves with the bubble as shown in Figure 1.4. This assumes the bubble does not grow as it rises in the tube. In this dissertation, unprimed and primed quantities refer to area average velocities in the laboratory and bubble reference frames, respectively. It should be noted that the drift velocity, $U_d = U_b - U_l = U_b' - U_l'$, is

independent of the chosen reference frame as is the plunging velocity, $U_p = U_f + U_l = U_f' - U_l'$. The average film velocity, U_f, can be calculated from a mass balance and the film thickness:

$$U_f = \frac{(U_l - U_b)R^2}{(2R\delta - \delta^2)} - U_b \tag{1}$$

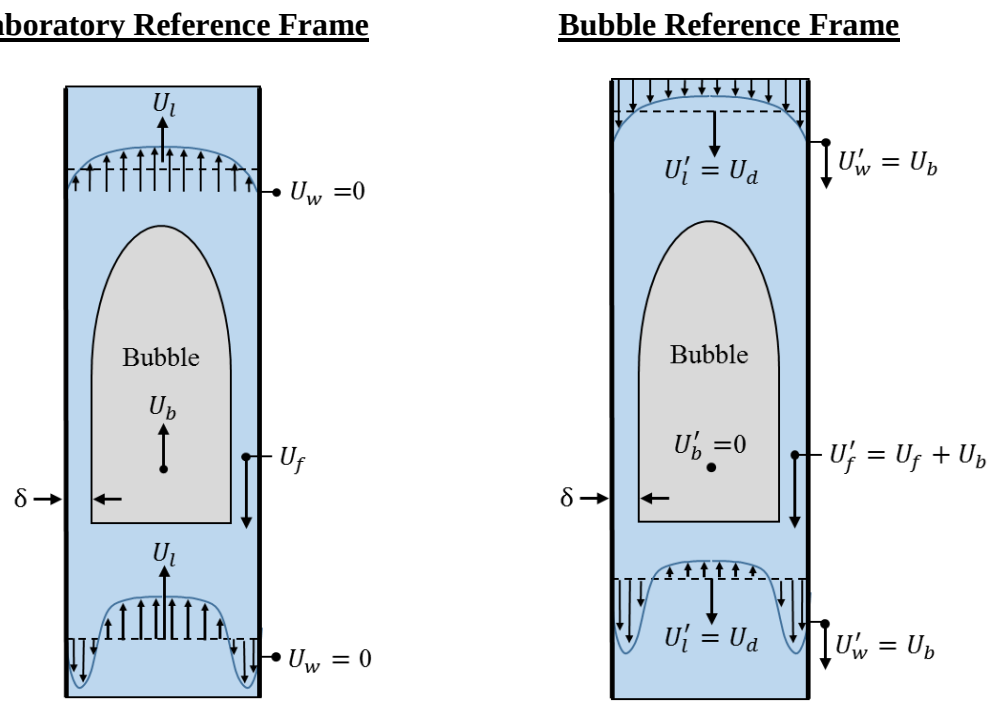

Figure 1.4: Diagram of velocity profiles ahead of the bubble and in the near wake region in the laboratory (left) and bubble (right) reference frames.

1.3.1 Taylor Bubble Hydrodynamics

Bubbles with $Bo > 40$ are considered macroscale [13], exhibit bullet-shaped profiles, and are commonly described as Taylor bubbles (from the early work by Davies and Taylor [14]). Bubbles of this type have been widely studied; a review of the literature prior to 1992

is given in Fabre and Line [15], which summarizes fundamental aspects of the bubble hydrodynamics. Nicklin et al. [16] proposed a correlation for bubble velocity, U_b, of the form,

$$U_b = CU_l + U_{b,0} \tag{2}$$

where C is a constant that defines the bubble rise velocity depending on the fluid velocity profile, and $U_{b,0}$ is the bubble rise velocity in a stagnant fluid column. Values of C were theoretically and experimentally determined to be 2 and 1.2 for a Taylor bubble flowing within fully developed laminar and turbulent flows, respectively [16,17]. White and Beardmore [18] proposed a graphical relation for $U_{b,0}$ based on experimental measurements of air bubbles in a variety of stagnant liquids. Results were broken into several regimes depending on the relative influence of inertial, surface tension, and viscous forces acting on the bubble. Brown [19] modified the potential flow solution for the flow field around rising Taylor bubbles to account for liquid viscosity and developed a correlation that agreed well with experimental results when viscous forces could be ignored at the bubble nose. Viana et al. [13] combined bubble velocity data from the literature with their own data to create a universal correlation for $U_{b,0}$ based on Bo and a buoyancy Reynolds number similar to the Grashof number, Gr. Rattner and Garimella [20] recently completed an experimental study on intermediate scale slug flows and proposed an extension of Bendiksen's [21] prediction for $U_{b,0}$. Polonsky et al. [22] analyzed high speed video of rising Taylor bubbles in air-water vertical flow to characterize the bubble velocity and shape. Oscillations in the bubble tail were found to be of higher frequency and amplitude for longer bubbles.

As the bubble rises, a liquid film is formed between the liquid/vapor interface and the tube wall that thins as it moves towards the tail, eventually reaching a constant thickness

(δ) where the liquid velocity profile within the film has become fully developed. Campos and Carvalho [23] proposed an equation (eqn. (3)) to calculate the distance, *Z*, at which the film stabilizes.

$$\frac{Z}{D} \approx \frac{\left[\left(\frac{g\delta^2}{2v}\right)+U_b\right]^2}{2gD} \tag{3}$$

Nogueira et al. [24] compared experimentally measured values of *Z* to predictions by Campos and Carvalho and found that the agreement was heavily dependent on the measured film Reynolds number, $Re_{U_f} = \frac{U_f \delta}{v}$, where U_f is the mean velocity in the fully developed film. *Z* was underpredicted at film Reynolds numbers below 40, but overpredicted above $Re_{U_f} = 80$.

Prediction of the fully developed film thickness has been the subject of both theoretical and experimental work. Goldsmith and Mason [25] developed a relation for δ by solving the Navier-Stokes equations for a laminar thin film around a Taylor bubble. The thin film assumption was later relaxed by Brown [19] to obtain a similar result (eqn. (4)).

$$\delta = \left[\frac{3v}{2g(R-\delta)}\left((R-\delta)^2 U_b - R^2 U_l\right)\right]^{1/3} \tag{4}$$

Llewellin et al. [26] approximated δ for air bubbles rising in a variety of Newtonian fluids by correlating the bubble volume to its length. It was found that the relative film thickness (δ/R) was solely a function of the non-dimensional parameter $N_f = \frac{\sqrt{gD^3}}{v}$ (this is also equal to the square root of the Galileo number, *Ga*). An empirical correlation was proposed based on their collected data as well as the data of Nogueira et al. [24],

$$\frac{\delta}{R} = a + b\tanh\left(c - d\log_{10} N_f\right) \tag{5}$$

where the constant values are a=0.204, b=0.123, c=2.66, and d=1.15. Rattner and Garimella [20] measured film thickness, bubble velocity, and void fraction for Taylor bubble trains in 6, 8, and 9.5 mm ID tubes using an optical flow visualization facility. Bubble film thicknesses were found to be relatively independent of the liquid flow rates, and depended primarily on the tube diameter. A series of equations was proposed to predict the film thickness for intermediate scale Taylor flows.

At the tail, the liquid film plunges into the liquid slug trailing the bubble creating vortices in the wake whose structures vary in complexity from organized toroids to chaotic shedding. Characterization of the flow field in this region has seen significant progress in recent years due in large part to the advancement of experimental techniques. Campos and Carvalho [23] performed a photographic study of rising air bubbles in stagnant water/glycerol mixtures seeded with dye to determine the structure of the bubble wake. The parameter N_f was varied by adjusting the ratio of water to glycerol. Three wake patterns were identified as shown in Figure 1.5. For $N_f < 500$ (Figure 1.5a) the wake exhibited a laminar, closed, axisymmetric, toroidal vortex with internal recirculatory flow. A transition region occurred for $500 < N_f < 1500$ (Figure 1.5b) where the toroidal vortex remained intact, but became non-axisymmetric due to oscillations in the bubble tail. For $N_f > 1500$ (Figure 1.5c), the vortices in the wake were shed randomly, exhibiting turbulent characteristics that decayed as they moved downstream.

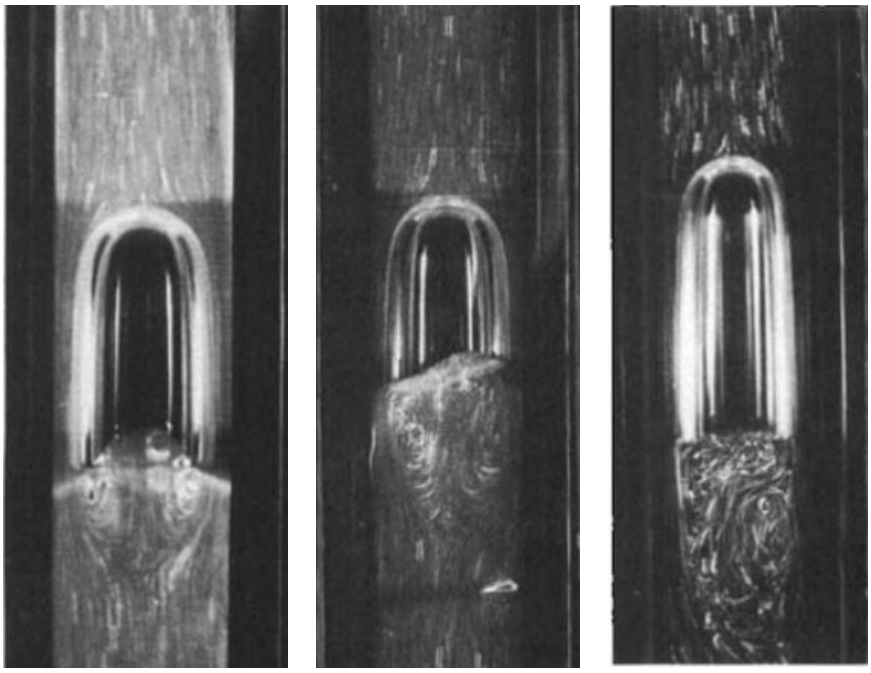

a) b) c)

Figure 1.5: Wake patterns described by Campos and Carvalho [23]: a) laminar, closed, axisymmetric, toroidal vortex with internal recirculatory flow; b) asymmetric, closed, toroidal vortex; c) open, turbulent vortices. Used with permission.

Liu et al. [27] compared these boundaries to wake velocity profiles for vapor bubbles rising in stagnant liquid nitrogen. Results from their particle image velocimetry (PIV) technique revealed that due the significant property differences between water (used by Campos and Carvalho) and liquid nitrogen, the prediction of wake regimes was not applicable to cryogenics. Transitional and laminar wake patterns were observed for $N_f \gg 1500$. Pinto et al. [28] redefined Campos and Carvalho's criteria in terms of a Reynolds number based on the relative velocity between the bubble and liquid, $Re_{U_d} = \frac{\rho_l U_d D}{v}$. They proposed that the wake would be fully turbulent for $Re_{U_d} > 525$ in the case of liquid flowing co-currently with the bubble, but noted that the limit had not been experimentally confirmed.

Kawaji et al. [29] observed turbulent wake characteristics and suggested the vortices were due to a Helmholtz-type instability resulting from the relative velocity difference between the plunging film and the trailing slug. They found that the distance behind the bubble at which the film became unstable (the “penetration length”) remained relatively constant with respect to bubble length once the flow within the film became fully developed.

Shemer et al. [30] used PIV to study the velocity profiles in the wake of single bubbles rising in both laminar and turbulent background flows. They found the wake flow field could be effectively turbulent even when the base flow was laminar. Turbulence quantities calculated from the data showed that the initial mixing process occurred in the near wake region and persisted a few diameters downstream of the bubble tail.

1.3.2 Taylor Bubble Heat Transfer

Hetsroni and Rozenblit [31] briefly touched upon the mechanisms of heat transfer in slug flow. A thin heated film was installed within a 74 mm ID tube and coated with black paint to allow temperature measurement using an IR camera. The wall temperature during the passage of a Taylor bubble was observed to be higher compared to the liquid slug behind the bubble. This suggests a higher heat transfer coefficient in the liquid slug than in the liquid film, but no quantitative data was presented.

Using a similar infrared technique, Babin et al. [32–34] investigated the wake heat transfer enhancement for single air bubbles rising in stagnant and vertically flowing water in 26 and 44 mm ID tubes. They observed that the heat transfer coefficient rose rapidly just behind the bubble tail before decaying to the original single-phase value several hundred diameters downstream. It was also seen that bubbles moving co-currently with turbulent

background flow created smaller heat transfer enhancement compared to those moving in laminar background flow. Heat transfer measurements were compared to PIV velocity measurements obtained by Shemer et al. [30] to show that the growth and decay of velocity fluctuations in the wake may correspond to the heat transfer coefficient profile observed for turbulent background flows.

A model for macroscale gas/liquid slug flow was developed analytically by Barnea and Yacoub [35] in which an energy balance was performed on fluid cross-sections to determine the local wall and fluid temperatures as a function of time. For the case of constant heat flux, the wall temperature was found to be higher during the passing of a liquid slug compared to the liquid film. While this suggests higher heat transfer in the film, it should be noted that the model is based on the absorptive and convective capabilities of each cross-section and not on observed mechanisms.

1.3.3 Capillary Bubble Heat Transfer

The advent of microscale (defined as $Bo < 0.9 - 19.7$ by [18,21,36–38]) heat exchangers has spurred work into the behavior of microchannel slug flow. Slug flow under these conditions is characterized by elongated bubbles, also known as capillary bubbles, with near-spherical caps at the nose and the tail. Several modeling efforts and numerical studies of local heat transfer around capillary bubbles have been completed. A model by Jacobi and Thome [39] featured a two-zone representation of evaporation for elongated bubble flows where the regime was divided into a liquid slug region and a thin film region. It was suggested that the main mechanism of heat transfer was evaporation of the thin film trapped between the bubble and heated channel wall. This model was modified by Thome et al. [40] to include three zones as shown in Figure 1.6: a liquid slug, an evaporating elongated

bubble, and a vapor slug. As with the two-zone model, evaporation in the thin liquid film provided heat transfer several orders of magnitude higher than the single phase heat transfer due to the liquid slug.

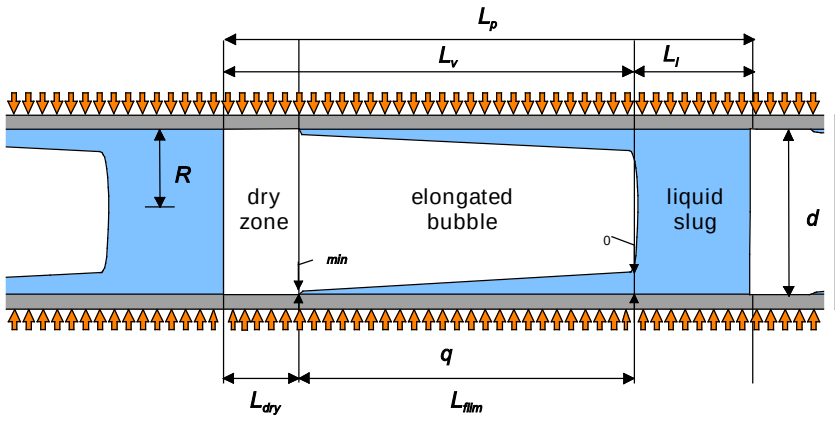

Figure 1.6**:** Diagram of the three-zone heat transfer model for the elongated bubble regime in microchannels, illustrating a triplet comprised of a liquid slug, an elongated bubble, and a vapor slug (from Thome et al. [40], used with permission).

Magnini et al. [41] numerically obtained the shape, length, and local heat transfer of Taylor bubbles during boiling of several fluids in a 0.5 mm circular channel. They found that as the bubble entered a heated channel containing a developing thermal boundary layer, evaporation of the liquid film removed heat from the fluid and caused the heat transfer to become larger than for single-phase flow. The heat transfer coefficient rose monotonically from the bubble nose towards the tail, with the highest values occurring in the bubble wake region. Based on these results, they modified the three-zone model by Thome et al. [40] to include unsteady conduction through the liquid, and obtained better agreement with the simulations.

Extending their previous study, Magnini et al. [42] analyzed the effect of leading and sequential bubbles on evaporating slug flow heat transfer of refrigerants in a 0.5 mm tube. Two bubbles were injected into a thermally-developing flow with constant heat flux boundary conditions applied to the tube wall. It was seen that the growth of the trailing bubble accelerated the leading bubble, but not the liquid within the film around the leading bubble. This increased the difference between liquid film velocity and bubble vapor velocity, thereby promoting local instability at the interface. It is also observed that the average heat transfer for the trailing bubble is nearly twice that observed for single-phase flow and 60% higher than the leading bubble, a result attributed to the re-development of the thermal boundary layer after the first bubble transit and perturbations of the second bubble. The authors created a new model for the heat transfer coefficient, breaking the flow structure into an adherent film, present in the bubble region and the liquid slug, and a recirculating flow within the slug as illustrated in Figure 1.7. A comparison to numerical simulations yielded good agreement when superheating of the liquid slug is taken into account. Many other numerical studies have been conducted on both the hydrodynamics and heat transfer of slug flow in microchannels and have been summarized in a review by Talimi et al. [43].

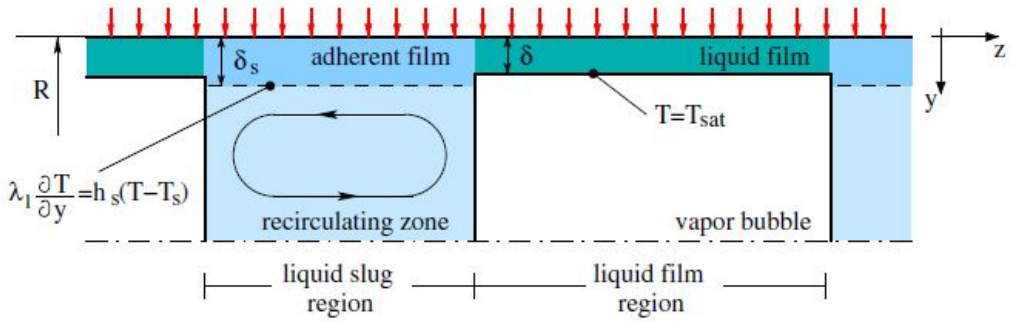

Figure 1.7: Schematic of microchannel slug flow decomposition into adherent film and recirculation region within the liquid slug (from Magnini et al. [42], used with permission).

The experimental heat transfer work to date has largely focused on measuring the overall heat transfer enhancement of slug trains with respect to single phase flow, rather than on the mechanisms of heat transfer around each bubble. For example, Walsh et al. [44,45] utilized an IR technique in which the outer wall temperature of a 1.5 mm ID stainless steel tube was measured when air-water bubble trains were present. The observed wall temperature was used as a boundary condition for a thermal resistance problem to obtain the time-averaged heat transfer coefficient. The maximum heat transfer enhancement over fully developed Poiseuille flow occurred at a liquid slug length to diameter ratio of unity. A correlation to predict the fully developed Nusselt number at other ratios was proposed.

Mehta and Khandekar [46] utilized a similar IR technique in bubble train experiments using deionized water and air within a 5 mm x 5 mm square minichannel. The heat transfer coefficient along the channel length was calculated using the experimentally measured channel wall temperature contours. An enhancement in heat transfer coefficient of 1.2 to 2 times over thermally developing single-phase flow was observed depending on the axial location.

1.4 OBJECTIVES

The objective of this work was to identify the contributions of various heat transfer mechanisms acting on a heated tube in the presence of a single elongated bubble at a variety of gravitational accelerations. Additionally, observations of the bubble shape and dynamics were made to allow for predictions of the flow field, which complemented the heat transfer measurements. The collected data can be utilized to guide mechanistic modeling of slug flow heat transfer and to provide validation for their results. Successful models may be used as design tools for future earth- and space-based two-phase heat exchanger systems, thereby satisfying NASA's goal of this research.

CHAPTER 2: EXPERIMENT DESCRIPTION

To characterize the heat transfer and dynamics of rising Taylor bubbles, a flow boiling experiment was conducted in which measurements of the local wall heat transfer and film thickness along with high speed images were obtained as single bubbles of varying length rose in a vertical column containing upward flowing liquid. The study of single bubbles was chosen in lieu of bubble trains so flow conditions upstream and downstream of the bubbles could be measured, reducing the complexity in approximating the flow patterns and understanding the heat transfer profile around each bubble.

A flow boiling test rig developed in the Phase Change Heat Transfer Lab was utilized for this study. The rig, which was designed for parabolic flight testing, includes the flow loop and various electronics required for testing. Figure 2.1 shows the rig in flight configuration with a secondary containment chamber surrounding the flow loop to avoid potential fluid leakage into the aircraft cabin. Three computers and four monitors were used to control the flow loop and acquire infrared, high-speed visual, and film thickness data. Several layers of safety features (overheat protection, circuit protection, strength requirements) were included per NASA specifications. The flow loop and infrared camera technique are described in the following sections.

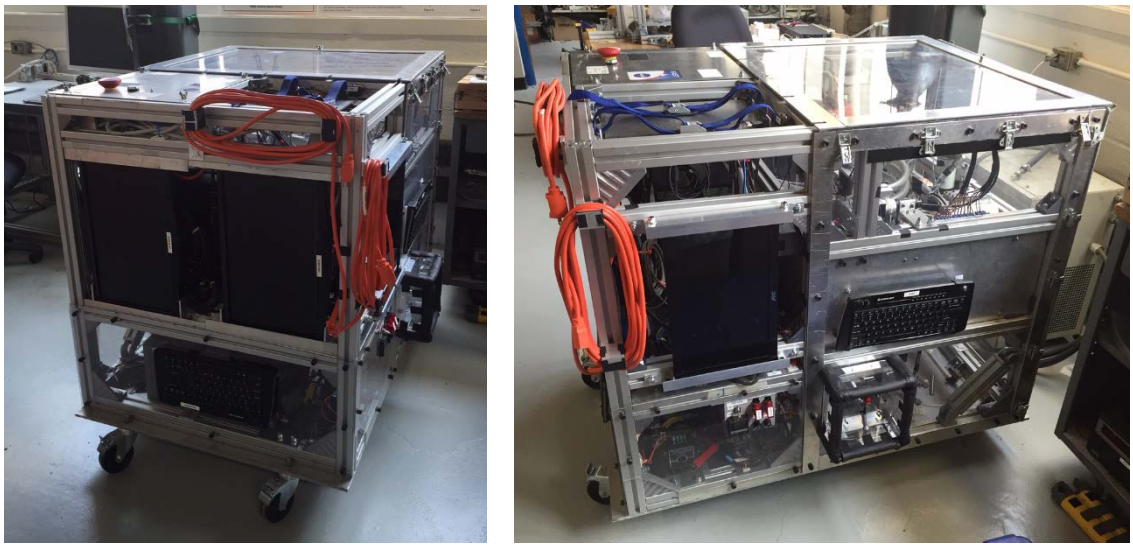

Figure 2.1: Experimental rig in parabolic flight configuration.

2.1 FLOW LOOP

A schematic of the experiment flow loop is shown in Figure 2.2. The working fluid was 3M Novec HFE 7100 ($C_4F_9OCH_3$), a non-toxic, dielectric fluid with a normal boiling temperature of 60°C. Properties at saturation conditions for 1 bar of pressure are summarized in Table 2.1.

Table 2.1: Summary of HFE 7100 properties at saturations conditions for 1 bar.

Property	**Saturation Value**
T_{sat} [ºC]	60
ρ_l [kg/m^3]	1372
h_{lv} [MJ/kg]	112.1
μ_l [cP]	0.375
σ_l [N/m]	0.128

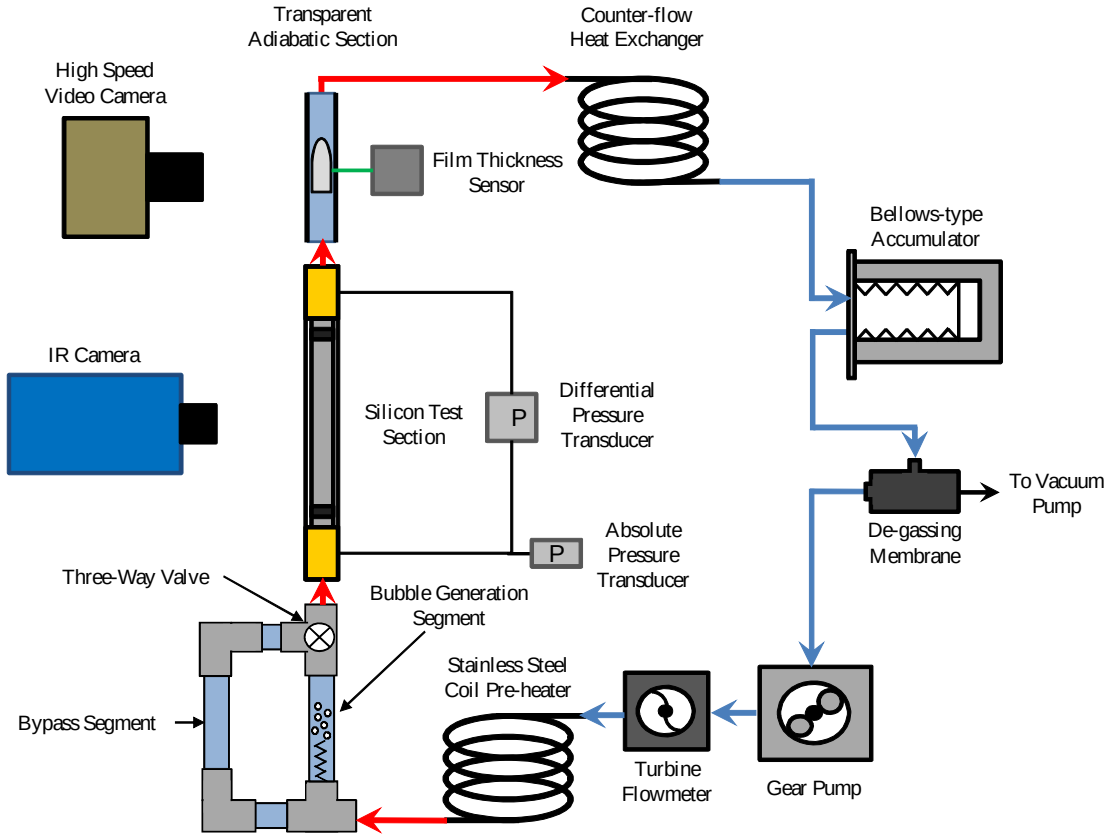

Figure 2.2: Schematic of rig flow loop.

HFE 7100 was pumped in a subcooled liquid state using a gear pump (Micropump L21755) as the flow rate was measured by a turbine flowmeter (Omega FLR1009). The liquid was heated to near saturation at the test section inlet using a stainless steel preheater powered by a modified 1000W computer power unit (Silverstone SST-ST1000-P) and controlled using pulse width modulation via a LabVIEW^{TM} interface.

The fluid then entered a section of the flow loop designed to create and release single Taylor bubbles. This section consisted of a bubble generation segment and a bypass segment connected at the downstream end by a three-way make-before-break valve as shown in Figure 2.3. To generate a bubble, the valve was set to divert the liquid flow

through the bypass segment, while a wire heater evaporated liquid in the bubble generation segment. The bubble volume was varied by adjusting the power to the wire and the heating time. Once the desired bubble volume was generated, it was released by rotating the valve such that liquid was redirected through the bubble generation segment, pushing the bubble into the test section.

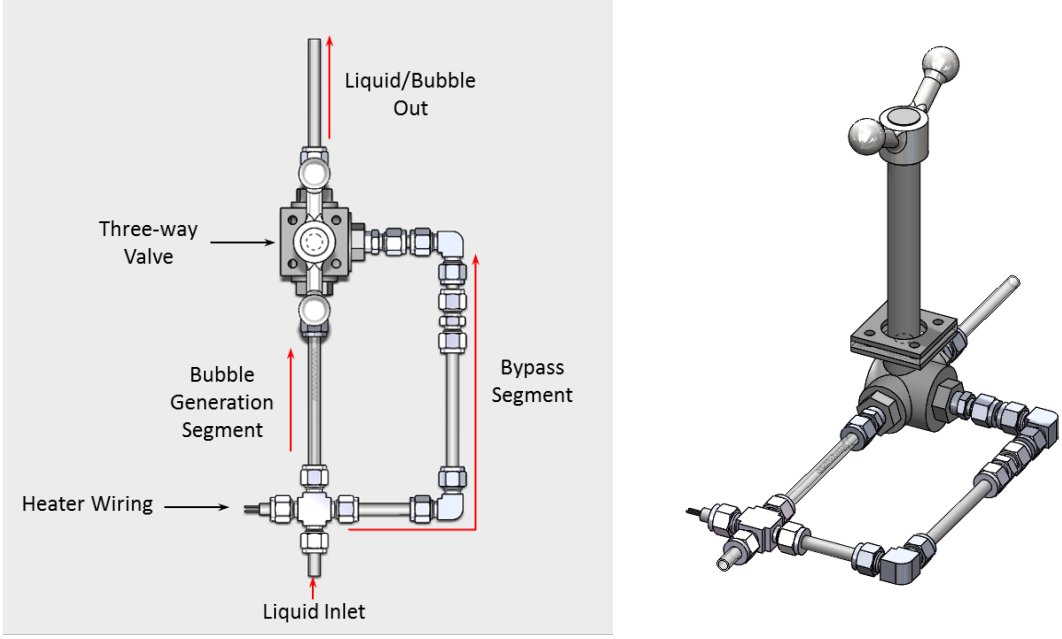

Figure 2.3: Schematic of bubble generation section: flow pattern (left); isometric view with valve handle extension (right).

The bubble rose vertically into a 6 mm ID silicon test section (see Figure 2.4) positioned 200 mm downstream of the three-way valve where heat transfer measurements and infrared flow visualization were made. Pressure taps were located at the inlet and outlet of silicon tube so differential and absolute pressures could be measured. The absolute pressure transducer (Omega PX209-030A5V) was used to determine the saturation temperature of the fluid entering the test section. Immediately after leaving the heated silicon tube, the

rising bubble passed through a glass adiabatic section (380 mm downstream of the three-way valve) where high speed video was obtained using CMOS video cameras (Phantom Miro eX4 and Sentech STC-MBCM200U3V) at frame rates between 500 and 1200 frames per second. The high-speed visualization was used to determine the bubble length, study the dynamics of the tail, and analyze the bubble shape. The liquid film thickness was measured using two techniques: a laser displacement sensor (Keyence LK-G5000) and high-speed image analysis. The Keyence sensor was calibrated by measuring a known thicknesses of HFE 7100 within a maximum uncertainty of 17 μm. Due to movement of the sensor relative to the tube when the test apparatus was flown on the aircraft, data from the Keyence sensor could not be obtained. The film thickness under these conditions were therefore calculated from analysis of the high-speed video captured in the adiabatic section. Error in the measurement created by optical distortion was removed by a calibration procedure similar to Liu et al. [27] in which a grid of known spacing was placed in the test section tube. The apparent spacing was compared to the known spacing to create a calibration curve. The uncertainty associated with this technique was estimated to be 25 μm. Further information on the calibration and uncertainty analysis of the film thickness measurement is provided in Appendix A.

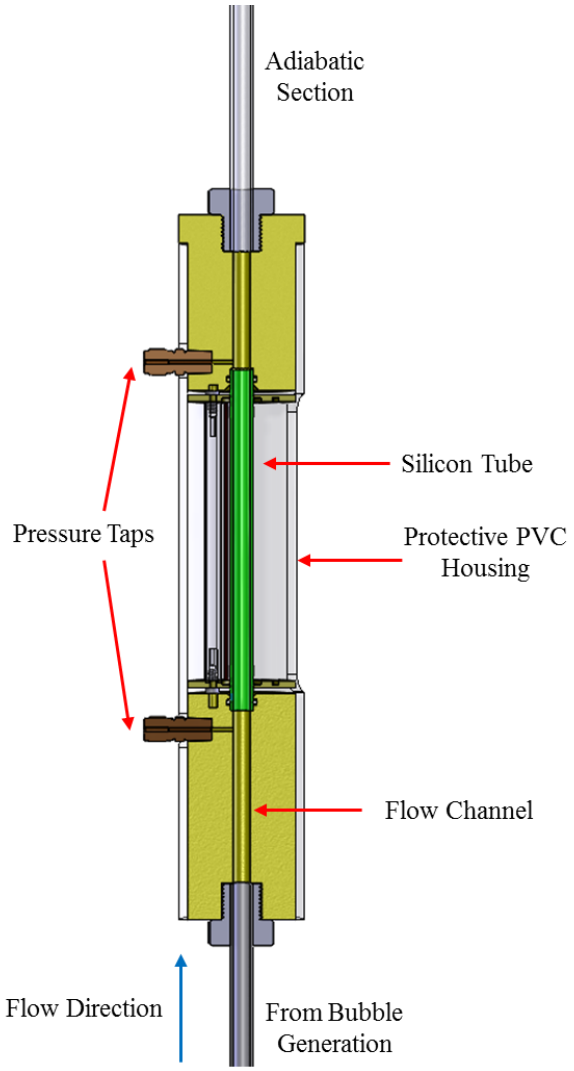

Figure 2.4: Schematic of heat transfer test section.

Bubbles were condensed and the liquid subcooled in a counterflow heat exchanger where the secondary fluid was cold water. A bellows-type accumulator was included after the condenser with the dry side open to the ambient to maintain the system pressure at nominally 1 bar in the lab, or the aircraft cabin pressure (typically 0.76-0.83 bar) during parabolic flights. Before re-entering the gear pump, the fluid was sent through a de-gassing

membrane (Liqui-Cel SuperPhobic). A vacuum pump connected to the membrane for several hours prior to data being collected was used to degas the liquid.

Transducer data was collected using a 24-channel data acquisition system (Omega OMB-DAQ-3000) and recorded at a rate of 100 Hz through a LabVIEW^{TM} interface. T-type thermocouples were installed at various locations in the flow loop for data analysis, calibration, and safety purposes. Uncertainty for the thermocouples was calculated to be ± 0.12°C. Heat transfer measurements and flow visualization were made using an IR camera (Electrophysics Silver 660M) at a frame rate of 246 Hz. Typical uncertainties for the major instrumentation and some of the reduced parameters are summarized in Table 2.2.

Table 2.2: Typical uncertainties for important system parameters and measurements.

Parameter	**Uncertainty**
G [kg/m^{2}s]	5.2
P_{abs} [millibar]	1.3
δ [μm]	17 or 25
T_{cam} [°C]	0.14
k_p [W/m-K]	0.01
α_{Si} [1/m]	6.5
α_p [1/m]	192
T_{sat} [°C]	0.14

2.2 IR TECHNIQUE

Heat transfer measurements and flow visualization were obtained using an IR thermometry technique developed by Kim et al. [47] that takes advantage of the transparency of silicon in the mid-IR range (3-5 μm). HFE 7100 passed through the 6 mm ID (8 mm OD) single crystal silicon tube which was doped to allow for resistive heating. The input power to the

tube was varied by adjusting the voltage of a high-voltage power supply. The inner wall was of the tube was coated with a 57 μm layer of polyimide tape ($k_p = 0.12$ W/m-K) as shown in Figure 2.5 One half of the inner circumference was then covered with an IR opaque paint containing carbon black (Nazdar GV111), which allowed an effective inner wall temperature to be measured through the silicon and polyimide layer. Two strips of the painted polyimide tape were also attached to the outer wall of the tube so the outer wall temperature could be measured. To complement the heat transfer measurements, the flow was visualized using a set of six gold-plated mirrors (Figure 2.5, left image) arranged such that flow visualization and heat transfer measurements could be captured using a single camera. A representative IR image illustrating the two "halves" of the tube is shown in Figure 2.6. The top half was used to visualize the flow within the channel, while the bottom half was used for temperature measurements. Note the two white (warmer) strips on the bottom half which are the two black tape strips on the outside of the tube.

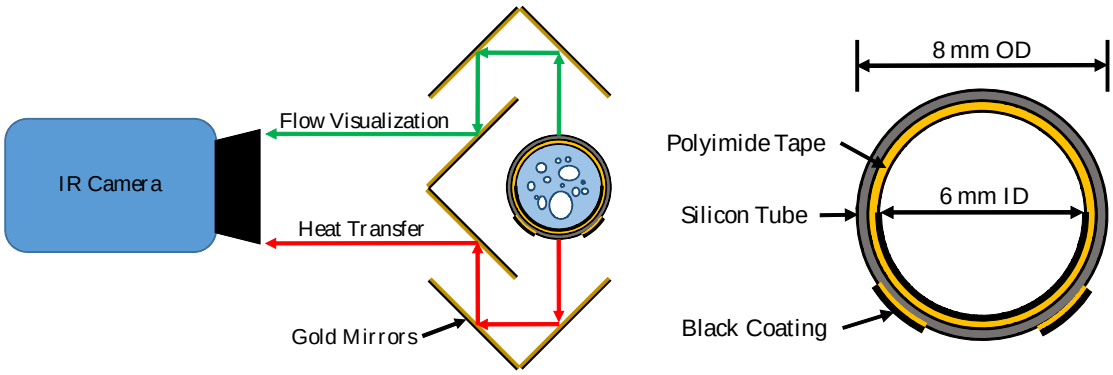

Figure 2.5: Mirrors to provide simultaneous heat transfer measurements and flow visualization (left image), and cross-sectional view of silicon tube with coated polyimide tape (right image).

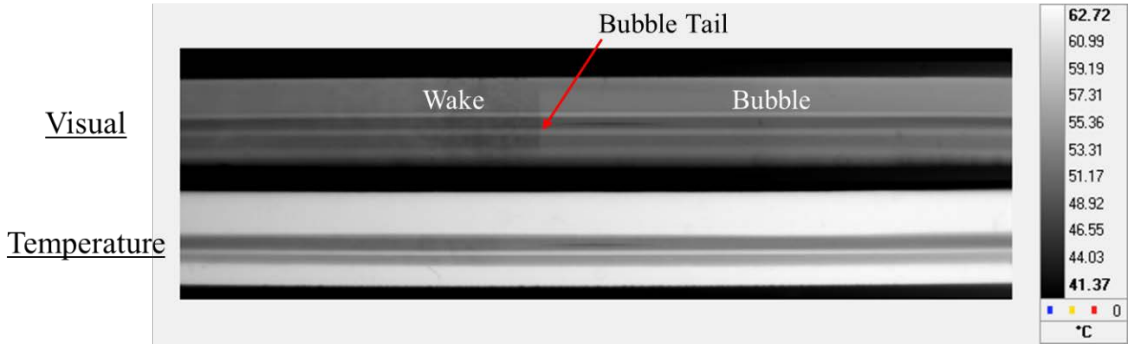

Figure 2.6: Representative IR image showing tube "halves" observed using mirror arrangement. The top half was used for visual observation of the internal flow, while the bottom half allowed for temperature measurements to be made.

The temperature profiles within the multilayer were calculated using a 1-D heat conduction equation where the governing equations for the silicon (eqn. (6)), adhesive (eqn. (7)), and polyimide layers (eqn. (8)) are given by

$$\rho_{Si} c_{p,Si} \frac{\partial T}{\partial t} = k_{Si} \nabla^2 T + \dot{q}_{Si} \tag{6}$$

$$\rho_{ad} c_{p,ad} \frac{\partial T}{\partial t} = k_{ad} \nabla^2 T \tag{7}$$

$$\rho_{p} c_{p,p} \frac{\partial T}{\partial t} = k_{p} \nabla^2 T \tag{8}$$

with boundary conditions $T=T_{s,o}(z,t)$ at the outer silicon tube wall and $T=T_{s,i}(z,t)$ at the liquid/polyimide interface. A schematic of the multilayer is shown in Figure 2.7 with the two boundary conditions labeled along with representations of the thermal gradients present within the layers.

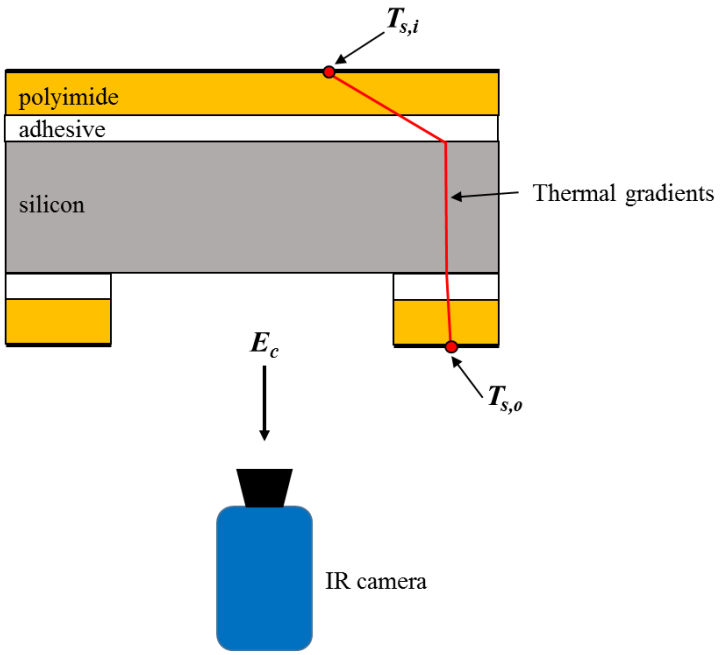

Figure 2.7: Schematic of silicon tube and tape multilayer showing the thermal gradients present due to heating of the tube and cooling from forced convection and boiling.

Due to absorption, reflection, and emission of energy by the various layers, the observed temperature of the inner and outer black surfaces were not indicative of the actual temperatures. Instead, a set of optical calculations was coupled with the conduction equations to determine the correct boundary conditions. The temperature of the tube outer surface was obtained by an iterative process involving two unknowns. The theoretical energy collected by the camera while observing the outer tube surface could be calculated by summing the energy from each of the sources,

$$E_{c,o} = (1 - \varepsilon_s)E_\infty + \varepsilon_s E_{s,o} \tag{9}$$

where ε_s is the emissivity of the black paint, $E_\infty = F_{\lambda_1-\lambda_2}\sigma T_\infty^4$ is the energy contributed by the surroundings, and $E_{s,o} = F_{\lambda_1-\lambda_2}\sigma T_{s,o}^4$ is the blackbody radiation emitted by the outer black surface. $F_{\lambda_1-\lambda_2}$ is the fraction of total blackbody energy collected by the camera over

its bandwidth ($\lambda_1 - \lambda_2 = 3 - 5$ μm) at a particular temperature. As a result, $F_{\lambda_1-\lambda_2}$ varied for each source term in eqn. (9) and was determined by integration of Planck's function over the wavelengths and temperature of interest. T_∞ was determined experimentally by an in-situ calibration in which liquid HFE 7100 at a known temperature flowed through the tube at a high mass flow rate. Due to the high thermal conductivity of silicon, an effective T_∞ was calculated such that $T_{s,o}$ was equal to the fluid temperature. This procedure was repeated for several fluid temperatures to ensure an accurate calibration.

With the surroundings source term defined, the remaining unknowns were $T_{s,o}$ and $F_{\lambda_1-\lambda_2}$, which is a function of $T_{s,o}$. A temperature for the tube outer surface was assumed and the theoretical energy collected by the camera calculated. After comparing to the actual collected energy, $T_{s,o}$ was updated and the process repeated until the change in temperature was acceptable ($\Delta T_{s,o} \leq 10^{-6}$ °C).

Determination of the polyimide/liquid interface temperature was more complex as the absorption, emission, and reflection of the multilayer components were accounted for. The theoretical energy collected by the camera while observing the inner black surface was calculated using the equation,

$$E_{c,i} = \rho_{\infty-c} E_\infty + \varepsilon_{Si-c} E_{Si} + \varepsilon_{T-c} E_T + \tau_{s-c} E_{s,i} \tag{10}$$

where $E_{Si} = \int_0^{L_{Si}} \alpha_{Si} F_{\lambda_1-\lambda_2} \sigma [T_{Si}(x)]^4 \exp(-\alpha_{Si} x) dx$ is the energy emitted by the silicon that reaches the air/silicon interface, $E_T = \int_0^{L_T} \alpha_T F_{\lambda_1-\lambda_2} \sigma [T_T(x)]^4 \exp(-\alpha_T x) dx$ is the energy emitted by the combined adhesive and polyimide layer that reaches the adhesive/silicon interface, and $E_{s,i} = F_{\lambda_1-\lambda_2} \sigma T_{s,i}^4$ is the blackbody radiation emitted by the inner black surface. The properties $\rho_{\infty-c}$, ε_{Si-c}, ε_{T-c}, and τ_{s-c} are the effective reflectivity of the multilayer, effective emissivity of the silicon, effective emissivity of the combined

adhesive/polyimide layer, and effective transmissivity of the multilayer, respectively. Their derivations can be found in Kim et al. [47]. A separate value of T_∞ was determined for the inner wall calculations by a calibration technique in which the inner and outer wall temperatures were measured while single-phase liquid was passed through the silicon tube with constant power applied to the tube. Heat losses from the tube to the surroundings and test section housing were approximated using the tube outer wall profile. Further information on the loss calculations are provided in the appendix (section A.2.7). The heat losses were subtracted from the input power (measured using the four-wire method) to determine the net heat absorbed by the fluid. An energy balance using thermocouple measurements upstream and downstream of the test section were in agreement with these calculations. An effective T_∞ was then calculated such that the average heat flux along the tube length, determined from the measured wall temperatures and MATLAB analysis, agreed with the net heat flux value. This procedure calibrated out variations in optical properties with temperature, reflections from within the tube, and thermal contributions from the surroundings.

With E_∞ defined, the theoretical energy calculated by eqn. (10) was compared to the actual energy collected by the camera. If a difference was observed, an updated $T_{s,i}$ was determined. The inner and outer tube temperatures were used as a boundary condition for the conduction equations to determine a new temperature profile. This procedure was repeated at each time step until $T_{s,i}$ no longer changed by a significant value ($\Delta T_{s,o} \leq 10^{-6}$ ℃). The final calculated temperature profile at each t was used as the initial assumption for the following time step.

The instantaneous heat flux at each pixel was determined by calculating the temperature gradient at the polyimide/liquid interface, or $q" = -k_p \frac{\partial T}{\partial x}\Big|_{x=x_{s,i}}$. For general two-phase heat transfer measurements, the heat transfer coefficient was defined as $h = \frac{q"}{(T_{s,i} - T_{sat})}$, where $q"$ and $T_{s,i}$ are defined at each axial pixel location by the calculations above. The saturation temperature (T_{sat}) was found using the test section absolute pressure, according to saturation data provided by 3M (manufacturer of HFE 7100). The heat transfer coefficient for Taylor bubble experiments was defined as $h = \frac{q"}{(T_{s,i} - T_m)}$, where T_m is the mean fluid temperature at each axial location calculated by an energy balance on the fluid using the measured heat flux. This definition was chosen because slightly subcooled conditions ($1-3°C$) were required to prevent undesired nucleation in the pre-heater.

2.2.1 Validation

The IR thermography technique was validated through single-phase and two-phase testing in a vertical upward flow configuration. For turbulent single-phase flow, liquid passed through the heated silicon tube and the heat transfer coefficient along its length was measured. The experimentally measured heat transfer coefficient was compared to the Dittus-Boelter equation corrected for the thermally developing flow at the beginning of the heated silicon tube using the factor proposed by Al-Arabi [48]. The experimental data shown in Figure 2.8 is in good agreement with the correlation. Additional validation of the technique for the case of laminar single-phase flow was completed by measuring the temperature of the tube inner wall at two heat fluxes. Heat losses attributed to natural convection on the tube outer wall and axial conduction along the tube into the test section end caps were calculated to be 32±4% at these conditions (23±3% to axial conduction,

9±1% to natural convection). Losses due to axial conduction were approximated using the temperature gradient at the downstream end of the tube, measured using the infrared technique. Natural convection losses were estimated using a correlation by Churchill and Chu [49] for free convection from a vertical wall, where the surface temperature was taken as the average outer wall temperature of the tube. An energy balance on the test section conducted by measuring the inlet and outlet liquid temperatures during heating confirmed the calculations.

The ratio of Grashof number $\left(Gr = \frac{g\beta(T_w - T_m)D^3}{v^2}\right)$ to the square of the liquid Reynolds number was of the range $0.68 \leq \frac{Gr}{Re_l^2} \leq 1.17$, indicating that natural convection and forced convection likely contribute to heat transfer from the inner tube wall, according to Incropera et al. [50]. In the absence of available correlations from the literature, Incropera et al. suggest that the mixed convection Nusselt number (Nu_M) be computed using the form $Nu_M^n = Nu_F^n + Nu_N^n$, where Nu_F is the forced convection Nusselt number and Nu_N is the natural convection Nusselt number, both computed using existing correlations for the specific geometry. In this case, Nu_F was approximated from Shah and London [51] and Nu_N from Davis and Perona [52]. It was noted that the best correlation of data is often obtained for $n = 3$, which was chosen for this case. Accounting for heat losses, the predicted and measured inner wall temperature (T_w) offset by the tube inlet temperature (T_{in}) is plotted as a function of axial position in Figure 2.9 showing relatively good agreement within the uncertainty of the measurements and predictions. The decline in wall temperature at the tube exit is dominated by wall axial conduction losses.

Due to limitations in microgravity and hypergravity duration, extensive validation of the experiment was not able to be conducted under those conditions. However, energy

balance tests, as described above, were repeated in the laboratory based on the conditions experienced on the aircraft. Notably, the effect of natural convection variation on the outer tube wall could not be studied, but two comments in this regard may be made. First, according to the correlation of Churchill and Chu [49], the average heat transfer coefficient for free convection over a vertical plate is related to gravity by the $1/4^{th}$ power. As a result, an increase in gravity level by a factor of 1.8 (hypergravity) yields an increase in the heat transfer coefficient by 16%, yet only an overall increase in power lost by 1.4% ($9\% \times 1.16 = 10.4\%$). Second, natural convection loss for $a/g = 0.01$ was assumed to be similar to $a/g = 1$, given that the data collected under microgravity was taken 2-3 seconds after the transition from $a/g = 1.8$ to $a/g = 0.01$ and currents associated with free convection may have still existed. All data was processed using the corresponding heat loss calculations for that gravity level.

Two-phase validations were conducted by comparing data obtained in the churn and annular flow regime to data collected by a group at IMFT in Toulouse, France using a test apparatus of different design but operated under similar conditions [53]. Figure 2.10 shows that data collected from both experiments are in agreement with each other as well as the correlations by Chen [54] and Cioncolini and Thome [55] at low vapor qualities.

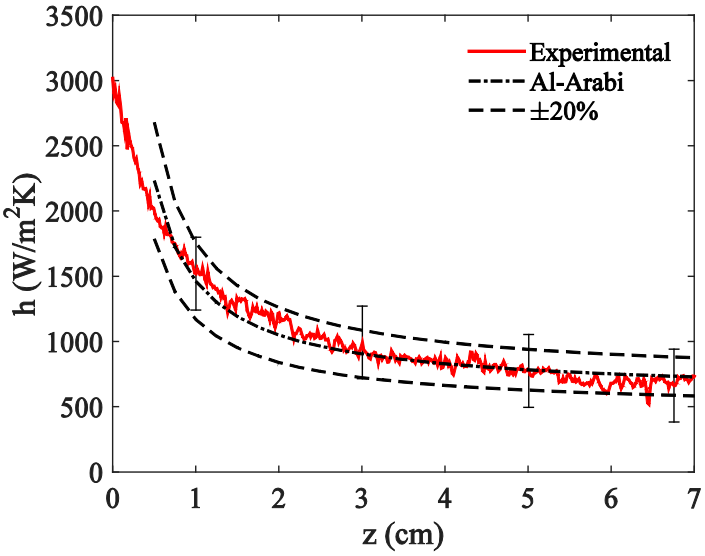

Figure 2.8: Experimental heat transfer coefficient compared to the Dittus-Boelter correlation with the Al-Arabi correction for the parameters: HFE 7100, Re=5545, T_{sub}=20°C, q"=20 kW/m^2.

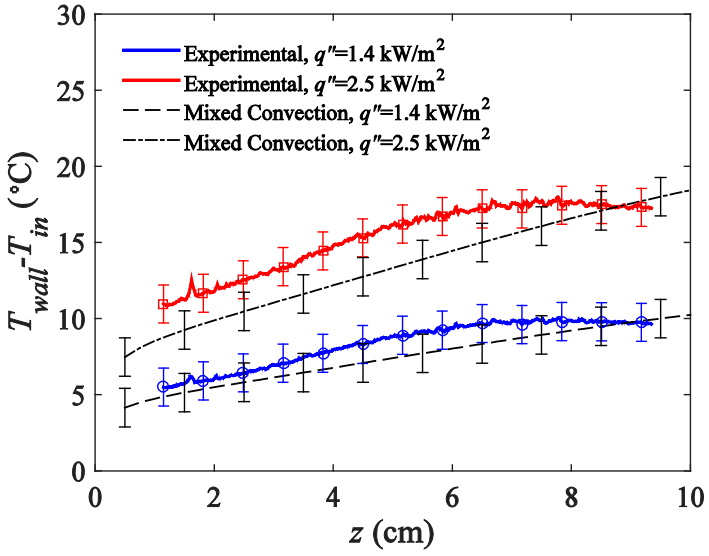

Figure 2.9: Experimental heated wall temperature offset by the liquid inlet temperature as a function of axial length along the tube compared to correlations for mixed convection. The conditions were: G=50 kg/m^{2}s, Re=790, T_{in}=45°C, and q''= of 1.4 kW/m^2 and 2.5 kW/m^2.

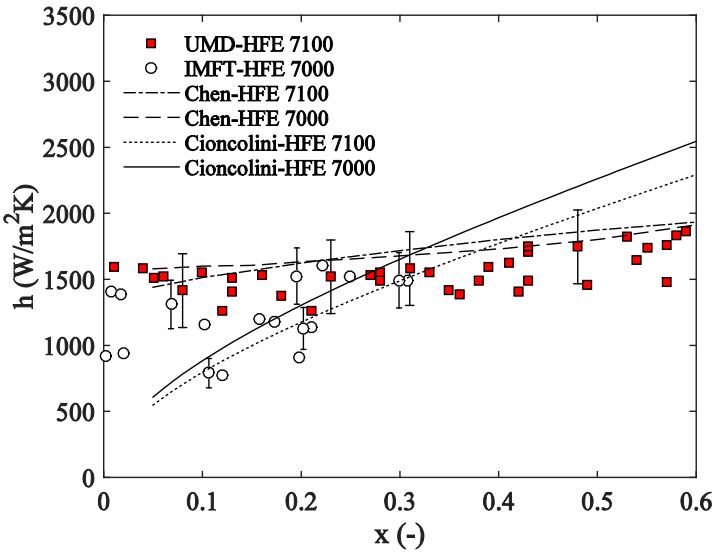

Figure 2.10: Comparison of two-phase data collected by UMD and IMFT with similar experiments at conditions – UMD: G=100 kg/m^{2}s, q''=10 kW/m^2; IMFT: G=100 kg/m^{2}s, q''=9.8-36 kW/m^2 (figure adapted from Narcy et al. [53]).

2.2.2 Uncertainty analysis

The uncertainty associated with heat transfer measurements can be divided into two parts: bias error and random error. Bias uncertainty is attributed to possible error associated with the determination of material optical properties, thicknesses, thermocouple readings, and camera temperature readings. An additional uncertainty relating to the approximation of heat losses was also present, but considered as a separate source of bias error. Major sources of bias uncertainty and their values are summarized in Table 2.2, including the absorptivity of the silicon tube and polyimide tape, thermal conductivity of the polyimide tape, and IR camera temperature measurement. The bias uncertainty in measured heat flux was calculated to be $\delta q''$=2.3 kW/m^2 over the range of applied tube heat fluxes in this work. Bias uncertainty in the heat transfer coefficient varied linearly with applied heat flux, ranging from δh=0.30 kW/m^{2}K at q''=2.0 kW/m^2 to δh=0.73 kW/m^{2}K at q''=11.7 kW/m^2.

The values of the bias uncertainty were the same order of magnitude of the measurements themselves in most cases, but their effect can be partially negated by an offsetting procedure due to the fact that the error sources are fixed values or measurements from set calibration curves (with the exception of heat loss calculations). Therefore, if the measured heat flux for single-phase flow observed just ahead of the bubble is subtracted from the heat flux measured when the bubble is present, then the heat flux enhancement due to the presence of the bubble can be defined as $q"_{enh} = (q" + (\delta q")_{bias}) - (q"_{SP} + (\delta q"_{SP})_{bias}) \pm (\delta q")_{heat\ loss} = q" - q"_{SP} + (\delta q" - \delta q"_{SP})_{bias} \pm (\delta q")_{heat\ loss}$. If the bias uncertainty is same for both measurements, the heat flux enhancement reduces to $q"_{enh} = q" - q"_{SP} \pm (\delta q")_{heat\ loss}$. If the bias uncertainties are unequal, the difference must be incorporated into the overall uncertainty by propagating the errors.

The random uncertainty was calculated by means of propagation of error for averaged measurements proposed by Taylor [56] in which the averaged uncertainty decreases with respect to the individual measurement uncertainty by a factor of $1/\sqrt{N}$, where *N* is the number of averaged measurements. Each temporally averaged bubble heat transfer profile, a discussion of which will follow later, is considered an individual measurement whose random uncertainty is characterized by $\delta_r = \frac{\sigma_r t}{\sqrt{N}}$, where σ_r is the standard deviation of the heat flux or heat transfer coefficient about the mean value at each location along the bubble and *t* is the parameter associated with measurements which are assumed to follow the Student's *t* distribution. Hereafter, error bars presented in heat transfer figures denote the random uncertainty associated with the particular measurement as well as the uncertainty remaining from bias offsetting of measurements.

2.3 DATA COLLECTION

The procedure for normal gravity data collection began with the initialization of the experimental rig and components therein. Once circulation was established within the flow loop, heating of the liquid to near saturation was begun and the system was allowed to come to equilibrium over a period of roughly 30 minutes. Just prior to testing, a "constant temperature" data point was taken in which liquid of known input temperature was passed through the test sections at a high flow rate as a means of calibration for the infrared video and thermocouples. The silicon test section was then set to the desired applied wall heat flux and several bubbles were generated to ensure proper operation of the system. The procedure for each data point was as follows: 1) a bubble of desired volume was created in the generation section; 2) recording of the test conditions was started via LabVIEW^{TM}; 3) infrared and film thickness data collections were begun; 4) the bubble was released and tracked through the various sections to ensure no secondary bubbles were present; 5) recording of test conditions, infrared, and film thickness data was stopped. This process was completed for 10-15 bubbles during each collection session. Data was analyzed using a series of MATLAB [57] scripts yielding calibrated test conditions, heat transfer measurements, and bubble film profiles.

The experiments completed under a normal gravity environment provide insightful information into the heat transfer and flow characteristics of Taylor bubbles rising under the conditions available in the laboratory. The bubble drift velocity, U_d, however, is a parameter that will be shown to play a role in determining the bubble shape and the heat transfer in the following sections, but is not easily varied. A slight manipulation of eqn. (2) yields a relation for U_d, which is seen to be dependent on the parameters C, U_l, and $U_{b,0}$,

$$U_d = U_b - U_l = (C-1)U_l + U_{b,0} \tag{11}$$

where $U_{b,0}$ has been found to be function of the difference in the liquid and vapor densities, gravity level, liquid viscosity, liquid surface tension, and tube diameter. The range of bubble drift velocities available for the laboratory experiments was limited as the dominant term in eqn. (11) is $U_{b,0.}$ Modification of the test section tube diameter or exchanging the test fluid would provide an expansion of the drift velocity range, but would prevent direct comparison of old and new data sets. Varying the gravitational acceleration experienced by the bubble delivers a less obvious, yet more straightforward solution.

Several means exist to increase or decrease the gravity level in the experimental environment. Drop tower tests are relatively inexpensive and can be repeated several times per day, but the microgravity duration is too short (2-3 seconds) to allow for a bubble to be released and tracked through the test sections. Conducting experiments on a sounding rocket or the International Space Station, while providing longer microgravity periods (minutes to months), are cost and size prohibitive. A median solution is a parabolic flight campaign in which researchers are provided 20-30 seconds of microgravity and hypergravity, while being able to work directly with their test rig. Experiments were, therefore, conducted aboard NASA's C-9 aircraft (shown in Figure 2.11a) which was based at Johnson Space Center in Houston, TX. The campaign consisted of four flights with each consisting of forty parabolic trajectories similar to the one shown in Figure 2.11b. Each parabola provided up to 22 seconds of microgravity (0.02±0.01g) and up to 30 seconds of hypergravity (1.8±0.01g) during which data could be collected.

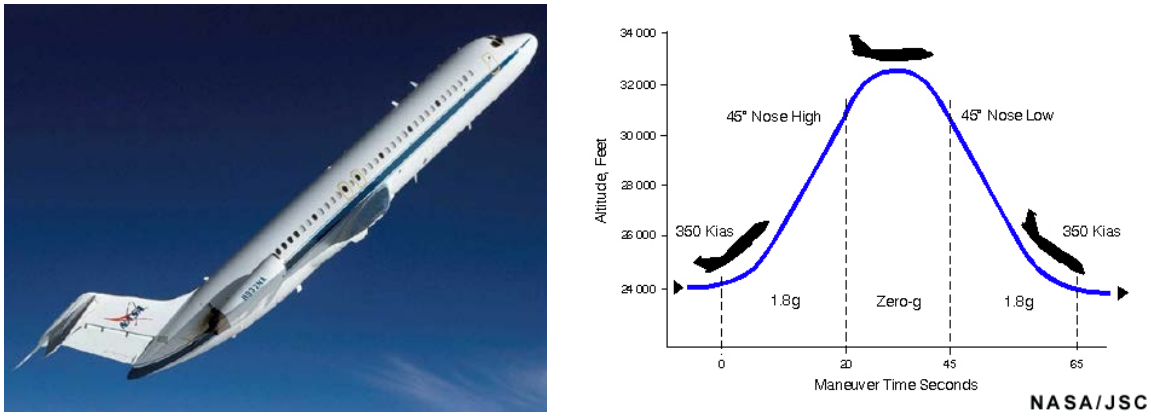

a) b)

Figure 2.11: Description of parabolic flight campaign: a) NASA C9 aircraft; b) parabolic flight profile (photo and graph courtesy of NASA).

The data collection procedure during parabolic flights was slightly abbreviated compared to experiments conducted in the laboratory. Due to aircraft fuel and flight plan restrictions, the available time to initialize the test rig and preheat the flow loop was reduced to 10-12 minutes. The reduced pressure within the cabin, however, provided a lower required heating temperature as the saturation temperature of the fluid was decreased. As a result, the restricted warming time was still sufficient to allow the system to reach an equilibrium temperature. Individual data points were collected using the same series of steps described for normal gravity testing for a total of approximately 40 bubbles during each flight. The extended duration of testing required “constant temperature” data to be collected periodically to account for heating of the infrared camera housing and the rig containment volume. Data was later analyzed as described previously.

Normal gravity and variable gravity results were combined into a complete data set which spans a wide parametric space and provides novel insight into heat transfer

mechanisms of rising elongated bubbles. These results are presented and discussed in the following chapter.

CHAPTER 3: RESULTS AND DISCUSSION

Data was collected in the laboratory and during a parabolic flight campaign which consisted of 164 parabolic maneuvers. Each parabola provided approximately 20 seconds of microgravity ($\pm 0.01g$) and 30 seconds of hypergravity ($1.8g \pm 0.1g$) where g is gravitational acceleration. Background liquid velocities within the test section were of the range 35 mm/s $\leq U_l \leq$ 140 mm/s (50 kg/m^{2}s $\leq G \leq$ 200 kg/m^{2}s), which correspond to liquid Reynolds numbers $\left(Re_l = \frac{GD}{\mu_l}\right)$ between 790 and 3090. The variation of these parameters allowed for heat transfer measurements and flow visualization to be obtained at 0.49 < *Bo* < 87, thereby spanning both capillary and Taylor bubble regimes. A summary of the test conditions is given in Table 3.1.

Table 3.1: Summary of data parameters.

U_d (mm/s)	G (kg/m^{2}s)	Re_l	a/g	Bo	U_f (mm/s)	U_b (mm/s)
20	100	1580	0.01	0.48	–	90
41	200	3090	0.01	0.48	–	180
94	200	3090	0.34	16.5	–	235
105	50	790	1	48.4	851	142
124	100	1580	1	48.4	1030	196
144	50	790	1.8	87.2	1151	180
163	200	3090	1	48.4	1402	305
173	100	1580	1.8	87.2	1389	241
208	200	3090	1.8	87.2	1754	349

3.1 BUBBLE DYNAMICS

Elongated bubbles released from the bubble generation section rose into the silicon test section where the heat transfer was measured. High-speed video was then obtained as the bubble passed through the adiabatic glass section. The bubble velocity was determined by tracking the bubble nose as a function of time. A series of 5–20 bubbles were analyzed and averaged to obtain the bubble velocity at each liquid velocity for four gravity levels as shown in Figure 3.1. For a given liquid velocity, the bubble velocity was found to increase with increasing gravity due to the larger buoyancy force acting on the bubble. A line was fit to the velocity measurements at three gravity levels (a/g=0.01, 1, and 1.8) to compare the data with correlations of the form proposed by Nicklin et al. [16]. Results for $U_{b,0}$ are compared to the predictions of White and Beardmore [18], Rattner and Garimella [20], Brown [19], and Viana et al. [13] in Table 3.2. Very good agreement is seen with Brown, Viana et al., and White and Beardmore for normal gravity conditions (1g), while the correlations tend to slightly under-predict $U_{b,0}$ at hypergravity. As expected, $U_{b,0}$ was very small under microgravity (±0.01g) conditions due to the small residual buoyancy force. Similar observations were made by Colin et al. [58] for Taylor flow in microgravity.

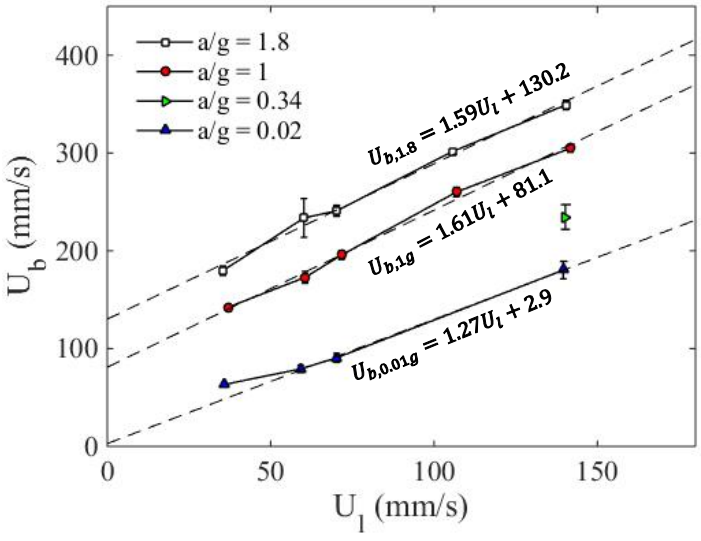

Figure 3.1: Bubble velocity as a function of liquid velocity for *a/g*=0.01, 0.34, 1, and 1.8.

Table 3.2: Comparison of measured $U_{b,0}$ to those calculated from published correlations.

a/g	**Present Study**	**White and Beardmore** [18]	**Brown** [19]	**Viana et al.** [13]	**Rattner and Garimella** [20]
0.01	2.9±5.8	0.0	—	—	0.0
1	81.1±4.1	79.6	82.0	82.4	72.4
1.8	130.2±8.8	112.3	110.4	110.6	108.8

Calculated values for *C* at 1*g* and 1.8*g* (*Bo*=49 and 87) were found to fall within the classical bounds of 2 and 1.2 for the laminar and turbulent liquid flow regimes, respectively. Under microgravity conditions (*Bo*=0.49), *C* was measured to be smaller than at normal and hypergravity. The variation is likely due to a transition from Taylor flow to capillary flow given that the bubble *Bo* in microgravity lies below the critical values suggested by previous authors [18,21,36–38]. Visual evidence of a transition is provided in Figure 3.2 where high-speed images of bubbles rising at various gravity levels and bubble drift velocities ($U_d = U_b - U_l$) are shown. Under microgravity conditions (Figure

3.2a,b), the bubbles exhibited rounded tail profiles whose radius of curvature increased with drift velocity. Stationary, small amplitude interfacial waves were observed at U_d=20 mm/s (Figure 3.2a). When the drift velocity increased to 41 mm/s (Figure 3.2b), the waves became more frequent, larger in amplitude, and oscillated in the streamwise direction. Above U_d=94 mm/s (Figure 3.2c–e), the Taylor bubbles possessed flat tails that wobbled as the bubbles rose. The magnitude of the wobble was found to increase with bubble length. Figure 3.3 illustrates the tail shape of two bubbles rising in a co-current flow at U_l=37 mm/s and a/g=1. The shorter bubble (L_b/D=2.1) experienced mild oscillations and the tail profile remained relatively perpendicular to the flow direction, while the longer bubble (L_b/D=8.8) oscillated significantly and exhibited irregular tail shapes. This trend is in agreement with Polonsky et al. [22], who showed that a small increase in oscillation frequency and large increase in amplitude accompanied bubbles with longer lengths.

A more detailed bubble profile analysis was conducted using the open source image processing program ImageJ [59]. The nose profiles of bubbles with drift velocities of U_d=20, 41, 94, 175, and 214 mm/s are compared in Figure 3.4. The bubbles exhibit narrower, more rounded nose contours with increasing U_d. The theoretical nose shape suggested by Dumitrescu [60] for a Taylor bubble rising in a stagnant column of fluid without viscosity or surface tension at normal gravity is also included. With a corresponding drift velocity of approximately 81 mm/s (the value of $U_{b,0}$ at 1g), Dumitrescu's profile is seen to fall between the experimental curves for U_d = 41 and 94 mm/s near the top of the bubble. As the liquid film develops, the prediction moves within the measured profile for U_d=94 mm/s but remains within the uncertainty of the experiment.

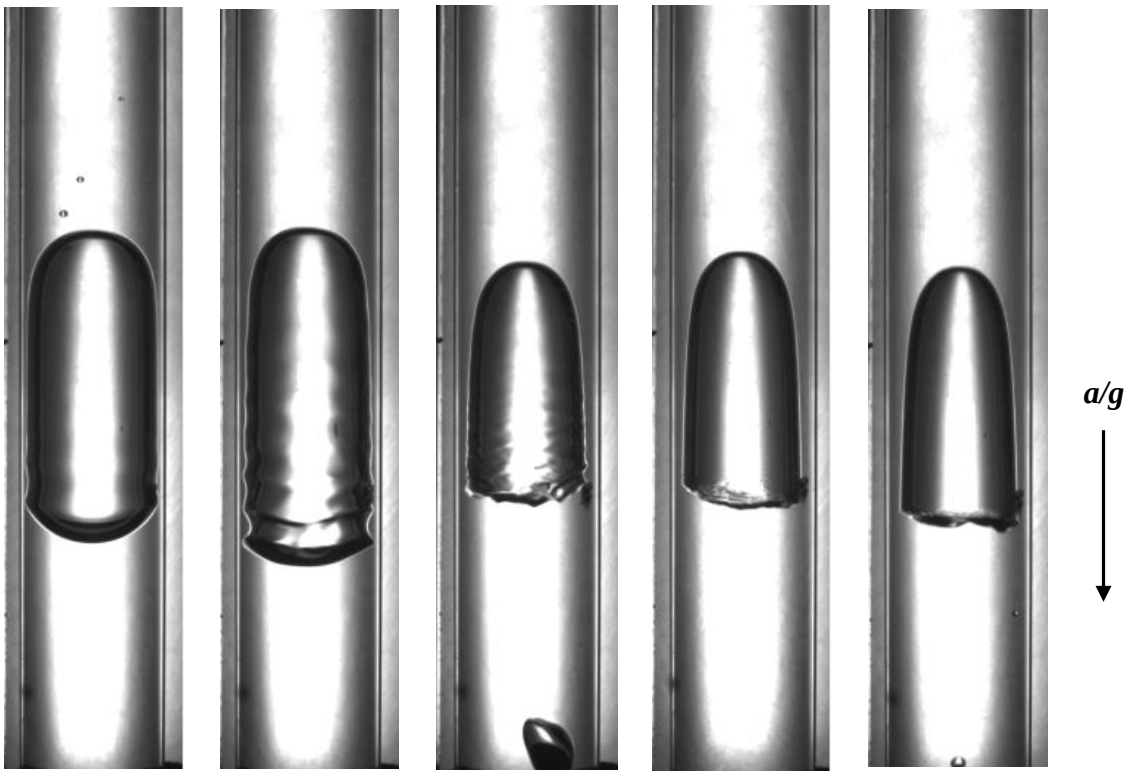

Figure 3.2: Images of representative bubbles at varying accelerations and drift velocities: a) a/g = 0.02, U_d = 20 mm/s, Bo = 0.97, L=17 mm; b) a/g = 0.02, U_d = 41 mm/s, Bo = 0.97, L=18 mm; c) a/g = 0.34, U_d = 94 mm/s, Bo = 16.6, L=13 mm; d) a/g = 1, U_d = 106 mm/s, Bo = 48.7, L=13 mm; e) a/g = 1.8, U_d = 214 mm/s, Bo = 87.7, L=13 mm.

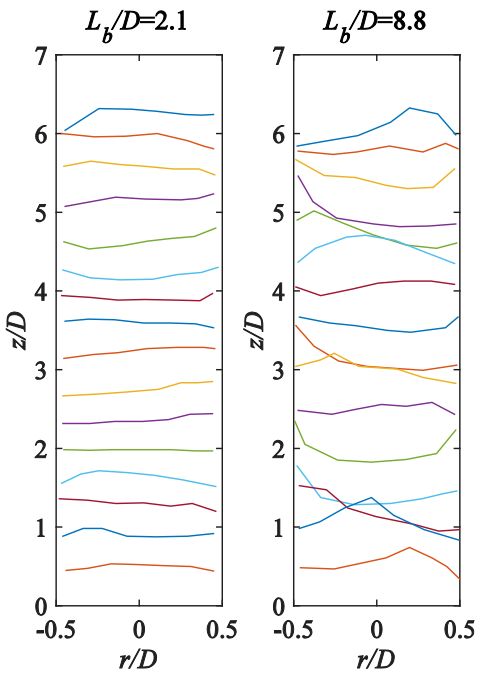

Figure 3.3: Representative tail profiles for two bubbles rising in co-current flow with U_l=37 mm/s.

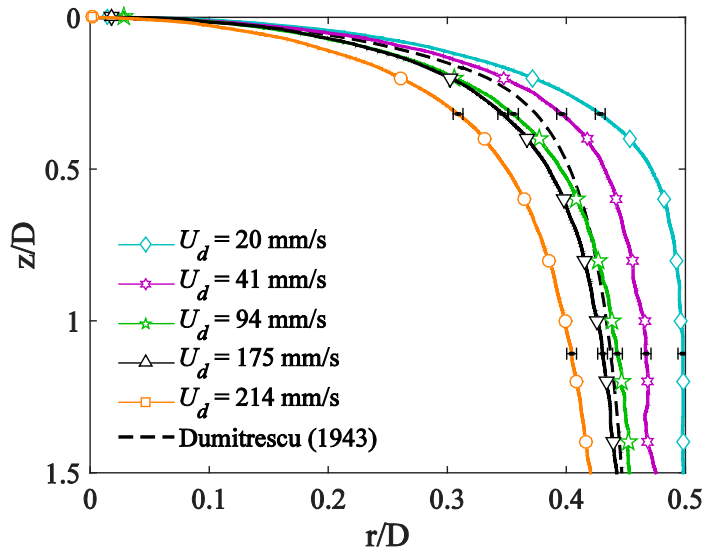

Figure 3.4: Bubble nose profiles at $\underline{U_d}$=20, 41, 94, 175, and 214 mm/s. The theoretical profile of Dumitrescu for U_d=81 mm/s is also shown.

As was mentioned, small waves were observed for capillary bubbles (U_d=20 and 41 mm/s) at the vapor/liquid interface near the bubble tail. Profiles for two representative bubbles at these drift velocities are shown in Figure 3.5. The wavelength (λ) of the waves was found to be slightly dependent upon U_d with values of 2.13 ± 0.04 mm and 1.79 ± 0.04 mm for U_d=20 and 41 mm/s, respectively. Ratulowski and Chang [61] numerically predicted the shape of elongated bubbles as a function of the Capillary number $\left(Ca = \frac{\mu U_b}{\sigma}\right)$. A series of relations were developed for the characteristic wavelength of capillary waves at the bubble interface. For Ca=0.0034 (U_d=20 mm/s) and Ca=0.0069 (U_d=41 mm/s), Ratulowski and Chang predict λ to be 2.15 mm and 2.83 mm, quite similar to the current experimental results. Edvinsson and Irandoust [62] compared their numerical results for λ to those of Ratulowski and Chang, and found that λ/D was overpredicted by the original results for Ca>0.005. Edvinsson and Irandoust's results were applied to the current study yielding a wavelength of 2.41 mm for bubbles with U_d=41 mm/s, which is somewhat closer to the current measurement of 1.79 ± 0.04 mm than predictions from Ratulowski and Chang.

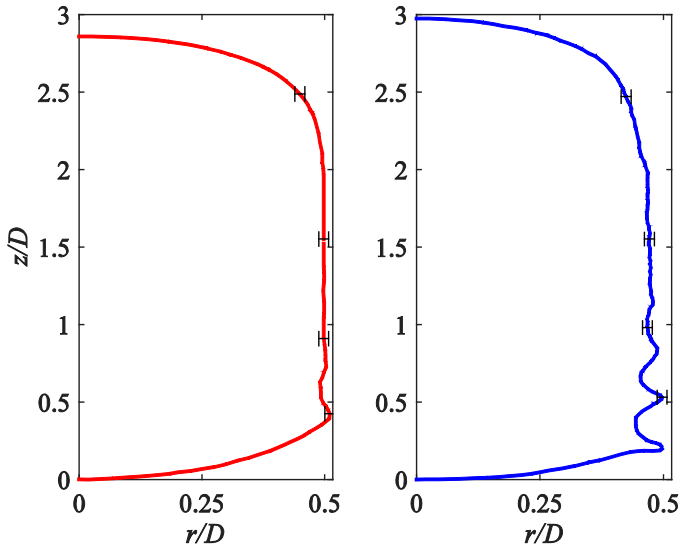

Figure 3.5: Bubble shape profiles for U_d=20 mm/s (left) and U_d=41 mm/s (right) under microgravity conditions.

The liquid film thickness for Taylor bubbles ($U_d > 94$ mm/s) was obtained using either the Keyence sensor or high-speed image analysis as described previously. Figure 3.6 compares data collected in $1g$ (Keyence sensor) and $1.8g$ (image analysis) with their respective uncertainties labeled on several points. The tail film thickness for bubbles with U_d=105, 124, 163, 173, and 208 mm/s are plotted as a function of the bubble length. As expected, δ decreases with bubble length until approximately L_b/D=6 where the thickness reaches the fully developed value. This development length (Z) was compared to predictions of Campos and Carvalho [23], which range from 13.8 to 16.1 for the current experimental results depending on the bubble velocity. Nogueira et al. [24] found that at film Reynolds numbers ($Re_{U_f} = (U_b - U_l)D/4\nu$) above approximately 80, the Campos and Carvalho correlation over-predicted their experimental results by as much as 30%. The

current data shown in Figure 3.6 suggests L_b/D~6 is required for the film thickness to stabilize, which is not inconsistent with either of these predictions.

The data is compared to predictions by Brown [19] for fully developed film thickness (δ_B) by two means. First, δ_B was calculated for each value of U_d using the measured U_b, U_l, and an assumed acceleration of 1g. This range of δ_B is illustrated by a blue area in Figure 3.6. Also shown is the prediction for U_d=163 mm/s and a/g=1, which agrees well with the measurements at these conditions. The calculations were repeated for U_d=173 and 208 mm/s at hypergravity, with the results shown by the red area and dash-dot line (U_d=173 mm/s). It is clear that the relation by Brown over-predicts the film thickness for higher gravity levels. In fact, the measurements at a/g=1.8 vary little from those collected at a/g=1. Using the correlation of Llewellin et al. [26] for fully developed film thickness of Taylor bubbles in stagnant flow, δ was calculated to be 271 μm for a/g=1 and 264 μm for a/g=1.8. Both of these values fall within the 1g prediction range of Brown and illustrate relatively little change in film thickness with increasing gravity level, which is consistent with the measurements.

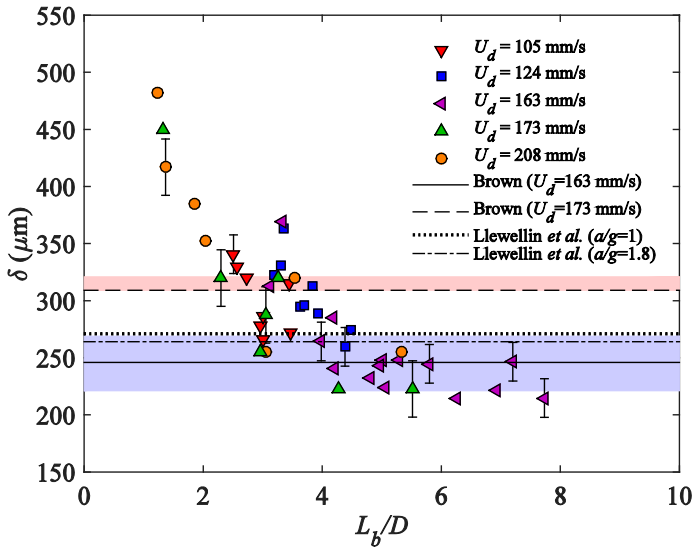

Figure 3.6: Film thickness at the bubble tail as a function of bubble length at various drift velocities for Taylor bubbles (U_d>94 mm/s).

3.2 HEAT TRANSFER

The wall heat transfer was measured for each bubble as it passed through the silicon test section where steady-state, thermally developing flow was established to ensure reproducible boundary conditions. Measurements were offset by the single-phase heat transfer observed just before the bubble enters the test section. This means of characterization was chosen to emphasize the effect of heat transfer enhancement created by the bubble passage, rather than the effect of the background flow conditions. Two heat transfer coefficient profiles ($h - h_{SP}$) obtained at a Reynolds number of Re_l=1580 (*a/g*=0.01 and 1) are plotted in Figure 3.7 as a function of axial location along the bubble, where *z/D*=0 indicates the bubble tail. The profiles shown are an average of the instantaneous profiles measured in the frame of reference of a viewer moving with the bubble tail. For both gravity levels, the heat transfer coefficient ahead of the bubble

corresponds to single-phase flow. As the liquid thins during bubble passage, a slight enhancement to the heat transfer occurs due to increased conduction and convection. Waves in the liquid-vapor interface create oscillations in the capillary bubble heat transfer (Figure 3.7a) as the fluid accelerates and decelerates within the film. At the capillary bubble tail (~z/D=0), a significant decline in the heat transfer enhancement was observed and may be attributed to a local thickening of the thermal boundary layer caused by a negative radial velocity in this region. Magnini et al. [41] also observed these flow characteristics in their numerical simulations of capillary flow within a microchannel. No such oscillations are seen in the Taylor bubble profile (Figure 3.7b) where the interface remains smooth. At the tail of the Taylor bubble, vortices are generated when the downward moving film plunges into the trailing liquid slug, inducing turbulence and a large spike in heat transfer. Vortices were not observed in the wake of the capillary bubble and the heat transfer coefficient was seen to be similar to single-phase flow. Representative IR flow visualization images of the two bubbles are shown in Figure 3.8. The wake (to the left of the image) of the capillary bubble was seen to maintain an essentially uniform temperature, suggesting that the near-wake region remained laminar and no mixing occurred. Just behind the Taylor bubble, however, clear temperature fluctuations (vortices) can be seen, indicating mixing of warmer and cooler fluid.

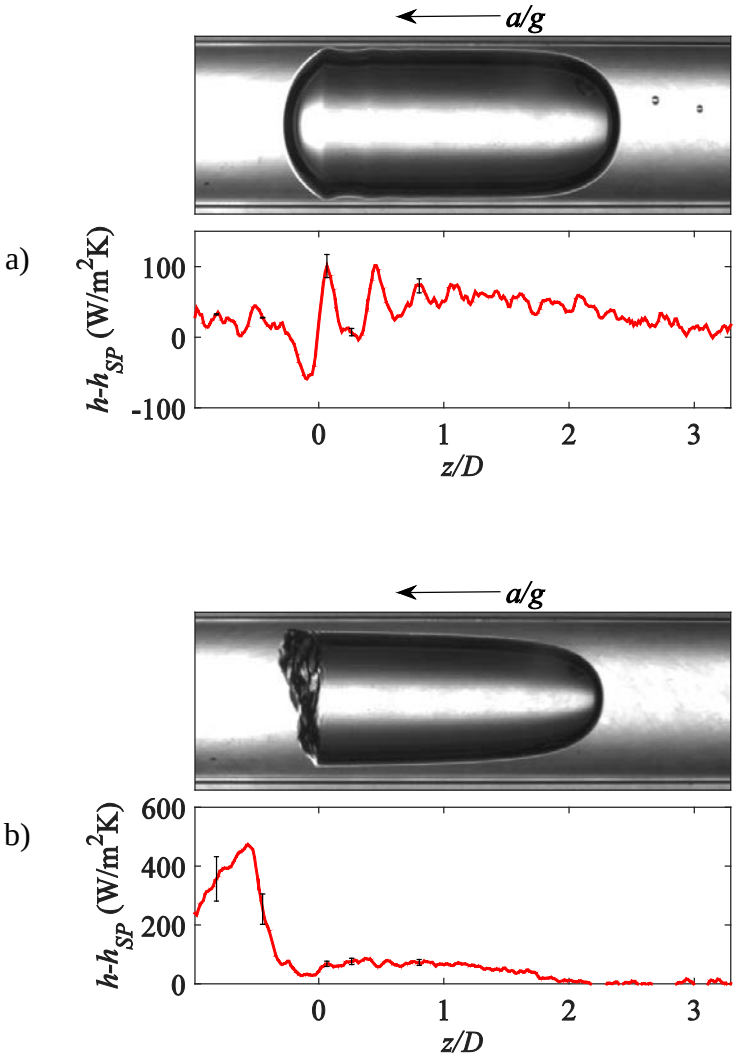

Figure 3.7: Representative heat transfer coefficient profiles: a) capillary bubble (U_d=20 mm/s, U_l=70 mm/s, L_b=16 mm, a/g=0.01, q''=800 W/m^2, h_{SP}=101 W/m^{2}K); b) Taylor bubble (U_d=124 mm/s, U_l=70 mm/s, L_b=14 mm, a/g=1, q''=1440 W/m^2, h_{SP}=148 W/m^{2}K).

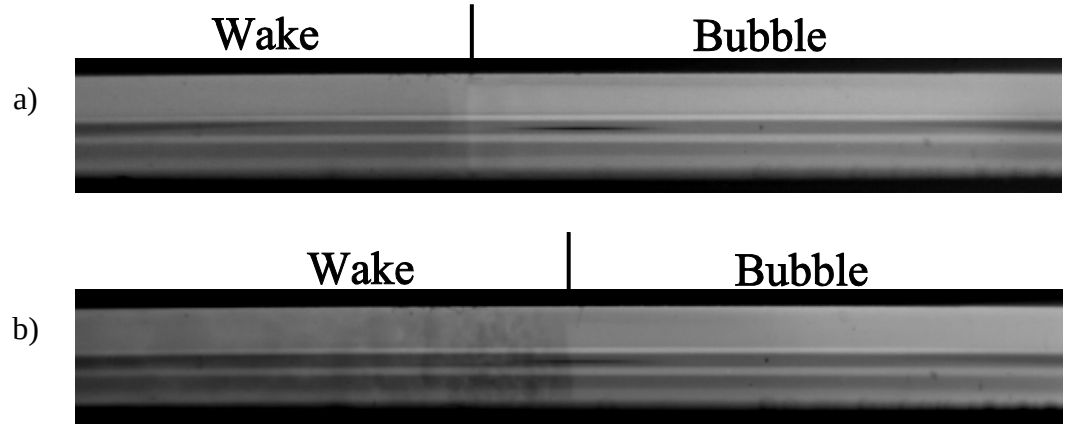

Figure 3.8: Representative IR images of the near wake region for bubbles presented in Figure 3.7: a) capillary bubble and b) Taylor bubble.

For Taylor bubbles, the bubble length was found to have little effect on the shape and magnitude of the wake heat transfer enhancement as shown in Figure 3.9. The enhancement due to five bubbles of different lengths at U_d=163 mm/s differed by an amount similar to the uncertainty in the measurements and no visible trend in the profiles was seen. If it is assumed that the relative velocity between the liquid film and trailing liquid slug is the parameter that dictates wake heat transfer, then this result is not surprising. As was seen in Figure 3.6, the liquid film thickness is essentially invariant for L_b/D>4. The bubbles presented in Figure 3.9 were very near or above this threshold, suggesting that their film velocities and subsequently wake heat transfer should also be similar. Babin et al. [34], on the contrary, found that the magnitude and length of the wake enhancement increased with bubble length for both laminar and turbulent flows. They attributed the trends to two factors. First, the higher film velocities associated with longer bubbles resulted in vortices that persisted farther downstream. Second, the increased wobbling of the tail for longer bubbles may have resulted in increased wake enhancement.

An additional explanation arises if the bubble development length is considered. The bubble length required for a fully developed liquid film was calculated for the conditions of Babin et al. [34] to be $L_b/D \approx 22$ using Campos and Carvalho [23] where the film thickness was approximated using Brown [19]. The bubble lengths considered by Babin et al. ranged from L_b/D=2–10, shorter than the L_b/D for fully developed flow, even if Z is over-predicted by the correlation. It is possible that the enhancement in wake heat transfer observed with increasing bubble length is the result of higher film velocities. As the bubbles in the current experiment were essentially fully developed, little variation in the wake heat transfer profiles are seen for the results.

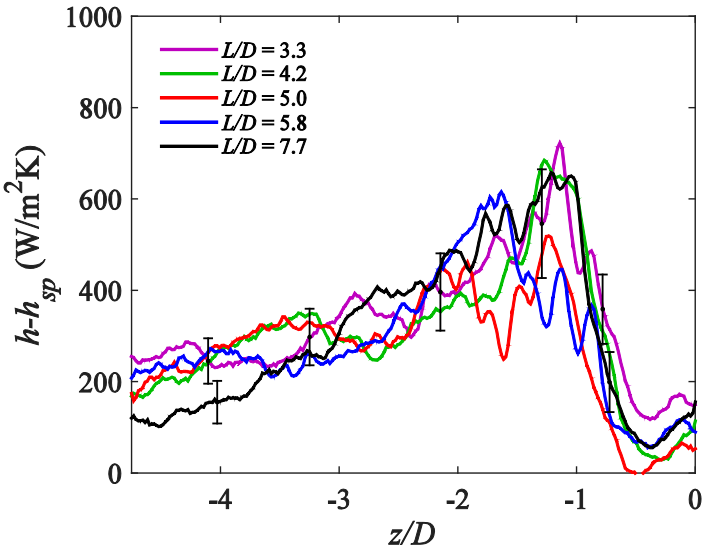

Figure 3.9: Scaled heat transfer coefficient as a function of distance behind the bubble tail for bubble drift velocity U_d =163 mm/s, tube heat flux of q"=1.0 kW/m^2, average single-phase heat transfer coefficient h_{SP}=192 W/m^{2}K, and bubble lengths L_b/D=3.2, 4.2, 5, 5.8, and 7.7.

A 2-D plot of the temporal and spatial wake heat transfer can be used to infer the local effect of vortices generated by Taylor bubbles. An example of such a plot and the wake

characteristics are shown in Figure 3.10. The resolution of the data was limited by the spatial (114 µm, 0.02*D*) and temporal (4 ms) resolution of the camera, thus creating the pattern of colored rectangles. Streaks of elevated heat transfer (labeled by black lines) were likely caused by the departure of vortices from the tail. The distance behind the tail at which the streaks appear (the penetration length from Kawaji et al. [63], L_p) is seen to vary with respect to time, a behavior that can be attributed to two factors as illustrated in Figure 3.11. First, the location of the tail (z/D=0) is determined from the average bubble velocity and does not account for wobbling of the tail. As a result, the actual location of the tail at each time may be slightly ahead or behind the average position, leading to a variation in the perceived penetration length. The second factor to be considered is the instability inherent in the plunging jet which would likely lead to oscillations in L_p even if the tail position was fixed.

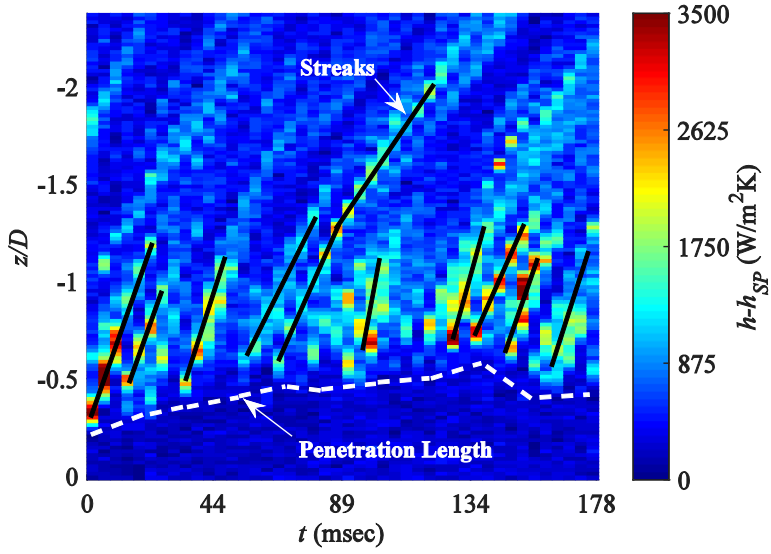

Figure 3.10: Representative wake heat transfer signature characteristics identification.

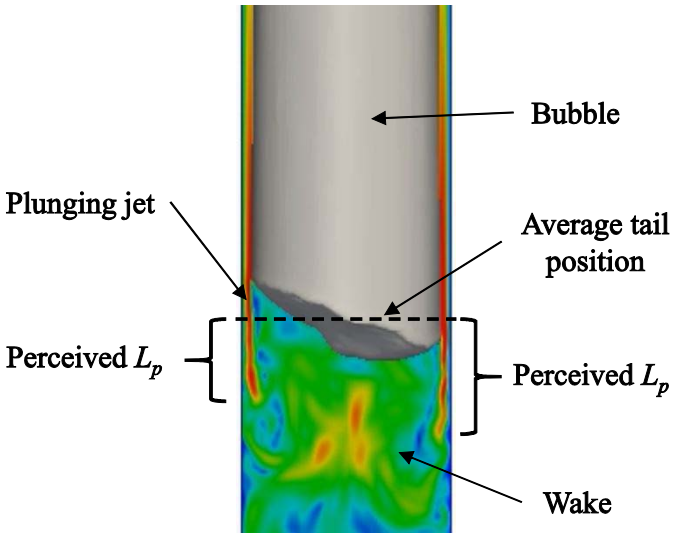

Figure 3.11: Schematic showing high velocity wall jets (red) plunging into the wake. Separation of the jet occurs at the penetration length. Bubble photograph courtesy of Dr. Mirco Magnini.

Heat transfer coefficient contours for flows with Re_l=790, 1570, and 3090 at a/g=1 and a/g=1.8 are shown in the left images of Figure 3.12 and Figure 3.13, respectively. Plots on the right of each figure illustrate the heat transfer coefficient profile at four time steps from the corresponding contour on the left. These individual profiles confirm the variation in L_p, which is seen to range from 0.5-1.5 diameters for bubbles observed at a/g=1 and 0.7-2.0 diameters for a/g=1.8. Similar results were obtained by Kawaji et al. [29] for air bubbles rising in stagnant kerosene, where L_p ranged from 0.85-1.4 diameters depending on the bubble length. Shemer et al. [30,64], while not explicitly describing the penetration length, found that the highest time-averaged radial velocity in the wake occurred at approximately 1 diameter from the tail, also consistent with the current results.

An increase in average L_p was observed for increasing Re_l (and subsequently U_f) at each gravity level. This behavior was potentially the result of the increased momentum possessed by the film as it plunged into the wake. Results of Babin at al. [34] exhibited

similar trends, but an explanation was not discussed. Kawaji et al. [29] suggested (referencing Lamb [65]) that increasing the relative velocity between the film and the wake, as occurred with increasing Re_l, would increase the rate of instability growth and potentially cause shorter values of L_p. This theory, however, based on Helmholtz instability analysis, does not account for the increased velocity of the bubble with Re_l, which may result in larger values of L_p as the bubble moves away from the injection point, despite the increased growth rate of the instability.

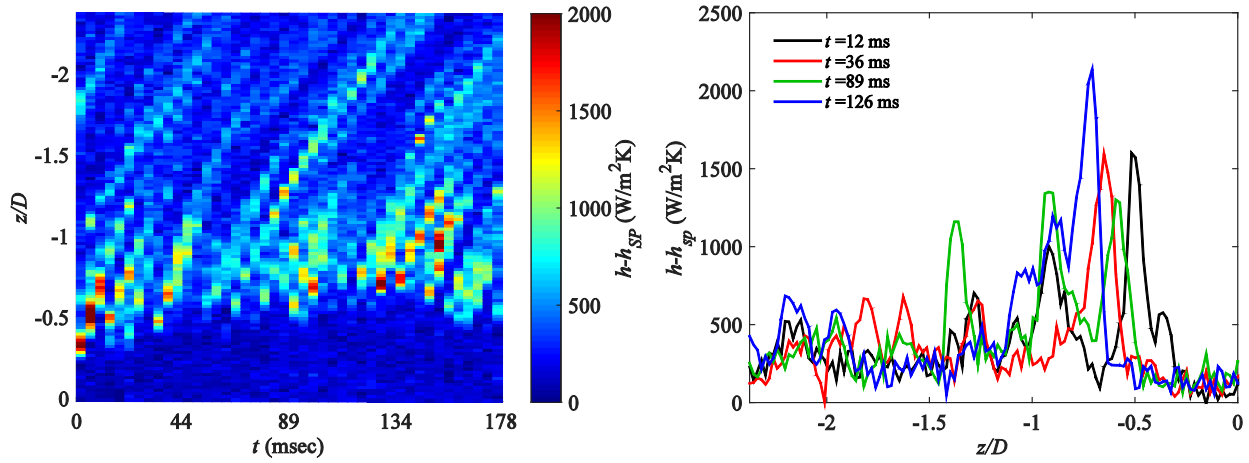

a) U_d=105 mm/s, q''=1400 W/m^2, h_{SP}=130 W/m^{2}K

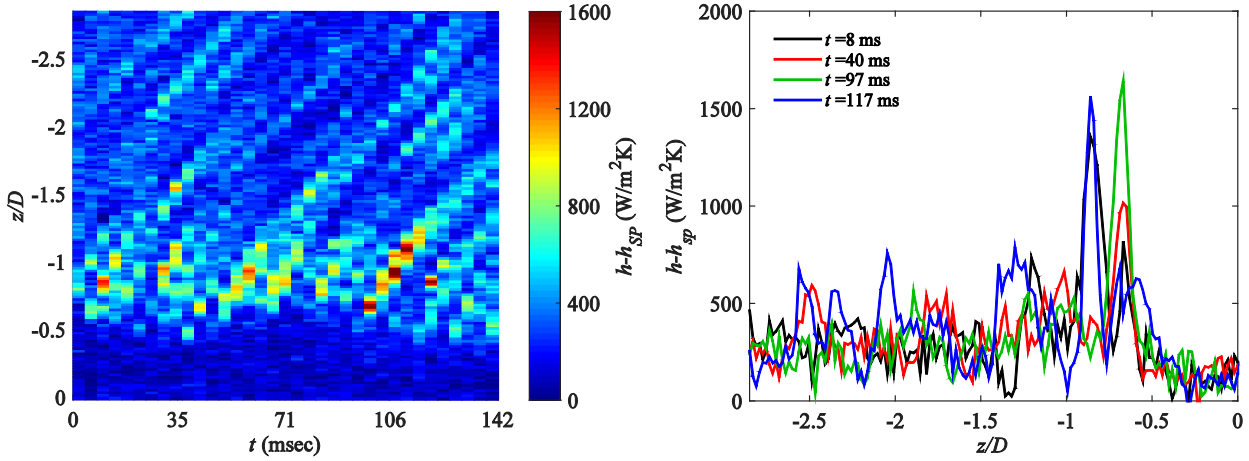

b) U_d=124 mm/s, q''=1470 W/m^2, h_{SP}=148 W/m^{2}K

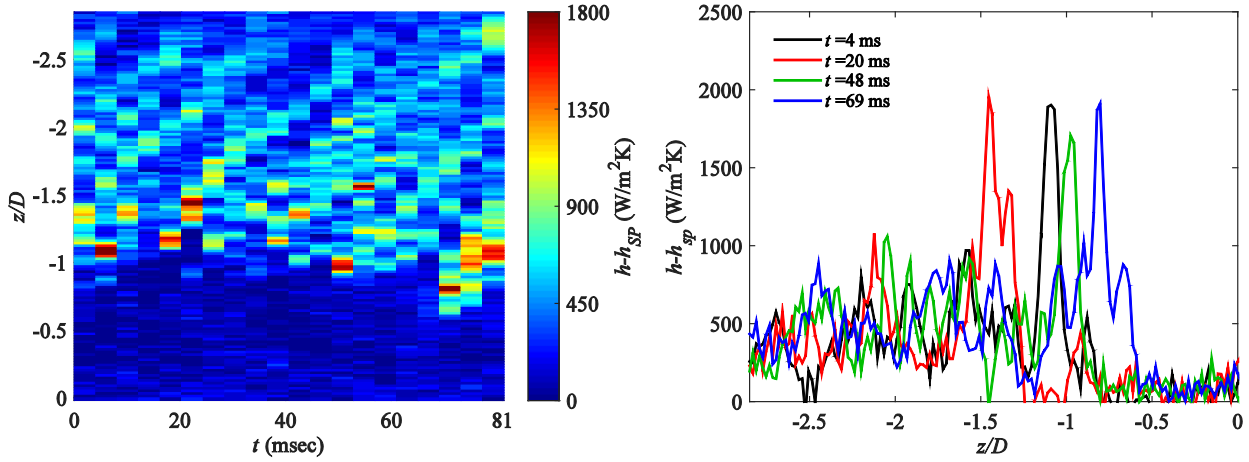

c) U_d=163 mm/s, q''=1700 W/m^2, h_{SP}=192 W/m^{2}K

Figure 3.12: Wake heat transfer coefficient contours (left) and representative profiles (right) at a/g=1 for various conditions.

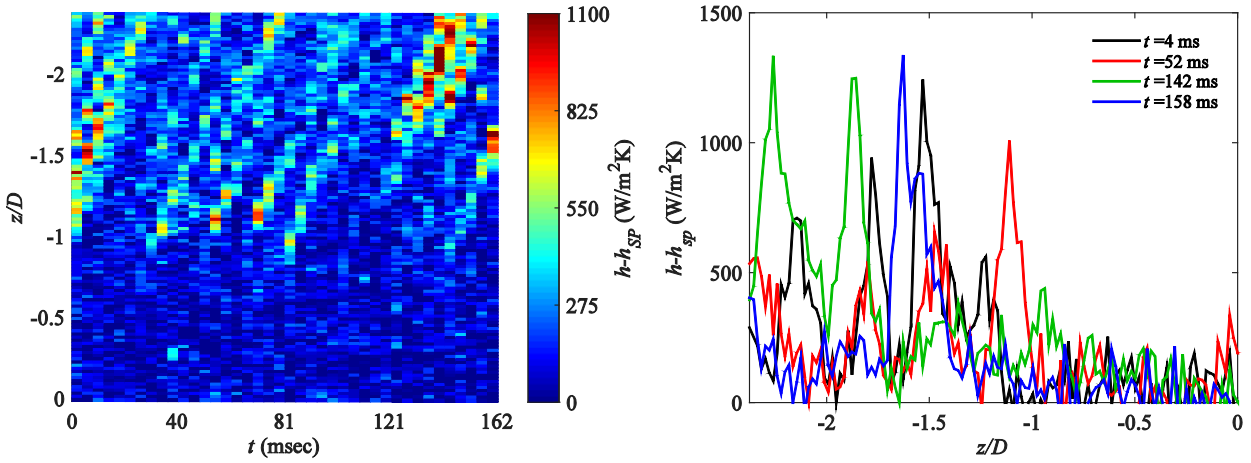

a) U_d=144 mm/s, q''=1140 W/m^2, h_{SP}=104 W/m^{2}K

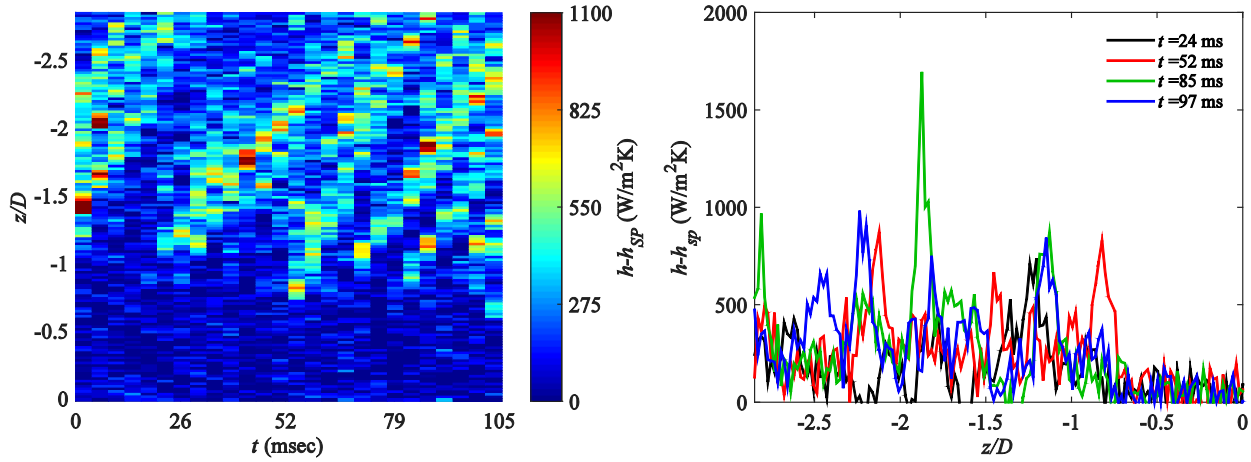

b) U_d=173 mm/s, q''=1330 W/m^2, h_{SP}=112 W/m^{2}K

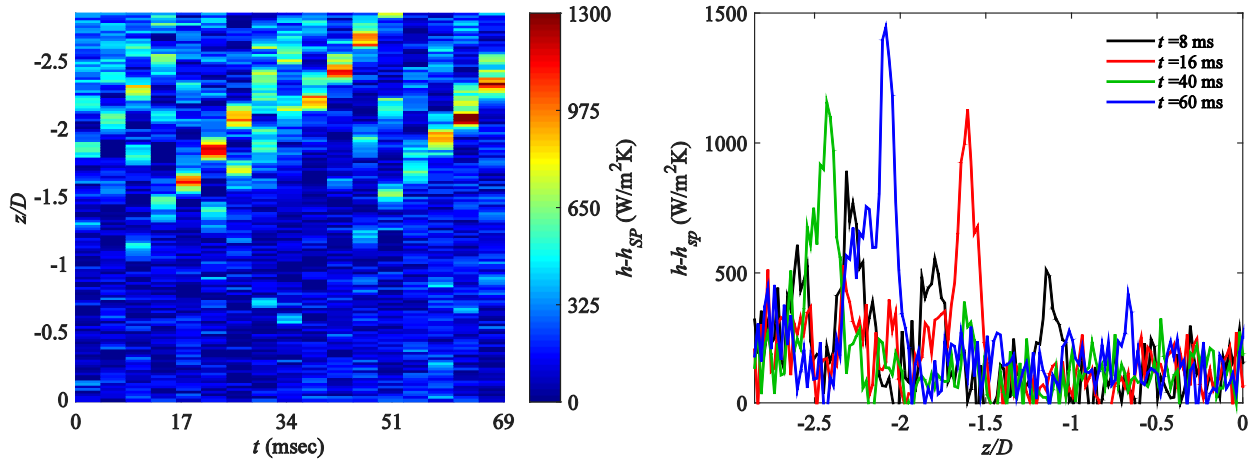

c) U_d=208 mm/s, q''=1320 W/m^2, h_{SP}=146 W/m^{2}K

Figure 3.13: Wake heat transfer coefficient contours (left) and representative profiles (right) at a/g=1.8 for various conditions.

The vortex frequency, f_v, was determined by counting the number of streaks in each contour and dividing by the time over which they occurred. At each U_p, f_v was found by averaging the calculated frequencies for a number of contour plots (between 2 and 13 plots) at each flow condition. Attempts were made at performing Fourier analyses on the streaks. However, due the limited length of the acquired signals (resulting from the limited test section length) and quasi-periodicity of vortex generation, the results were inconclusive. The calculated frequency results should serve as an approximation of the wake turbulence. The frequency increased monotonically with increasing U_p as seen in Figure 3.14, and was independent of gravity level for a/g=1 and 1.8. It is possible that the two bubbles observed under Martian gravity (a/g=0.34) fall within a transitional region between capillary and Taylor bubble hydrodynamics and therefore do not align with the higher gravity data. A linear fit to the current a/g=1 and 1.8 data suggests that a critical plunging velocity ($U_{p,cr}$) of 127 mm/s exists where vortices begin to appear. For this experiment, $U_{p,cr}$=127 mm/s corresponds to a critical drift velocity of $U_{d,cr}$=34 mm/s and a critical drift Reynolds number of $Re_{U_{d,cr}} = 741$. Pinto et al. [28] proposed $Re_{U_{d,cr}} = 525$ as the boundary for incipience of vortex shedding, which compares fairly well with the current result. The frequency can be generalized using the Strouhal number (St), defined here as $St = \frac{f_v \delta}{(U_p - U_{p,cr})}$, to be St=0.018±0.003.

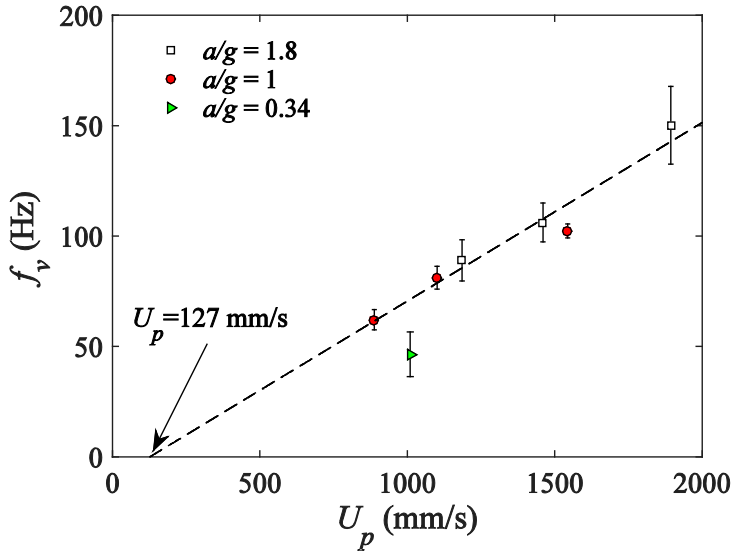

Figure 3.14: Wake vortex frequency as a function of the relative velocity between the film and bulk liquid velocity for *a/g*=0.34, 1, and 1.8.

The velocity with which the vortices moved away from the tail in the bubble reference frame, U_v', was determined from the streaks in Figure 3.12 and Figure 3.13 by measuring their slope in the near-wake region. The length of the near-wake region varied depending on the liquid velocity and gravity level. At U_d=105 mm/s (Figure 3.12a), for example, the near-wake region was defined as approximately $-1.2 \leq z/D \leq -0.5$, while at U_d=208 mm/s (Figure 3.13c) it was $-2.8 \leq z/D \leq -1.5$. U_v' is plotted in Figure 3.15 as a function of the wall velocity U_w'. Vortices are shown to move faster than the wall and increase monotonically regardless of gravity level. This is not surprising given that the liquid velocity near the wall is dominated by the remnants of the plunging jet, as shown in Figure 1.4. The fluid motion responsible for the streaks likely remains close to the wall and is convected downstream at a velocity greater than the wall velocity.

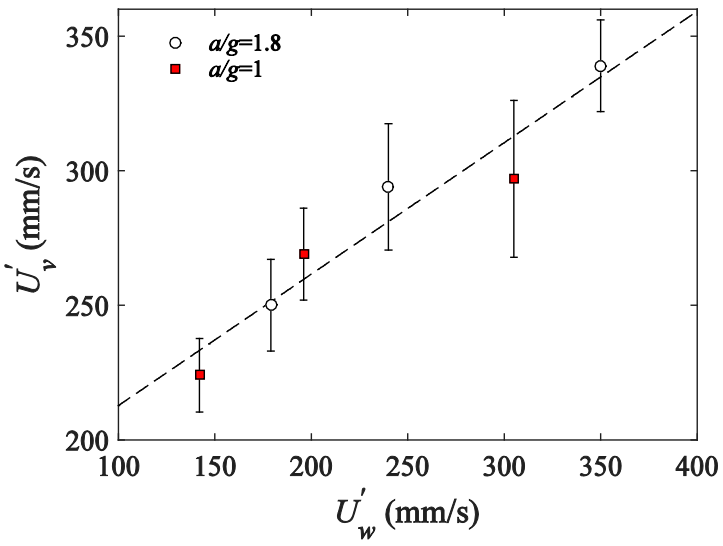

Figure 3.15: Velocity of vortices as they move away from the bubble tail (fixed reference frame at bubble tail) with respect to bubble velocity at *a/g*=1.8 and *a/g*=1.

The various time-resolved wake characteristics that have been gleaned from Figure 3.12 and Figure 3.13 can be used to describe time-averaged heat transfer results. To further compare the effect of drift velocity and gravity on the wake heat transfer, data were averaged with time for 5-20 bubbles at each test condition to obtain the profiles shown in Figure 3.16. The near-wake region (Figure 3.16a) is characterized by the rise of the heat transfer coefficient enhancement behind the bubble tail. The penetration length is seen to increase with U_d for both gravity levels, with *a/g*=1.8 exhibiting slightly longer L_p than *a/g*=1. Both observations may be attributed to the increase in liquid film momentum with increasing drift velocity and gravity level.

The peak heat transfer enhancement is also seen to vary with drift velocity, generally decreasing with increasing U_d at each acceleration. It can be noticed that the peak behavior over both accelerations appears to coincide with the relative distribution of L_p at each drift velocity. At *a/g*=1.8, L_p is seen to vary widely (Figure 3.13), thereby creating more diffuse

and smaller magnitude peaks than a/g=1 (Figure 3.12). Definitive elucidation of these trends requires coupling of local flow field measurements, which were not available in this study.

The far-wake region (Figure 3.16b) shows a continuation in enhancement decay to the single-phase value far downstream of the bubble. The distance behind the tail at which single-phase heat transfer is re-established (the calming length, L_c) is seen to depend on the liquid Reynolds number and the gravity level. This behavior may be attributed to the redevelopment of the thermal boundary layer in the wake after its disruption by vortices as was shown by Babin et al. [34]. For both 1g and 1.8g accelerations, L_c/D was smallest at Re_l≈800, increased to its largest values at Re_l=1570, then decreased to moderate lengths at Re_l=3058. Assuming laminar flow, increasing Re_l from approximately 800 to 1570 would have resulted in longer thermal and hydraulic redevelopment lengths. Increasing Re_l further to 3080, where the flow was likely transitional, would have caused a decrease in the redevelopment length due to the onset of turbulence. The growth in L_c/D with acceleration may be attributed to the increased influence of natural convection at hypergravity ($Ra_{D,1.8g}/Ra_{D,1g} \approx$ 2.8, 2.1, and 2.3 for $Re_l = 800$, 1570, and 3090, respectively) which effectively increased the Reynolds number near the wall and led to a longer development length.

a)

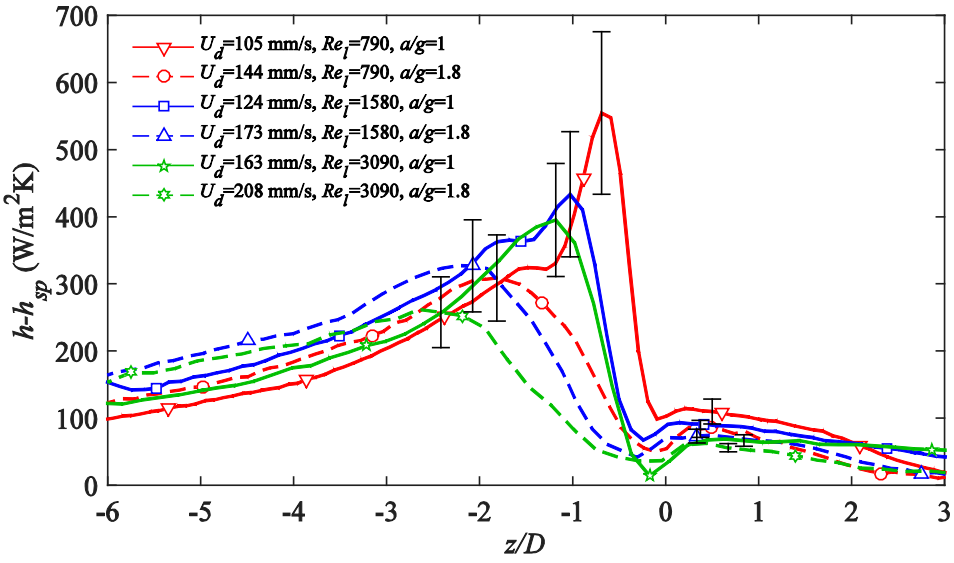

b)

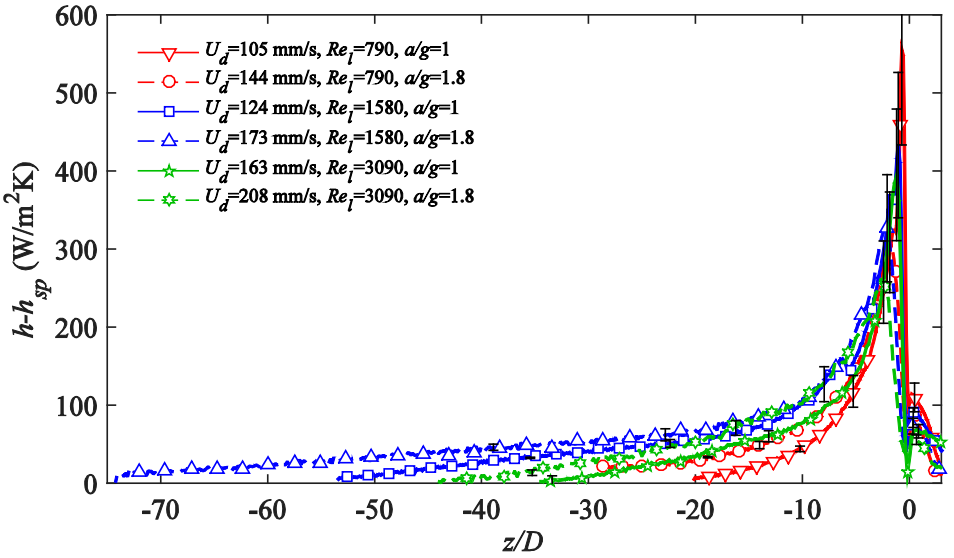

Figure 3.16: Heat transfer coefficient enhancement as a function of distance behind the bubble tail for a) near-wake region and b) far-wake regions at the conditions: U_d=105, 124, 163, 144, 173, and 208 mm/s; tube heat flux of q''=1400, 1470, 1700, 1140, 1330, and 1320 W/m^2, respectively; average single-phase heat transfer coefficient of h_{SP}=130, 148, 192, 104, 112, and 146 W/m^{2}K, respectively.

3.3 COMPARISON TO NUMERICAL SIMULATIONS

The experimental study presented above succeeded in determining major characteristics of the heat transfer and flow patterns around rising elongated bubbles. There were, however, limitations to the experiment that prevented portions of the fundamental physics from being fully understood. Specifically, the local, time-resolved flow and temperature fields in the near-wake region, which are invaluable to characterizing the movement of vortices, were unobtainable given the experimental setup. Results such as these are more easily captured with the help of numerical simulations from which many parameters may be detailed. For this reason, a collaboration was formed with Dr. Mirco Magnini working with Prof. John Thome at École Polytechnique Fédérale de Lausanne (EPFL) in Lausanne, Switzerland. Dr. Magnini has previously developed simulations in ANSYS Fluent for slug flow in microchannels that have compared well with the literature [41,42,66]. A detailed explanation of the simulation numerical framework can be found in Dr. Magnini's microchannel publications and in a recent UMD/EPFL collaborative conference paper [67]. His numerical framework was adapted for use with the current experimental setup to provide a comparison to the collected data and to aid in understanding its meaning.

3.3.1 Simulation Parameters

In an effort to match numerical and experimental results as closely as possible, a set of flow, heating, and bubble parameters were agreed upon to serve as boundary and initial conditions for the simulations. These details were determined from the experiments completed as part of this study and are summarized below in Table 3.3. The numerical boundary conditions were as follows. Laminar fully-developed (Poiseuille) hydraulic conditions were assumed at the tube entrance for both diabatic and adiabatic simulations.

Bubbles of specified length were initialized at the entrance and simulated to rise through the channel length (16D for adiabatic, 40D for diabatic). For diabatic simulations, the tube wall was heated with a constant heat flux. Natural convection was enabled to account for buoyancy effects in the liquid.

Table 3.3: Summary of comparative experimental and numerical parameters.

Parameter	Value
G [kg/m^{2}s]	50 and 100
q'' [W/m^2]	0 and 1380
L_b [mm]	18 and 36
g [m/s^2]	1 and 1.8

3.3.2 Shape and Hydrodynamics Comparison

As was illustrated in the experimental results discussed previously, the behavior of the bubble and its surrounding flow field heavily influence the bubble's effect on the heated tube through which it rises. Consequently, it is important that the bubble shape and hydrodynamics captured by the simulations closely agree with experiments so that heat transfer comparisons can be appropriately made. Representative bubble images from each case are compared in Figure 3.17 for G=50 kg/m^{2}s at normal gravity. The experimental bubble was visualized in the adiabatic section, while the bubble from the simulation was observed in a heated tube. The heat flux applied to the wall was small (q''=1380 W/m^2) and was assumed to not affect the bubble shape. It is clear that the general shapes of the bubbles are quite similar, including the deformation of the tails as they wobbled. More quantitative comparisons were also made, including the development of the liquid film. The

experimentally measured film thickness is plotted as a function of distance from the bubble nose (the measured bubble is shown above the plot) in Figure 3.18 along with the corresponding thickness from the simulations. Despite the difference in heating conditions, the film thicknesses are seen to agree within the uncertainty of the experimental measurements.

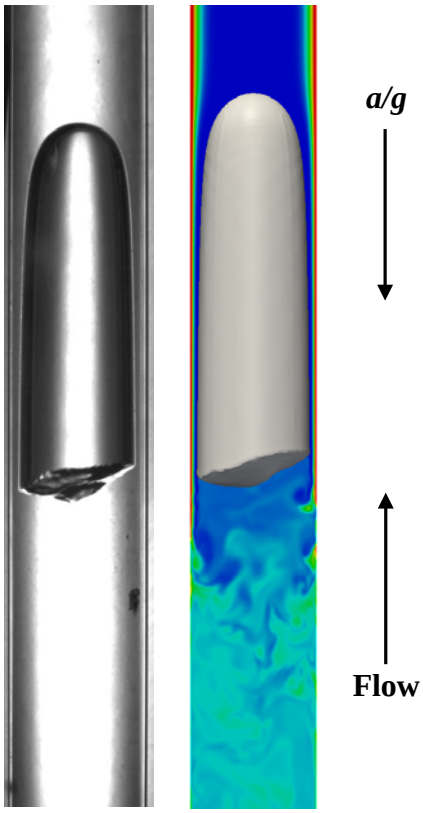

a) b)

Figure 3.17: Comparison of representative bubbles under normal gravity conditions with U_l=37 mm/s from: a) experiments (L=17 mm, adiabatic); b) simulations (L=18 mm, q''=1380 W/m^2). Simulation image courtesy of Dr. Mirco Magnini.

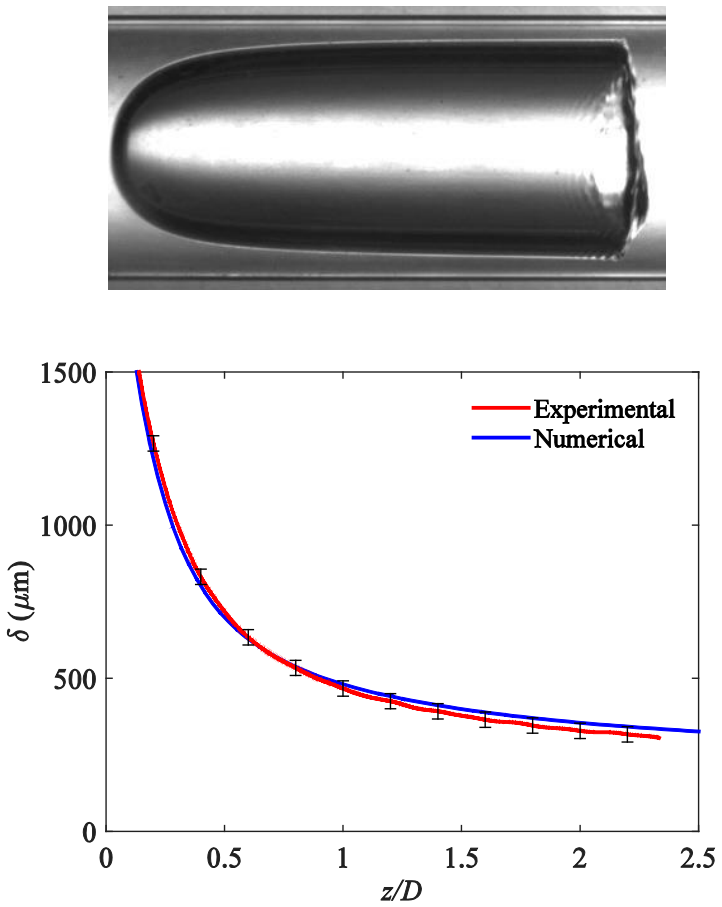

Figure 3.18: Comparison of measured and simulated film thickness for a short bubble (L_{exp}=14 mm, L_{num}=17 mm) rising within liquid with U_l=37 mm/s at a/g=1. The bubble from which the experimental film thickness was measured is shown above the figure. Numerical data courtesy of Dr. Mirco Magnini.

The bubble velocity was compared for various liquid mass fluxes at both adiabatic and diabatic tube heating conditions. Bubble tracking data from the diabatic simulations illustrated a decrease in velocity as the bubble rose in the tube due to flattening of the liquid velocity profile caused by natural convection. A variation was not seen for experimentally measured velocity, but the distance over which the bubble was viewed was shorter than the simulations, which may have truncated the decelerating behavior in the data. Due to this discrepancy, a representative value of U_b was determined for the simulations by averaging the velocity profile over the length that would be visible had it been measured using the

experimental apparatus. It can be seen in Figure 3.19 that regardless of the thermal boundary condition, both simulation and experimental velocity values agree well with each other and linearly increase with U_l, as expected.

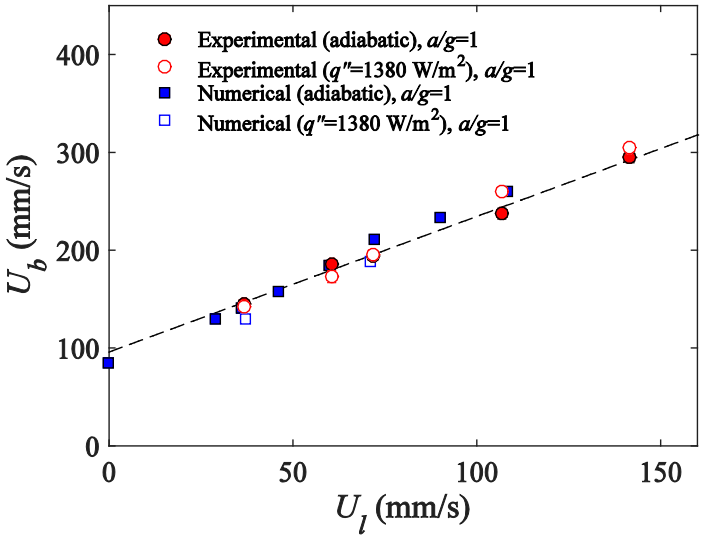

Figure 3.19: Comparison of experimentally measured bubble velocities to those obtained from numerical simulations. Numerical data courtesy of Dr. Mirco Magnini.

3.3.3 Heat Transfer Comparison

The general agreement in bubble hydrodynamics between the two methods of study provided encouragement that the simulation results were representative of the experiments. Further evidence was attained by comparing wake heat transfer contours in Figure 3.20 for G=50 kg/m^{2}s, a/g=1 and q''=1380 W/m^2. It can be seen that, like the experiments, the contours attained from the simulations were characterized by streak patterns where the highest heat transfer coefficient occurred near the tail. The streaks exhibit a higher velocity nearer the bubble (near-wake), then transition to a lower velocity downstream (far-wake).

Calculated vortex velocities from the simulations were found to agree well with those from the experiments (near-wake: $U'_{v,exp}$=224±11 mm/s, $U'_{v,sim}$=210±13 mm/s; far-wake: $U'_{v,exp}$=119±6 mm/s, $U'_{v,sim}$=115±16 mm/s). The penetration lengths were also found to be similar, ranging from approximately $z/D = -0.5$ to $z/D = -1.5$ in both cases.

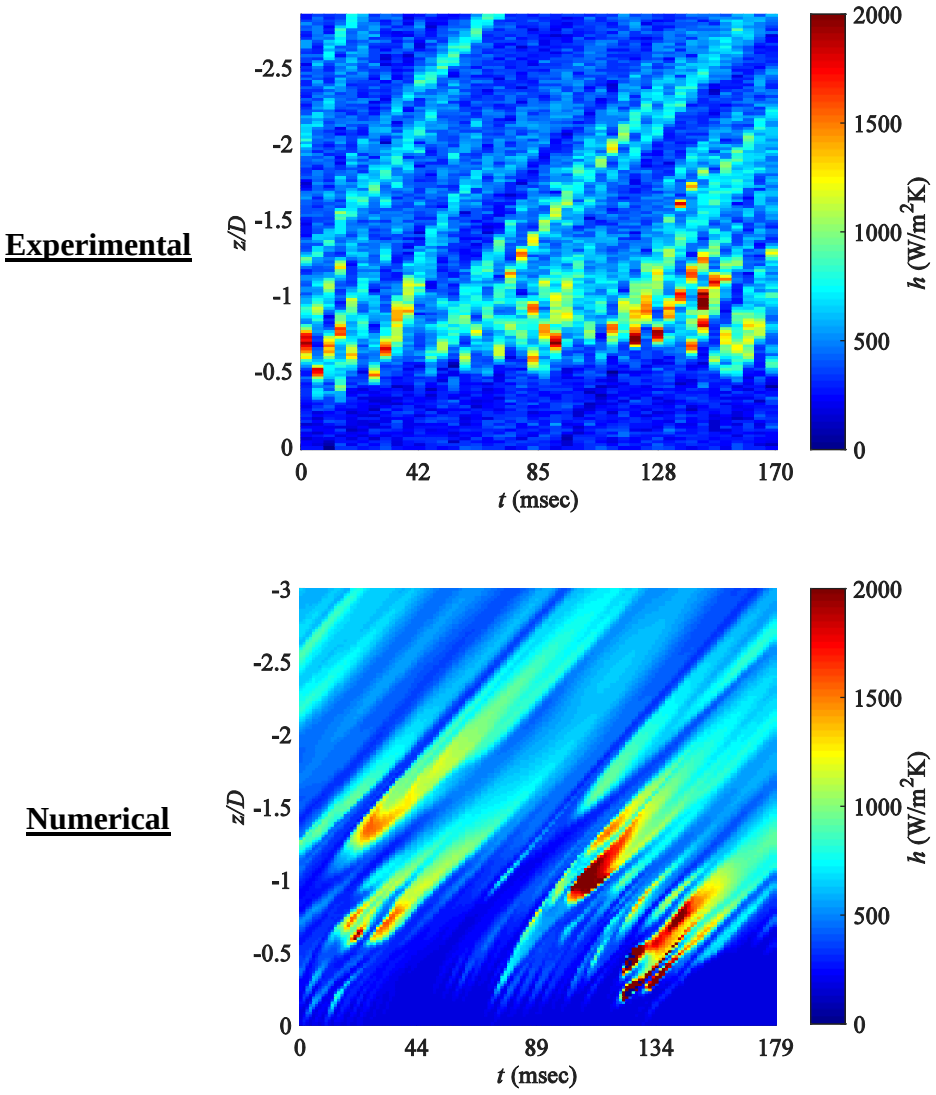

Figure 3.20: Comparison of wake heat transfer coefficient profiles obtained from experiments and numerical simulations for G=50 kg/m^{2}s, q''=1380 W/m^2, and a/g=1. Numerical data courtesy of Dr. Mirco Magnini.

Wake heat transfer comparisons made using the contours, while serving to validate both experimental and numerical results, do not take full advantage of the simulation data. To more completely understand the physics of the bubble wake, the instantaneous flow and temperature field can be plotted from the simulations, as shown in Figure 3.21 where $z/D = 0$ indicates the tail position and $z/D < 0$ is the wake. The velocity field is indicated by the arrow vectors and the temperature field is illustrated using the color map. Temperatures were offset by the inlet temperature of the heated region, where the liquid was subcooled by approximately 4°C. Near the top of the figure ($-0.5 < z/D < 0$), a warm, circular jet from the film can be seen to plunge into the cooler liquid behind the bubble. Note that as the contour was created from a cross-sectional view, the circular jet appears as two jets, one on each side of the tube ($z/D = \pm 0.5$). The jet becomes unstable as it moves downstream and is sheared from the wall, allowing colder fluid to replace it. Gradually the liquid behind the bubble mixes to create a more uniform temperature profile within the tube. The effect of the temperature and flow evolution was evaluated in Figure 3.22, where the local heat transfer coefficient at the tube wall is plotted vs. axial distance for the two "halves" of the channel.

The heat transfer coefficient is observed to be relatively small while the warm jet remains intact near the tail of the bubble. The jet acts as a barrier for the wall by preventing cool liquid from nearing the surface, thereby maintaining a thick thermal boundary layer. It is only when the jet begins to break up, at approximately $z/D = -0.75$ for both walls, that mixing of the fluid occurs and the heat transfer rises. Peaks in the heat transfer coefficient coincide with regions where the fluid motion transports pockets of cool liquid to the wall creating a high temperature gradient.

Relating this insight to experimental results, the heat transfer behavior in the wake contours can be better explained. First, the penetration length was directly related to the wobble of the bubble tail and the destabilization of the circular jet. Due to the complex and transient nature of the hydrodynamics, it is not surprising that L_p varied with time in Figure 3.12 and Figure 3.13. Second, the distribution of heat transfer coefficient with respect to *z/D* can be explained by the evolution of the temperature field within the tube. Just after the tail, where the highest heat transfer was observed, the liquid that was brought to the wall from the center of the channel was relatively cold compared to the liquid near the tube surface. Farther downstream, mixing created a more uniform temperature field and a smaller temperature difference existed between the wall and the bulk fluid. This, as well as the decay of turbulence, led to a steady decline in the heat transfer coefficient.

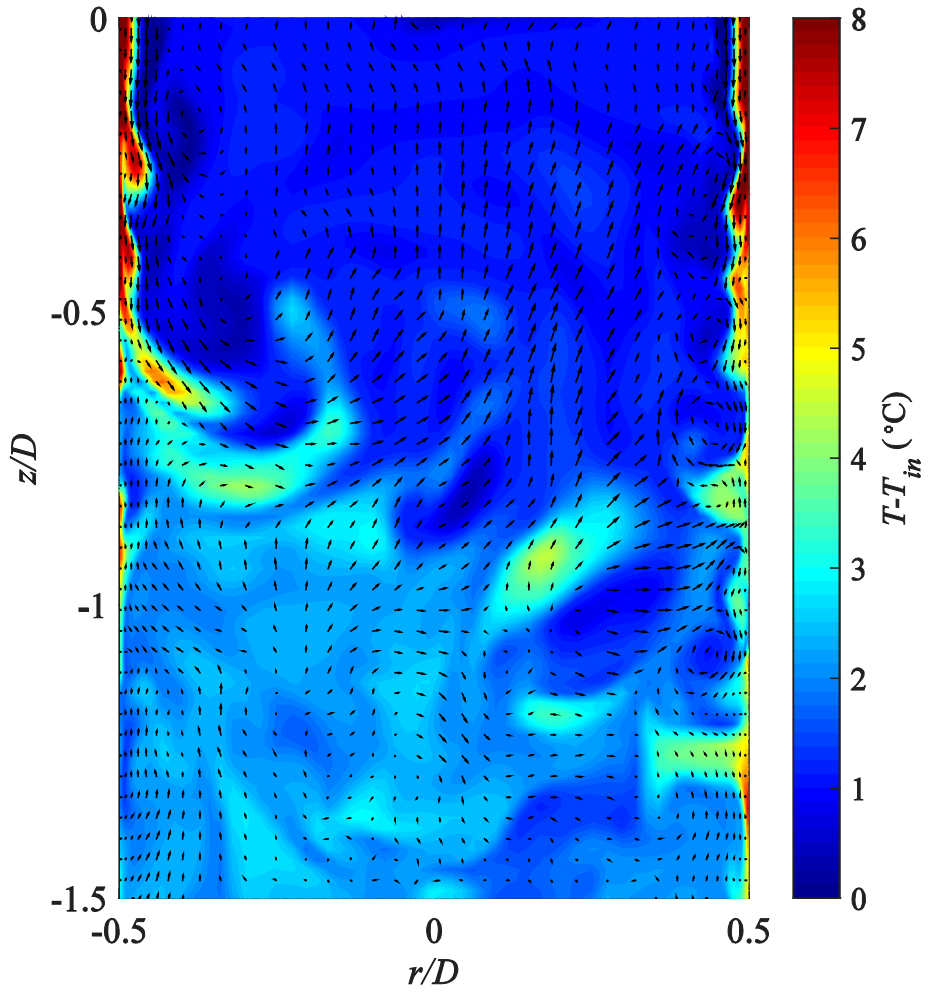

Figure 3.21: Instantaneous flow and temperature field simulated for a bubble with the conditions: G=50 kg/m^{2}s, L/D=6, q''=1380 W/m^2, T_{in}=55.2ºC, T_{sat}=59.5ºC, and a/g=1. Data courtesy of Dr. Mirco Magnini.

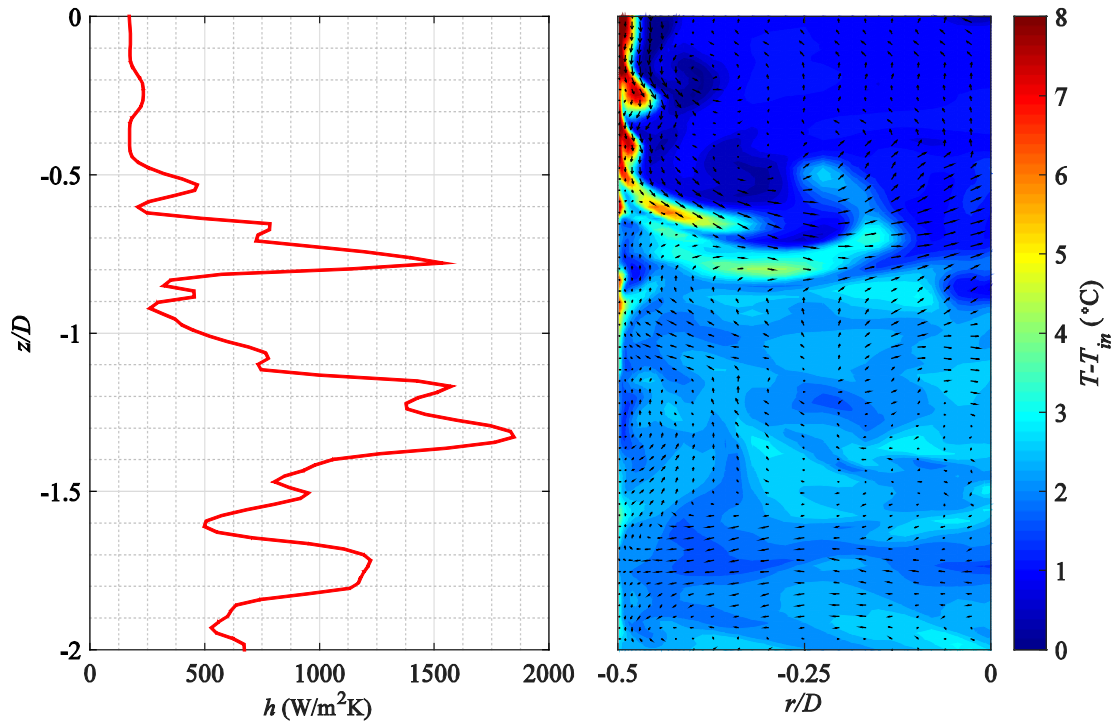

a) Left wall

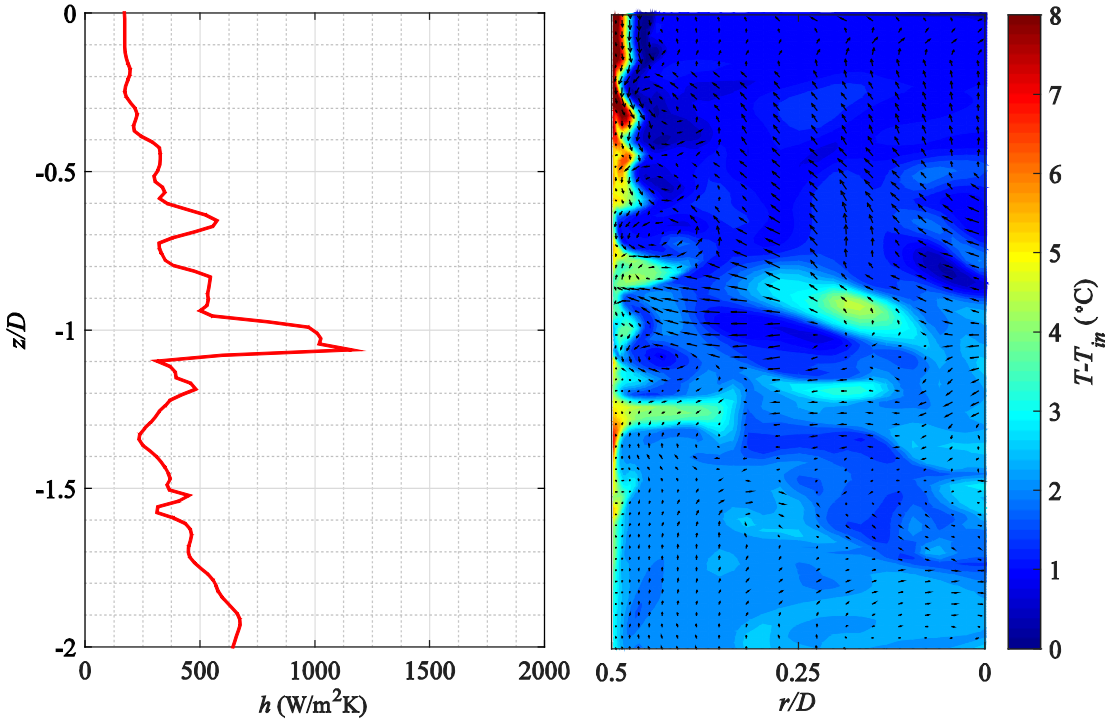

b) Right wall

Figure 3.22: Local heat transfer coefficient plotted as a function of axial position in the wake for the a) left and b) right sides of the cross-section. The averaged bubble parameters were G=50 kg/m^{2}s, L/D=6, q''=1380 W/m^2, T_{in}=55.2ºC, and a/g=1. Data courtesy of Dr. Mirco Magnini.

In conclusion, the comparisons presented above showed that experimental results can be well simulated by Dr. Magnini's numerical framework. Agreement was seen in both heat transfer and hydrodynamic characteristics for the simulated conditions currently available. Furthermore, local wake temperature data from the simulations helped to explain the behavior seen in the heat transfer contour plots. Additional simulation cases will be completed as part of the collaboration to determine the effects of liquid mass flux and gravity level on the heat transfer around a single bubble.

3.4 IMPLICATIONS FOR SLUG FLOW MODEL DEVELOPMENT

As one of the main goals of this research was to guide the development of more realistic and accurate models for slug flow heat transfer, it is important to discuss how the results contribute to that end. It has been shown that even for a simplified case of one Taylor bubble passing through a heated tube, the hydrodynamics and their effect on heat transfer are quite complex. Consequently, one would expect that the model for this regime would need to be fairly advanced. It is pertinent to inspect previous models for their means of handling the complexities which may be incorporated into new, more thorough models.

Several models have been developed to describe slug flow, including the aforementioned three-zone model by Thome et al. [40] for microchannels. The model breaks down an individual bubble's unit cell into a liquid slug, the bubble, and a vapor slug which occurs if the liquid film around the bubble dries out. Given that the model was developed for capillary flow, the assumptions made of homogenous flow and uniform saturation conditions are reasonable for that situation. As has been shown, however, these assumptions are not valid for slug flow with Taylor bubbles which makes the extrapolation of the model to flow of this type less appropriate.

A model for macroscale, gas/liquid, vertical-upward slug flow was developed analytically by Barnea and Yacoub [35] in which an energy balance was performed on fluid cross-sections to determine the local wall and fluid temperatures as a function of time. They suggested that the transfer of heat from the wall to the fluid was largely dependent on the local velocity within the slug and film regions. The heat transfer coefficient in each was approximated using Colburn's [68] correlation for forced convection inside tubes,

$$\frac{hD_h}{k_l} = 0.023\left(\frac{\rho D_h U}{\mu_l}\right)^{0.8}\left(\frac{c_{p,l}\mu_l}{k_l}\right)^{0.33} \tag{12}$$

where D_h is the hydraulic diameter (D in the slug, 2δ in the film) and U is the mean liquid velocity for either the slug or film region.

In an effort to predict peaks in heat transfer coefficient for near-zero vapor quality flows, Barbosa and Hewitt [69] developed a model for large scale turbulent liquid/vapor slug flow with Taylor bubbles. Their methodology utilized superposition to approximate the average heat transfer coefficients for the slug and film regions. In both cases, empirical correlations were superimposed to account for convective and nucleate boiling contributions.

Within the slug, Barbosa and Hewitt suggested the Dittus-Boelter correlation for turbulent forced convection with a modified Reynolds number to account for entrainment of small bubbles. The calculated convective heat transfer coefficient was multiplied by Chen's [54] two-phase enhancement factor, F. Heat transfer from nucleation was approximated with the Forster and Zuber [70] correlation multiplied by Chen's [54] nucleate boiling suppression factor, S. In the absence of nucleation and entrained bubbles (as in the current experimental results), this formulation for the wake heat transfer provides a constant heat transfer coefficient dependent on the bulk liquid velocity within the slug.

The suggested prediction for the average convective film heat transfer was a correlation by Chun and Seban [71] for a turbulent falling film on the outside of a vertical heated cylinder,

$$\frac{h}{k_l}\left(\frac{\mu_l^2}{\rho_l^2 g}\right)^{1/3} = 0.0038\left(\frac{4\rho_l U_f \delta}{\mu_l}\right)^{0.4}\left(\frac{\mu_l c_{p,l}}{k_l}\right)^{0.65} \tag{13}$$

Nucleation was again accounted for through Forster and Zuber's correlation and Chen's suppression factor. An interesting caveat relating to the film region was also included in the development of the model's energy balance equations. The assumption was made that the liquid supplied to the film of a bubble by the leading liquid slug originates from an annular region located at the wall of the tube. A schematic of this theory (originally proposed by Orell and Rembrand [72]) is provided in Figure 3.23. The area at the center of the tube is forced upwards by the bubble, while the annular wall region flows downward forming the film. Barbosa and Hewitt extended this idea to the temperature field, hypothesizing that the average temperature within the film was higher than that of the slug because the cooler liquid from the core does not enter the film.

It is evident from this summary of the currently available slug flow models that room for improvement exists in the prediction methods of heat transfer coefficient, especially in the wake where the mechanisms shown in this work are not addressed. While the models typically apply modified channel flow correlations, a more realistic approximation of plunging film heat transfer is the slot wall jet geometry (Figure 3.24) often seen in film cooling applications.

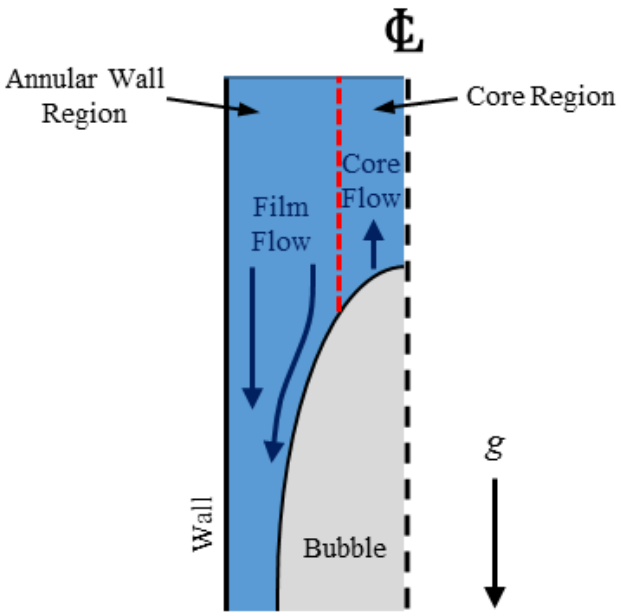

Figure 3.23: Schematic of slug liquid partitioning proposed by Orell and Rembrand [72].

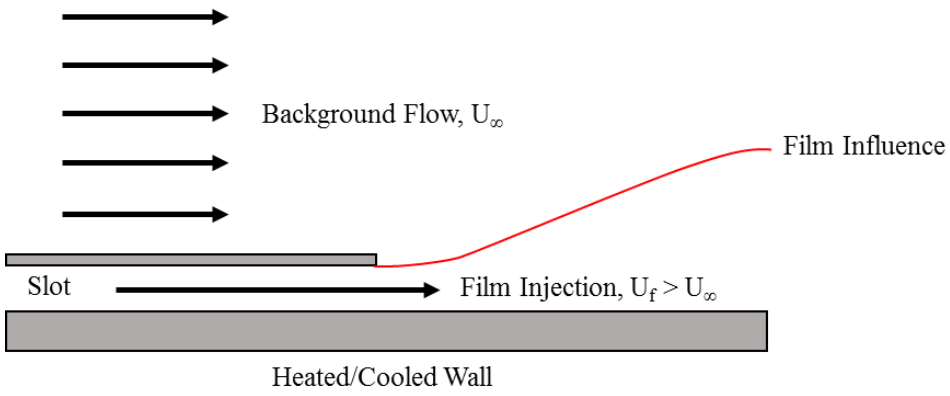

Figure 3.24: Schematic of slot injection geometry, adapted from Bittlinger et al. [73].

For the case of combustion chamber cooling, a thin film of cool air is injected via a slot near the chamber wall to protect it from the hot combustion gasses passing in the free stream. Several researchers have investigated the local heat transfer coefficient along a cooled wall in the presence of flowing heated air with various blowing ratios. The blowing

ratio, M, is defined as $M = \rho_f U_f / \rho_\infty U_\infty$, where ρ_f is the film fluid density, U_f is the film velocity, ρ_∞ is the bulk fluid density, and U_∞ is the bulk fluid velocity. Bittlinger et al. [73] found that the heat transfer coefficient increased sharply just after the film injection and then decayed to a steady state value as the film diffused downstream as shown in Figure 3.25. These profiles are remarkably similar to those found experimentally in Figure 3.16 for rising Taylor bubbles. Bittlinger et al. noted that above a blowing ratio of 1.6 (U_f/U_∞>1) the peak in heat transfer coefficient increased with M. This finding is contrary to the current results, but it is hypothesized that the decrease in peak heat transfer coefficient for Taylor bubbles may be related to a transition of the background liquid flow from laminar to turbulent regime. The film cooling experiments were conducted under fully turbulent conditions.

Seban [74] developed a correlation for local heat transfer coefficient downstream of the film injection for U_f/U_∞>1 and a constant heat flux condition at the wall,

$$\begin{aligned} \frac{h}{\rho_f U_f c_{p,f}} &= 0.10 \left(\frac{U_f \rho_f s}{\mu_f}\right)^{-0.3} \left(\frac{z}{s}\right)^{-0.3} \qquad \text{for } z/s < 40 \\ \frac{h}{\rho_f U_f c_{p,f}} &= 0.41 \left(\frac{U_f \rho_f s}{\mu_f}\right)^{-0.3} \left(\frac{z}{s}\right)^{-0.6} \qquad \text{for } z/s > 40 \end{aligned} \tag{14}$$

where s is the slot height. The heat transfer coefficient was defined as $h = q"/(T_w - T_{aw})$, where T_{aw} is the adiabatic wall temperature (the temperature of the wall without heating or cooling given the same flow conditions). A comparison is made between Seban's prediction for the modified heat transfer coefficient using experimental fluid properties and experimental results in Figure 3.26. While the prediction results are not directly comparable to experiments, it shows that a correlation of this type could be used to more realistically approximate the heat transfer profiles behind Taylor bubbles. Unfortunately,

due to the progression of film cooling research from slot-type to patterned hole geometries, recent predictive work on this topic is sparse. Future studies (whether experimental, numerical, or theoretical) on the flow characteristics and heat transfer of plunging jets may be required.

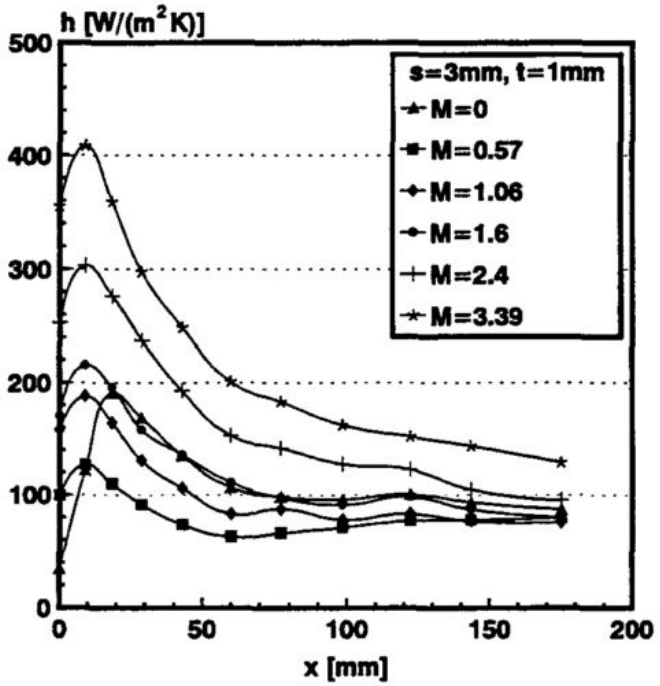

Figure 3.25: Heat transfer coefficient profiles for isothermal blowing $T_\infty = T_f = 270$°C for various blowing ratios from Bittlinger et al. [73] (used with permission). Here positive *x* indicates distance into the wake.

The heat transfer prediction within the film region is also of importance, despite its relatively small effect on the overall heat removal for the cases described in this work. As mentioned in the review, modelers have proposed either modified single-phase internal flow correlations or falling film correlations for calculation of the heat transfer coefficient. A comparison of the suggested correlations to experimental data is shown in Figure 3.27

for a bubble rising in laminar background flow. It can be seen that Colburn's correlation [68] for turbulent internal flow significantly over-predicts the heat transfer. Limitations of the experiment prevent measurement of the velocity profile within the film to determine if transition to turbulence occurs. In addition to Chun and Seban's [71] correlation for a turbulent falling film, their correlation for a laminar falling film,

$$h = 0.606\left(\frac{k_l^3 \rho_l^2 g}{\mu_l^2}\right)^{1/3}\left(\frac{\rho_l U_f \delta}{\mu_l}\right)^{-0.22} \tag{15}$$

was also included in the figure for two cases. In the first case, the prediction was made using a constant film thickness and film velocity based on measurements of the fully developed film. This instance is representative of many model formulations where the bubble is assumed to be a cylindrical plug rather than bullet-shaped. The actual film thickness profile and calculated local film velocity were substituted in the second case. It is evident that the film heat transfer coefficient is also over-predicted by the turbulent falling film correlation, but agreement is seen between experimental results and the laminar film predictions. Furthermore, the inclusion of the local film thickness and velocity improved the agreement by better capturing the shape of the experimental curve. While it is unclear whether the mechanisms assumed within the laminar film correlation are directly applicable to the Taylor bubble film (especially if the theory of Barbosa and Hewitt regarding annular and core regions is considered), the prediction capability is evident and may serve useful in future model development.

To conclude, it had been shown that particularly in the bubble wake, current slug flow models lack the ability to capture the magnitude and shape of the heat transfer coefficient profiles. Additional work will be required to apply slot film cooling mechanisms to the current results, but data from the field illustrates promise in that regard. Finally, it appears

that previously developed correlations for falling films may be directly applicable to modeling of the heat transfer coefficient for rising Taylor bubbles.

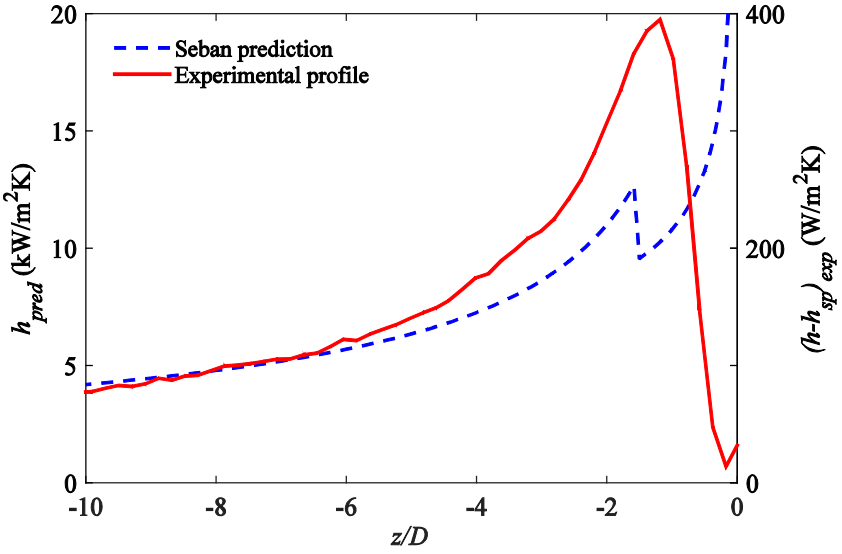

Figure 3.26: Comparison of predicted heat transfer coefficient by Seban [74] for slot injection film cooling to experimental results for Taylor bubble wake (experimental conditions: G=200 kg/m^{2}s, a/g=1, q''=1700 W/m^2, h_{SP}=192 W/m^{2}K).

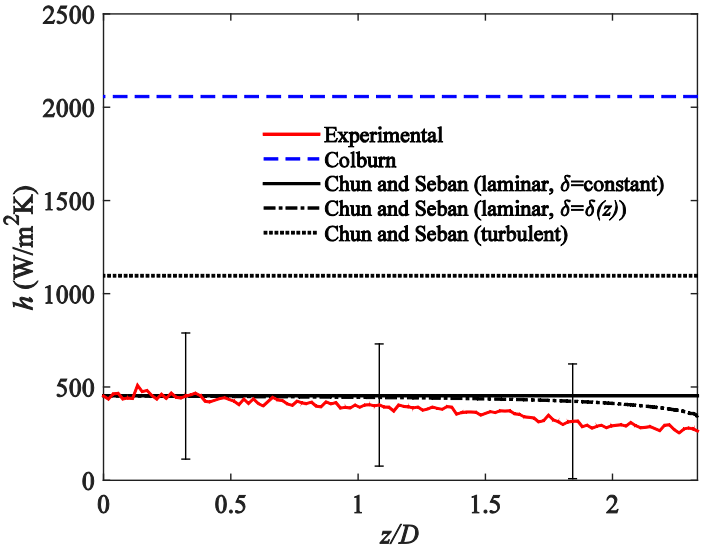

Figure 3.27: Comparison of experimentally measured film heat transfer coefficient the correlations of Colburn [68] and Chun & Seban [71]. The conditions were: $U_l = 37$ mm/s, $U_b = 142$ mm/s, $U_f = 851$ mm/s, $Re_l = 791$, and q'' = 1370 W/m^2.

CHAPTER 4: BUBBLE EFFECT ON NUCLEATE BOILING

The results presented in the previous chapter detailed the hydrodynamics and heat transfer associated with single elongated bubbles rising through a heated tube in which the initial condition was thermally-developing single-phase flow. While many applications exhibit these characteristics, some operating or emergency conditions in nuclear reactors result in nucleation at the wall. Bubbles nucleated near the bottom of the channel coalesce to form elongated bubbles and move upward, thereby affecting nucleation sites downstream. Using the same experimental setup described in Chapter 2, a preliminary study was completed on a single Taylor bubble rising through a tube where nucleation was present (see Figure 4.1). The conditions tested are summarized in Table 4.1. Power applied to the silicon tube was set such that nucleation was present over at least one half of the visible length to ensure data was collected over a sufficiently large area to be representative. Experiments were completed with three heat fluxes at each liquid mass flux to determine the influence of the bubble on increasingly vigorous nucleation. At elevated heat fluxes, the flow regime was observed to evolve significantly between the incipience of nucleation and the exit of the tube. Analyses for this study were isolated to the portion where nucleation was observed.

The heat transfer within the silicon tube as the bubble passed was measured by the same technique described in Chapter 2. Due to the significant increase in heat transfer coefficient resulting from nucleation, thermal losses from the tube were approximated to be negligible at the end caps (conduction) and 5% to the ambient (natural convection).

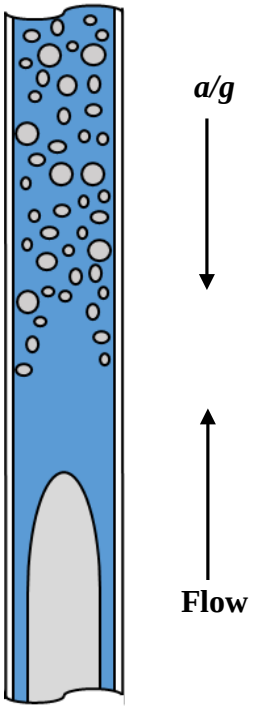

Figure 4.1: Schematic of initial conditions for single Taylor bubble influence on nucleate boiling tests.

Table 4.1: Summary of nucleate boiling test parameters.

G (kg/m^{2}s)	q'' (W/m^2)	T_{sub} (°C)
100	6630	2.7
	9520	2.8
	14160	2.9
185	9340	2.1
	13620	2.1
	18050	1.9

As with the single-phase tests, the heat transfer coefficient was plotted as a function of distance from the bubble tail (z/D>0: ahead of tail, z/D<0: behind tail). Figure 4.2 shows the heat transfer coefficient profiles for G=100 kg/m^{2}s and three heat fluxes. The measurements were left unscaled to emphasize the increase in overall heat transfer with

increasing heat flux. Unlike the results presented for the single-phase initial conditions in Chapter 3, the heat transfer coefficient was seen to decrease in the liquid film. This behavior can be explained if the ebullition model proposed by Hsu [75] is considered. He theorized that the activity of a wall nucleation site (growth of a vapor embryo) was limited by the growth of the thermal boundary layer, δ_t, near the heated wall. If a sufficiently thick δ_t is not present, the thermal conditions around the embryo would not be conducive to nucleation. In the case of a passing Taylor bubble in nucleate flow boiling, the acceleration of the liquid near the wall due to film formation caused the thermal boundary layer to thin such that nucleation could no longer occur. This behavior was observed near the nose for all heat fluxes tested, with the magnitude of degradation increasing with q''. It is well known that the frequency of bubble nucleation and subsequently the heat transfer coefficient is related to the superheat of the heated surface. In this case, suppression of nucleation in the film became progressively more detrimental to the heat transfer coefficient as the heat flux, wall superheat, and agitation due to bubble departure increased. This can be visually confirmed from heat transfer contour plots similar to those presented in earlier sections. In this case, however, the motion of the bubble through the tube is observed from the laboratory reference frame as shown in Figure 4.3. A strip of low, relatively uniform heat transfer coefficient indicates the film region where heat transfer degradation occurred. Ahead and behind the strip/bubble, nucleation sites are visible as dots of high heat transfer. It is evident that an increase in applied heat flux increases the nucleation frequency and site density.

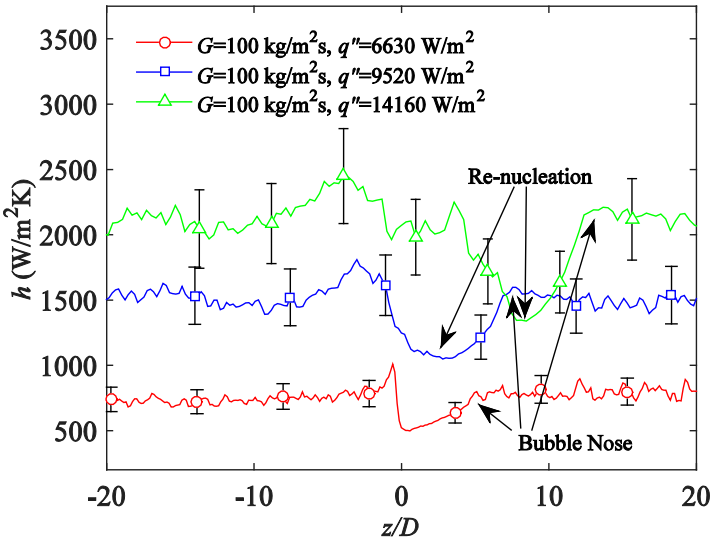

Figure 4.2: Heat transfer coefficient as a function of distance from the bubble tail as the bubble passes through nucleate boiling with G=100 kg/m^{2}s and q"=6630, 9520, and 14160 W/m^2.

The bubble length, and subsequently the distance ahead of the tail at which the heat transfer began to degrade, increased with heat flux due to higher evaporation rate of the bubbles as they passed through the silicon tube. As a consequence of the larger lengths and heat flux, re-nucleation within the liquid film was observed for the cases of q''=9520 and 14160 W/m^2, leading to an increase in heat transfer coefficient prior to the bubble tail. Visual evidence of this behavior is provided in Figure 4.4 where a representative IR image illustrates small cold spots on the tube inner wall during the passage of the bubble which are indicative of nucleation sites.

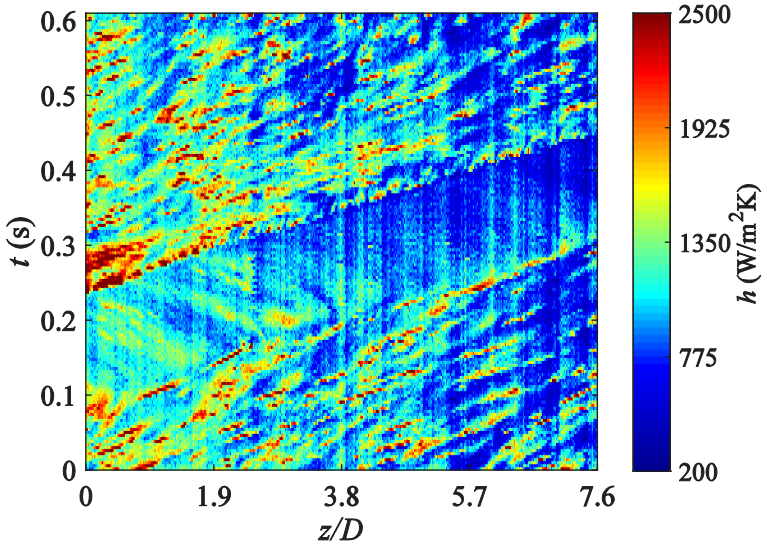

a) q''=6630 W/m^2

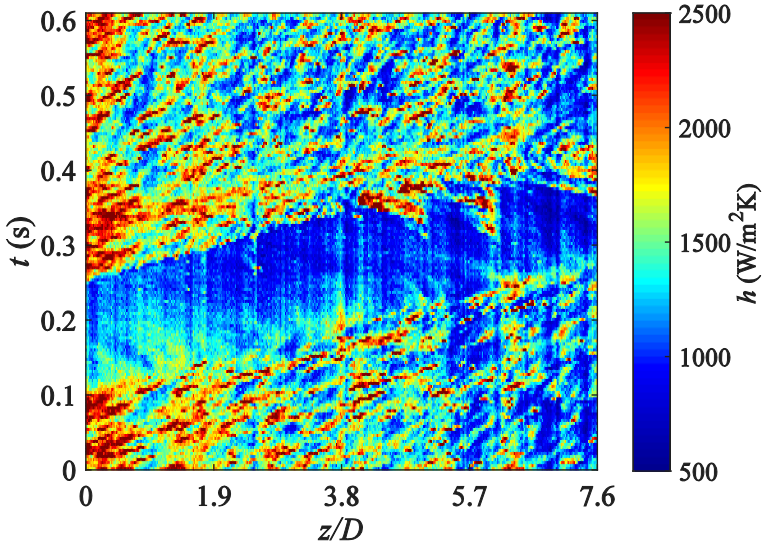

b) q''=9500 W/m^2

Figure 4.3: Wake heat transfer contours for G=100 kg/m2s and heat fluxes: a) q″=6630 W/m2 and b) q″=9500 W/m2.

The characteristics of suppression and re-nucleation observed in the liquid film are summarized in Figure 4.5 where process is divided into three zones (a, b, and c). In zone a, nucleate flow boiling is well established, resulting in steady heat transfer coefficient, wall temperatures, and thermal boundary layer thickness (δ_t). Formation of the film in zone

b accelerates the liquid and decreases δ_t such that the superheat conditions are not sufficient for bubble growth. As a result, a decrease in the heat transfer coefficient is coupled with an increase in the inner wall temperature. Eventually, in zone c, the additional superheating of the wall overcomes the thinner boundary layer thickness to re-establish nucleation. The inner wall temperature was observed to stabilize slightly above (about 5%) the steady value ahead of the bubble due to the additional superheat requirement for nucleation.

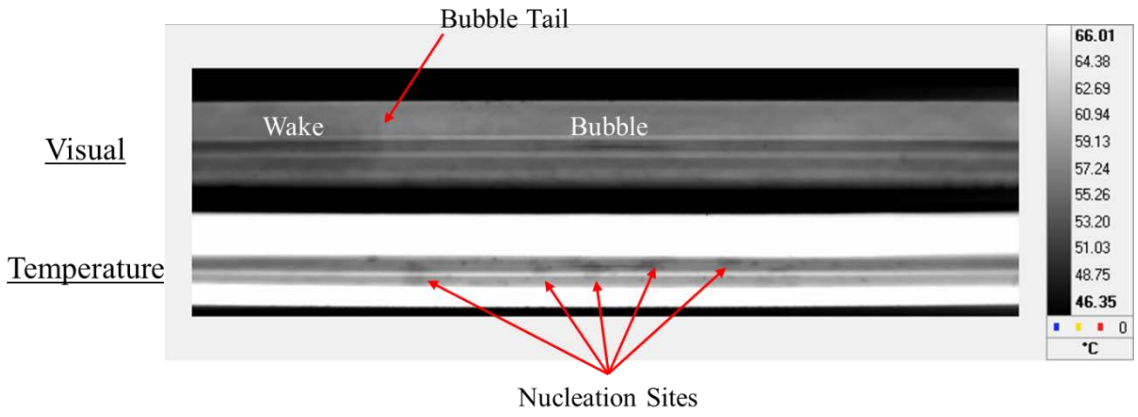

Figure 4.4: Representative IR image showing the passing of a Taylor bubble where nucleation is present in the liquid film. The testing conditions were G=100 kg/m^{2}s, q''=14160 W/m^2, T_{sub}=2.1 °C.

The wake heat transfer enhancement due to vortex shedding (see Figure 4.2) was found to be significantly smaller than was observed with the single-phase initial conditions. This result is unsurprising given that the agitation caused by wake turbulence is likely comparable to forced nucleate boiling. The high levels of mixing also contribute to the rapid decay of the wake enhancement. Due to the absorption of the silicon and polyimide tape, details of the wake hydrodynamics could not be more closely examined.

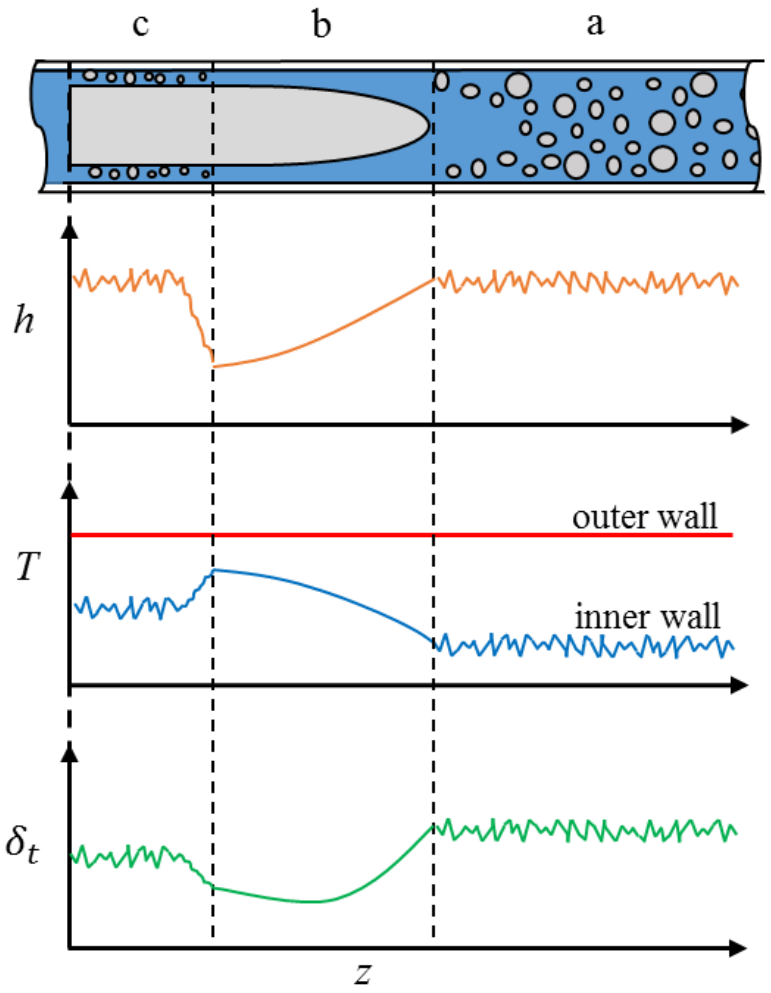

Figure 4.5: Schematic of Taylor bubble rising through nucleate boiling with representative graphs of the measured heat transfer coefficient, wall temperatures, and approximated thermal boundary layer.

Additional tests were completed at G=185 kg/m^{2}s to determine the effect of mass flux on the heat transfer profiles. As can be seen in Figure 4.6, degradation of the heat transfer coefficient is still observed within the film due to suppression of nucleation. Re-nucleation is seen for both q″=13620 and 18050 W/m^2. It can also be pointed out that the heat transfer coefficient ahead of the bubbles at q''=9340 and 13620 W/m^2 is smaller than are seen in Figure 4.2 for similar heat fluxes of q''=9520 and 14160 W/m^2. This can again be attributed

to a reduction of active nucleation sites caused by the thinner thermal boundary layer at a higher mass flux.

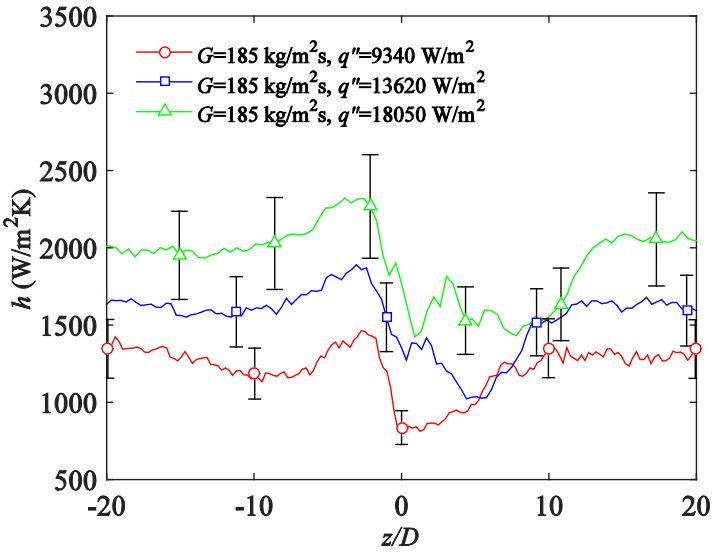

Figure 4.6: Heat transfer coefficient as a function of distance from the bubble tail as the bubble passes through nucleate boiling with G=185 kg/m^{2}s and q"=9340, 13620, and 18050 W/m^2.

While preliminary, the results of this study provide insight into the effect of long coalesced bubbles on nucleate flow boiling. It is evident that the presence of sequential bubbles or bubble trains would be highly detrimental to a thermal management system operating under these conditions. Continued work on this topic can provide not only invaluable information to heat transfer modeling efforts, but also potential solutions to prevent elongated bubble formation and/or maintain the stability of nucleation sites.

CHAPTER 5: CONCLUSIONS

The work presented in this dissertation is part of a broad effort by two-phase researchers to form accurate and reliable prediction methods for flow boiling heat transfer for earth- and space-based applications. To do so, previous research has indicated that two main topics are in need of further investigation: 1) development of flow boiling regime maps which account for fluid properties, heating conditions, surface properties, and gravity level; 2) identification of prominent heat transfer mechanisms for each regime to be applied to heat transfer modeling. The focus of this study was to address the second area with an emphasis on the characteristics of slug flow. Specifically, individual unit cells of slug flow (single bubbles) were investigated so that the initial and boundary conditions could be more easily specified and the effect of the rising bubble on a heated tube identified.

5.1 INTELLECTUAL CONTRIBUTIONS

5.1.1 Adaptation of Flow Boiling Experiment

The original UMD variable gravity flow boiling experiment was modified to increase its measurement capabilities and to create single elongated bubbles. The latter was accomplished by the addition of a bubble generation section consisting of two tubing segments connected downstream by a three way valve. One segment encased a wire heater used to vaporize liquid, creating a bubble of known volume. The second leg served as a bypass during bubble generation.

An adiabatic section was also added downstream of the heat transfer measurement section to allow for measurement of the film thickness and observation of the bubble dynamics. Several film thickness sensors were tested before the Keyence LK-G5000 model

was chosen, purchased, and installed. A compact, high-speed Sentech camera was also purchased and installed to capture flow visualization videos.

Finally, the experiment was prepared for variable gravity experiments aboard NASA's DC-9 aircraft. This process included verification of the experiment's structural requirements, completion of NASA safety documentation, and transport of the rig to Ellington Field in Texas. Successful flight testing was completed, the results of which have been presented in the previous chapters.

5.1.2 Characterization of Elongated Bubbles

A study on the hydrodynamics and heat transfer in the presence of an elongated bubble rising co-currently with vertical, upward flowing liquid was completed. Data collected in the laboratory and on an aircraft flying parabolic trajectories allowed for bubbles characterized by a wide range of Bond numbers to be observed. Visual analysis of the bubbles illustrated the effect of gravity, and subsequently drift velocity on the bubble profile. Bubbles exhibited small drift velocities and shapes characteristic of capillary flows at low gravity levels, while terrestrial and hypergravity conditions produced Taylor bubbles moving at higher drift velocities. The measured film thicknesses were shown to vary little with acceleration and be in agreement with correlations.

The flow dynamics induced by the different gravity levels was found to strongly influence the bubble shape and the local heat transfer characteristics. Large heat transfer enhancement was observed behind Taylor bubbles due to the presence of vortices in the wake. Capillary bubbles provided little wake heat transfer enhancement and only slight improvement in the liquid film. The frequency of vortex shedding for Taylor bubbles was shown to increase linearly with the plunging velocity, allowing for the proposal of a critical

impinging velocity to predict vortex incipience. Wall jet separation was found to affect the tube wall at differing penetration lengths depending on the acceleration and bubble drift velocity. Time-averaged heat transfer coefficient profiles showed that the variation in penetration length coincides with smaller and broader peaks in wake enhancement for a/g=1.8 compared to a/g=1.

Comparisons made with numerical simulations completed by Dr. Mirco Magnini at EPFL, Switzerland showed strong agreement in the bubble hydrodynamics as well as heat transfer characteristics. The local flow and temperature fields provided by the simulations enabled a better understanding of the vortex shedding process in the wake and its effect on the heat transfer coefficient.

The information gleaned from experiments and simulations were then applied to slug flow heat transfer models in the literature to determine their validity. It was found that the wake heat transfer coefficient was typically approximated using turbulent single-phase correlations. A more appropriate representation of the wake dynamics was proposed to be the slot film geometry, which produces similar heat transfer profiles to Taylor bubbles. Heat transfer within the film was shown to be reasonably predicted by laminar falling film correlations.

5.1.3 Taylor Bubble Effect on Nucleate Flow Boiling

A preliminary study was completed on the effect of a single Taylor bubble rising through a heated tube in which nucleate boiling had been established. Results showed that the acceleration of liquid into the bubble film thinned the thermal boundary layer and suppressed nucleation, leading to a decrease in heat transfer coefficient. The effect of suppression was more pronounced (larger degradation) at higher heat fluxes as more

nucleation sites were active prior to the bubble's arrival. In cases of long bubbles and high heat flux, the thermal boundary layer grew quickly within the film allowing for nucleation to be re-established.

5.2 RECOMMENDATIONS FOR FUTURE WORK

The results of this study, while providing valuable insight into the behavior and heat transfer around elongated bubbles, illustrate the complexity of slug flow and the need for further research in this area. Several directions could be taken to improve and advance upon the current work:

1. Given the insight provided by the presented experimental results and the overall goal of this study, a logical step in the progression of this work would be to develop a model for a single Taylor bubble rising in co-current flow through a heated tube. General considerations for heat transfer in the wake region were discussed in Section 3.4, where treatment of the plunging jet as a wall jet was suggested. It was also shown that the film heat transfer could be reasonably approximated using correlations for a falling film. A successful model for single Taylor bubbles can then be expanded to bubble trains, which are of more practical interest.
2. Improvements to the current experiment could provide a more detailed and complete data set allowing for the resolution of several outstanding questions. Replacement of the silicon tube with a sapphire tube of the same size would allow for simultaneous heat transfer measurements, flow visualization, and film thickness measurements to be made within the heated section. This would improve greatly the characterization of the tail motion effect on wake heat transfer as well as the variation in film thickness due to

evaporation. An additional, and more complicated, modification would be the addition of particle image velocitmetry (PIV) or particle shadow velocimetry (PSV). Tracking of particles in the bubble wake would provide local, time-resolved visualization of the wake flow patterns dictating heat transfer at the wall.

3. As the flow field and heat transfer around single elongated bubbles has been relatively well studied, the current (and potentially improved) experiment could be applied to investigate the effect of sequential bubbles and bubble trains on the local heat transfer. Some work on sequential bubbles is currently being completed by the group of Shemer and Barnea at Tel-Aviv University [76], but the combination of local heat transfer measurements and flow visualization is lacking. A numerical investigation by Magnini et al. [42] showed that for two bubbles flowing through a microchannel, the second bubble caused larger heat transfer enhancement than the first. This was attributed to the overlap of the hydrodynamic effects on wall temperature. It is expected that similar findings would be obtained for Taylor bubbles in larger channels.
4. The preliminary study on Taylor bubbles rising through a heated tube where nucleate boiling is present illustrated that, unlike previous tests with single-phase flow, the bubble hydrodynamics were detrimental to heat transfer due to suppression of nucleation. Using an improved sapphire test section where nucleation sites can be more easily observed, the fundamentals of this behavior can be closely investigated.
5. A more practical line of work may also be grown out of the early nucleation findings. If this type of flow (nucleation with passing large bubbles) were to occur in an application where heat transfer maximization were desired, it would be advantageous to either break up the large bubbles or to ensure that nucleation sites remained active

even in the presence of the bubble. A solution to the latter could be modification of the surface roughness of the tube wall such that a thinner boundary layer would be required for nucleation. This may have the additional effect of promoting the incipience of boiling at a lower superheat, which is advantageous from a heat transfer perspective. A study on surface modification of flow boiling channels could investigate these propositions.

APPENDIX A: CALIBRATIONS AND UNCERTAINTY

A.1 UNCERTAINTY OVERVIEW

The uncertainty analyses of this experiment were based on the practices laid out in Beckwith et al. [77] and Taylor [56]. The overall uncertainty of a measurement can be broken into two components: the bias uncertainty and random uncertainty, as shown in Figure A.1. Bias uncertainty defines the possible measurement error as an offset with respect to the actual value, while random uncertainty describes possible error in the measurement due to randomness in a signal or repeated measurements. Each of these uncertainty types can be calculated separately and then combined, as will be shown below.

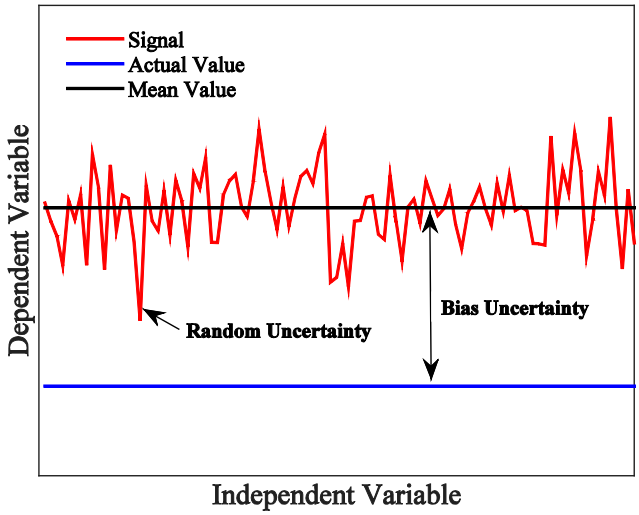

Figure A.1: Description of measurement uncertainty categories.

A.1.1 Bias Uncertainty

The bias uncertainty for measurements obtained during this study, particularly heat flux and heat transfer coefficients, were determined on a case-by-case basis as the calculation procedures vary. These analyses will be described individually in the sections that follow. One common method in all cases is accounting for propagation of error due to secondary or tertiary measurements used in the primary measurement calculation. For example, a measured value y is dependent on properties $x_1, x_2, \ldots, x_n$. The uncertainty of y, δy, is calculated by the equation,

$$\delta y = \sqrt{\left(\frac{\partial y}{x_1}\delta x_1\right)^2 + \left(\frac{\partial y}{x_2}\delta x_2\right)^2 + \cdots + \left(\frac{\partial y}{x_n}\delta x_n\right)^2} \tag{16}$$

where, $\delta x_1, \delta x_2, \ldots, \delta x_n$ are the uncertainties of properties $x_1, x_2, \ldots, x_n$. This equation may also be applied when combining the bias and random uncertainties to obtain the overall uncertainty of a measurement.

A.1.2 Random Uncertainty

Random uncertainty of calculations, calibrations, or transducer measurements was determined using the Student's t-distribution method, where the distribution of a quantity *t* is defined by,

$$t = \frac{\bar{x} - \mu}{S_x/\sqrt{N}} \tag{17}$$

Here, $\bar{x}$ is the mean value for a sample, μ is the mean value for a population, S_x is the standard deviation of a sample, and N is the number of samples. The values for *t* are widely available in tabulated form and are dependent on the number of degrees of freedom ($v = n - 1$) and the desired confidence, c. For all uncertainty calculations presented, the confidence was chosen to be 90%. The random uncertainty is defined by the quantity $\bar{x} -$

$\mu = \frac{tS_x}{\sqrt{N}}$, which represents the deviation of the sample mean from the population mean caused by relatively few measurements.

A.1.3 Curve Fitting Uncertainty

A final category of uncertainty calculation is the potential error induced by fitting a linear curve to acquired data, as was the case for calibrations described below. A method presented by Taylor [56] was utilized to predict the induced slope (*B*) and offset (*A*) uncertainty,

$$\delta_A = \sigma_y \sqrt{\frac{\sum x^2}{N\sum x^2 - (\sum x)^2}} \tag{18}$$

$$\delta_B = \sigma_y \sqrt{\frac{N}{N\sum x^2 - (\sum x)^2}} \tag{19}$$

where *x* is the independent variable, *y* is the dependent variable, and *N* is the number of samples. The parameter σ_y is an error estimation of the collected data with respect to the fitted line and is defined as,

$$\sigma_y = \sqrt{\frac{1}{N-2}\sum_{i=1}^{N}(y_i - A - Bx_i)^2} \tag{20}$$

A.2 INDIVIDUAL MEASUREMENT ANALYSES

A.2.1 Temperature

Proper measurement of temperature is essential in heat transfer experiments to reduce the uncertainty of results and to ensure that the desired testing conditions are obtained. This experiment utilizes T-type thermocouples and an Electrophysics 660M infrared camera to measure the various temperatures in the system. Thermocouples were calibrated by immersion in a controlled water bath, with the reference temperature measured using a

NIST traceable mercury thermometer accurate to 0.1°C. The most important thermocouple measurements for experiments were the temperature at the test section inlet (T_{in}) and the temperature at the preheater inlet ($T_{PH,in}$); for optical property measurements and camera calibration the most important were the temperature of the blackbody (T_{bb}) and the ambient temperature within the containment chamber (T_{box}). During thermocouple calibration, nine measurements were taken and compared to the reference thermometer as shown in Figure A.2a. Linear fits were computed for each thermocouple to obtain a calibration curve, which was used in data processing. The uncertainties of the thermocouples were calculated and include the error associated with the linear fit as well as the uncertainty of the mercury thermometer. A summary of the uncertainties can be found in Table A.1.

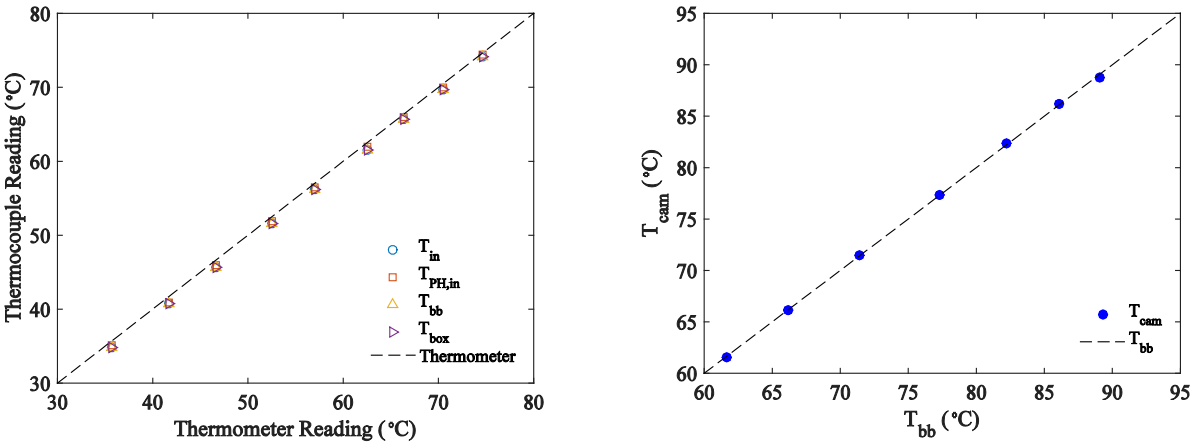

a) b)

Figure A.2: Calibration curves for a) experiment and calibration thermocouples, b) infrared camera.

A similar calibration procedure was conducted for the infrared camera. A blackbody (described in Kim et al. [47]) was heated and the opening observed by the camera. The measured camera temperatures were plotted against the measured blackbody temperature

as shown in Figure A.2b. The uncertainty of the camera measurement was found to be 0.14°C and included the uncertainties of the calibration curve and blackbody temperature.

Table A.1: Summary of important temperature uncertainties.

Temperature	Uncertainty (°C)	Typical Value (°C)
T_{in}	0.13	58
$T_{PH,in}$	0.12	34
T_{bb}	0.12	30-90
T_{box}	0.39	25
T_{cam}	0.14	50-70

A.2.2 Flow

The flowmeter used in this experiment, an Omega FLR1009, was calibrated by flowing water at constant rates through the flowmeter and collecting samples in a graduated cylinder over a specified duration. The graduated cylinder had a capacity of 100 mL and graduations of 1 mL. A stopwatch with a readout to 0.1s was used to record the time. Figure A.3 illustrates the measured flow rates as a function of output voltage. A linear curve was fit to the data to create a calibration curve used in the LabVIEW^{TM} VI and post-processing. The uncertainty in determining the flow rate with the calibration curve was found to be 1.3 mL/min (typical value 50-250 mL/min).

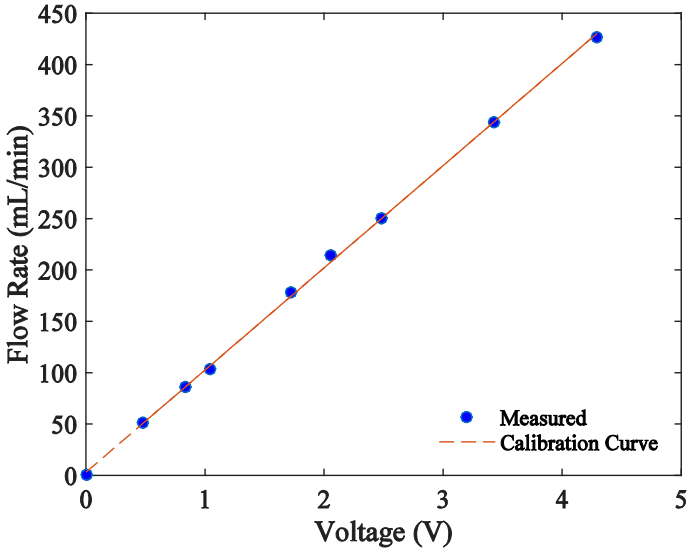

Figure A.3: Calibration data and curve for FLR1009 flowmeter.

Of greater use in experimental analysis, however, is the liquid mass flux, rather than the flow rate. The mass flux can be determined from the flow rate with knowledge of the liquid density (ρ_l) and tube area (A_t) by equation (21), where the flow rate (Q) is now in the units of m^3/s.

$$G = \frac{Q\rho_l}{A_t} \tag{21}$$

The uncertainty of the mass flux is therefore dependent on the uncertainty of the flow rate, the liquid density, and the radius of the tube. As was discussed above, the flow rate is known to within 1.3 mL/min (2.23×10^{-8} m^3/s). The uncertainty in HFE 7100 density will be determined in later sections, but was found to be 0.45 kg/m^3. Finally, the tube radius was measured using precision calipers to within 0.01 mm. Using the propagation of uncertainties method, the overall mass flux uncertainty was found to be 3.95 kg/m^3s (typical value of 50-200 kg/m^2s).

A.2.3 Pressure

The absolute pressure at the inlet of the heated silicon test section was measured using an Omega PX209-030A5V transducer with a range of 0-30 psia. The factory calibration (NIST traceable) was used as a baseline, but checks were completed using a custom manometer built in the laboratory. Figure A.4 shows the applied absolute pressure as a function of transducer output voltage. The calculated uncertainty of the calibration curve was found to be 0.01 psi.

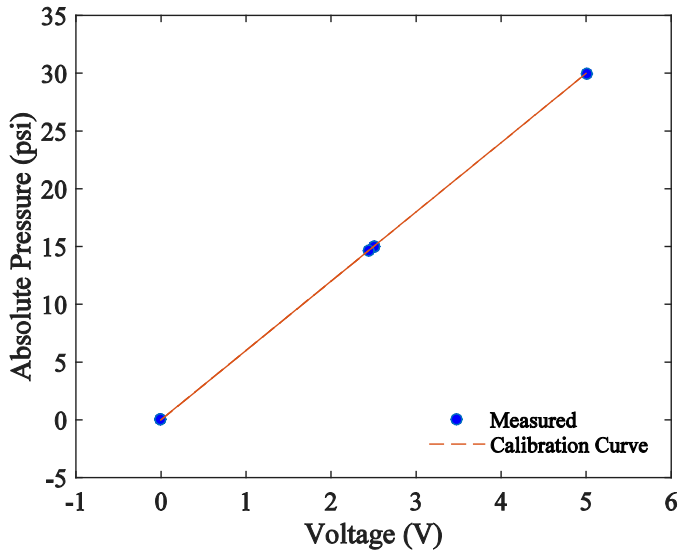

Figure A.4: Absolute pressure transducer calibration.

A.2.4 Fluid Properties

Properties for liquid and vapor HFE 7100 were determined using curve fits to data provided by 3M (the manufacturer of HFE 7100). The absolute pressure at the test section inlet was used as the independent variable for property determination during testing and data analysis of saturated conditions. Local temperature, measured with T-type thermocouples, was used as the independent variable for single-phase property calculations. Uncertainties of the fluid properties were calculated by accounting for the error associated with the curve fit to

the data provided by 3M as well as the uncertainty in measurement of the independent variable. A summary of the major uncertainties is given in Table A.2.

Table A.2: Summary of fluid property uncertainties.

Property	**Uncertainty**	**Typical Value**
T_{sat} [ºC]	0.14	60
ρ_l [kg/m^3]	0.45	1390
h_{lv} [MJ/kg]	0.97	112
μ_l [cP]	0.001	0.375

A.2.5 Film Thickness

The film thickness sensor (Keyence LK-G5000) utilizes a triangulation method of measurement as illustrated in Figure A.5. Laser light exits the sensor head at a specified angle and is reflected from the inner and outer walls of the tube and from the bubble liquid/vapor interface. Depending on the indices of refraction and thicknesses of the various layers, the reflected beams will intercept the sensor measurement array at different locations. The location at which the light reflects from the liquid/vapor interface is dependent on the film thickness as well as the inclination of the interface.

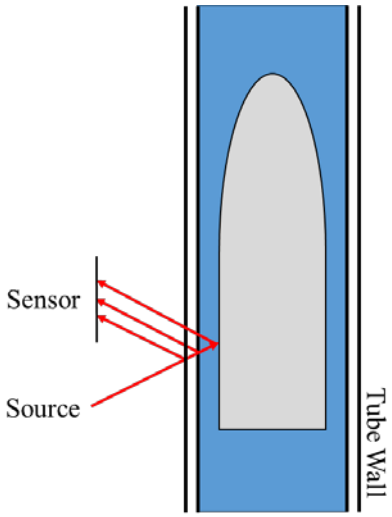

Figure A.5: Schematic of triangulation technique used by film thickness sensor.

Assuming that the liquid film is smooth and the film thickness is not changing (the liquid/vapor interface is parallel to the tube wall), the multilayer can be approximated using flat plates to simplify the setup for calibration (Figure A.6).

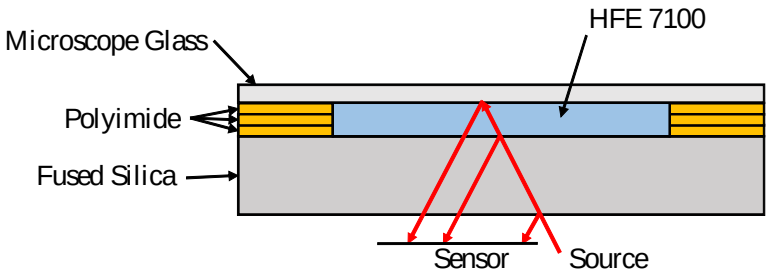

Figure A.6: Schematic of parallel calibration setup.

A fused silica wafer with a thickness of 1.03 mm and index of refraction of 1.456 was used to simulate the Pyrex tube of 1.00 mm thickness and index of refraction of 1.474. Polyimide strips of known thickness (48±1 μm and 24±1 μm) were used as spacers between the silica wafer and a microscope cover class that simulated the bubble interface. The gap

created by the spacers was filled with HFE 7100 to replicate the bubble liquid film. The known film thickness as a function of the sensor readout was obtained over the range of film thicknesses measured in our tests and a linear fit to the data was obtained as shown in Figure A.7a. Under these conditions, the thickness could be measured to a minimum accuracy of 16 µm.

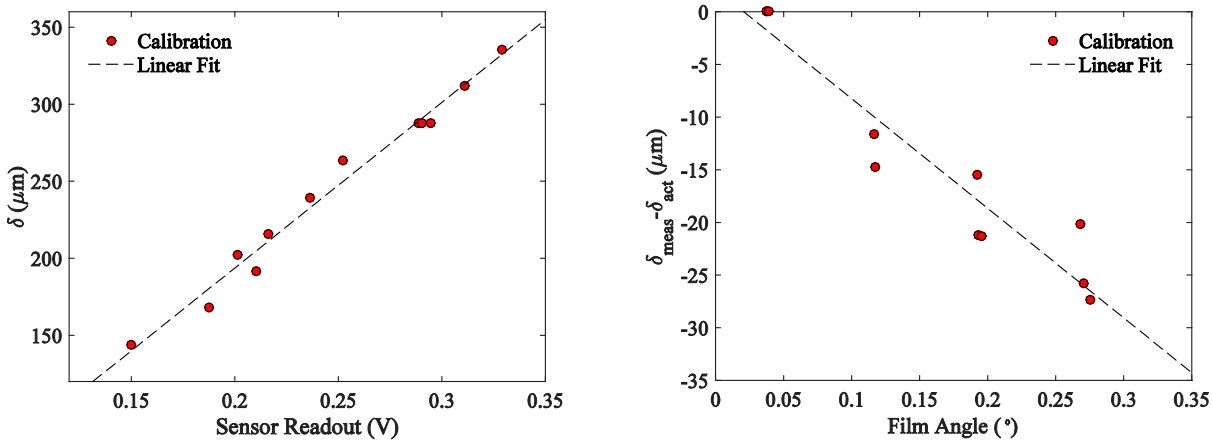

a) b)

Figure A.7: Calibration curve for Keyence film thickness sensor: a) flat configuration and b) angled configuration.

Shorter bubbles possessed developing liquid films which were not parallel to the tube wall. Characterizing the uncertainty associated with this angled film was completed in a similar manner to the original calibration. The polyimide films were unevenly stacked such that the microscope glass was inclined relative to the silica wafer as shown in Figure A.8.

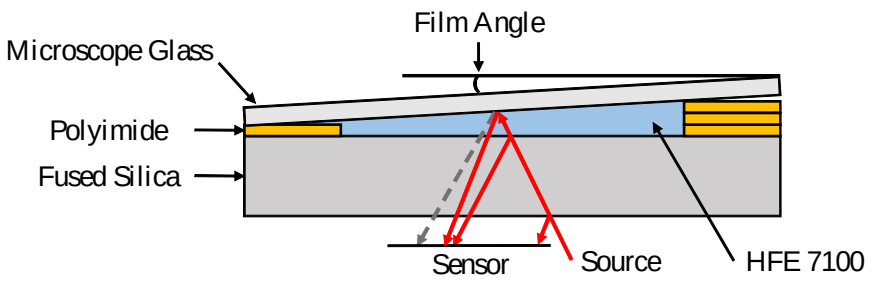

Figure A.8: Schematic of angled calibration setup.

Measurements were obtained at various inclination angles up to 0.27° (maximum bubble film angle measured was 0.26°) and the error relative to the actual film height was calculated. The error in measured thickness increased with increasing film angle as shown in Figure A.7b as expected. The maximum uncertainty for film thickness with the added correction required for the non-parallel liquid/vapor interfaces was 17 µm.

During parabolic flight testing, settling of the experiment due to gravity variations yielded the Keyence sensor inoperable. Film thickness measurements were instead made using detailed image analysis of the high-speed video. In order to correct for optical distortion caused by the curvature of the glass tube, a calibration was completed in which a grid with 0.5 mm spacing was inserted into the tube and submerged in liquid HFE 7100 as shown in Figure A.9a. The radial distance from the tube centerline from which each grid line was observed was correlated to the known grid spacing to create a calibration curve shown in Figure A.9b. Estimating the uncertainty for this technique includes several components and assumptions. First, the grid spacing is assumed to be accurate (it was printed using a 600 dpi laser printer and was checked using a ruler before insertion into the tube). Second, the potential error in determining the center each grid line was assumed to

be ±1 pixel (±37 µm), yielding an uncertainty of $\frac{37}{2} = 19$ µm. This value was included with the calculated uncertainty of linear curve fitting to obtain a total uncertainty of 25 µm.

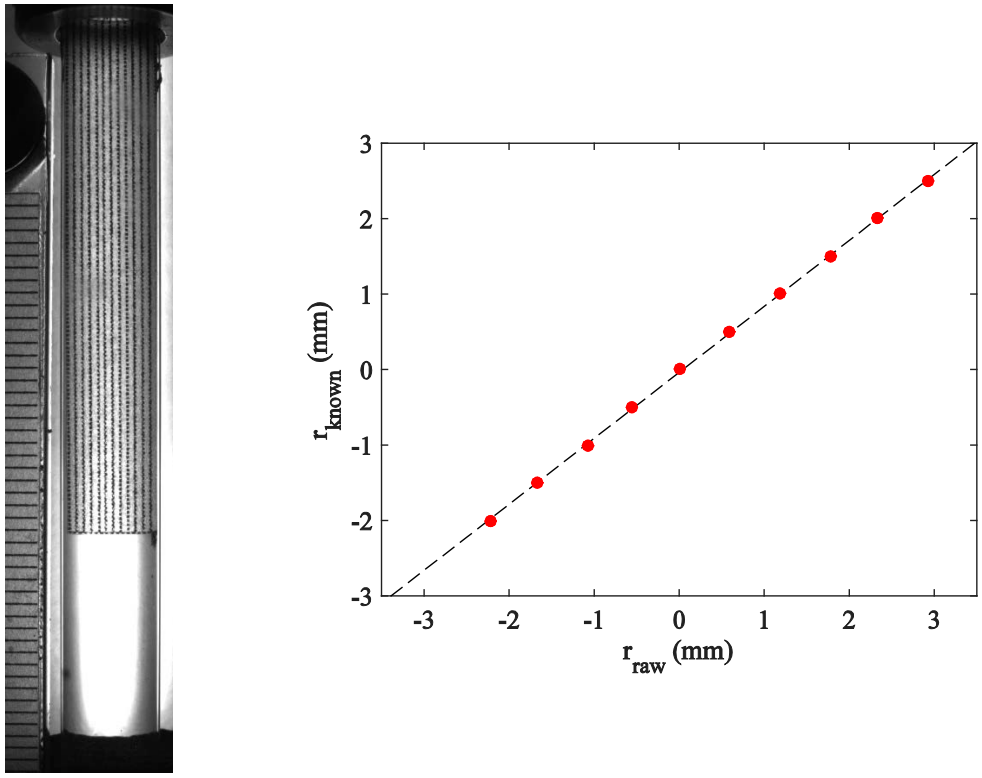

a) b)

Figure A.9: Calibration of visual film thickness measurements: a) 0.5 mm grid inserted in tube and submerged with HFE 7100, b) calibration curve relating raw radial position to known grid distances.

Film thickness measurements using the two methods were compared to ensure consistency and provide a means of validation. Bubbles rising in liquid with drift velocities over the range $105 \leq U_d \leq 163$ mm/s were measured by both techniques. The film thickness at the bubble tail was plotted as a function of bubble length in Figure A.10. Measurement types are seen to agree with each other as well as with correlations by Brown [19] and Llewellin et al. [26] for fully developed films.

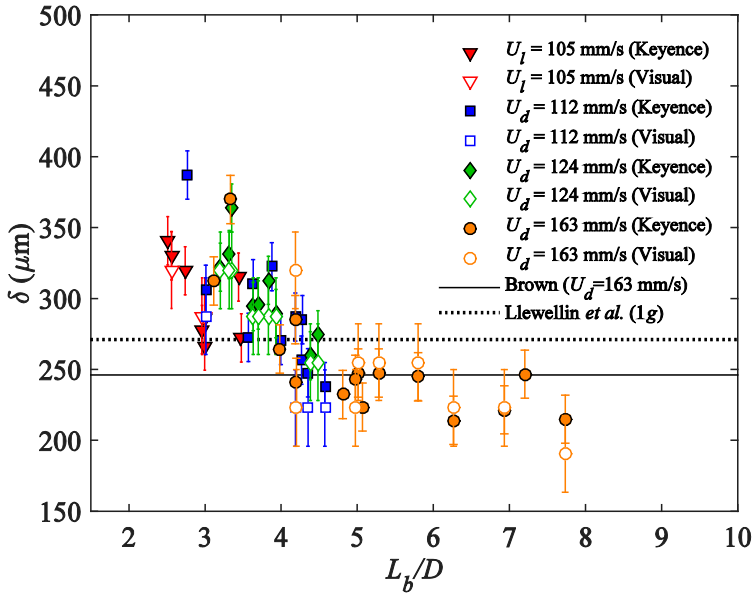

Figure A.10: Comparison of film thicknesses measured by a Keyence laser displacement sensor and analysis of high-speed visual images.

A.2.6 Optical Properties

The infrared technique utilized in this study for heat transfer measurements was dependent on knowledge of the optical properties of the materials constructing the tube multilayer: the silicon tube, Polyimide tape, and black paint. A rigorous series of experiments was conducted to obtain the absorptivity, reflectivity, and emissivity of the multilayer components according to the procedure described in Kim et al. [47], which is summarized below.

The silicon tube wall and Polyimide tape were considered to be plane walls for the infrared technique's optical model as the width of the camera's pixel (0.11 mm) is significantly smaller than the diameter of the tube (6 mm). Using this assumption, ray-

tracing of radiation incident on a single plane wall yields equations for the apparent reflectivity (eqn. (22)) and apparent transmissivity (eqn. (23)) of the wall,

$$\rho_{app,m-\infty} = \rho_{m-\infty} + \frac{(1-\rho_{m-\infty})^2 \rho_{m-\infty} {\tau_m}^2}{1-{\rho_{m-\infty}}^2 {\tau_m}^2} \tag{22}$$

$$\tau_{app,m-\infty} = \frac{(1-\rho_{m-\infty})^2 \tau_m}{1-{\rho_{m-\infty}}^2 {\tau_m}^2} \tag{23}$$

where τ_m and $\rho_{m-\infty}$ are the transmissivity of the reflectivity of the wall, respectively. In order to extract the two absolute properties from these equations, two experiments are required to determine the apparent properties and then the equations may be solved simultaneously. The experimental setups are shown below in Figure A.11.

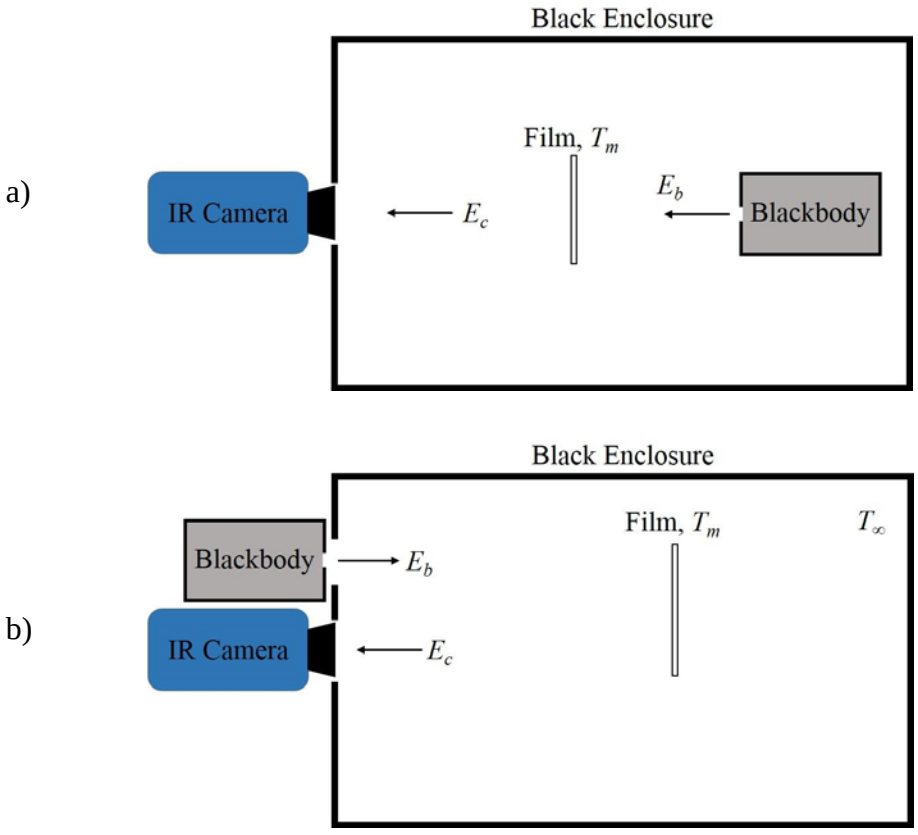

Figure A.11: Experimental setup for multi-layer optical property determination: a) apparent transmissivity measurement, b) apparent reflectivity measurement.

The energy received by the camera is a sum of the various sources, namely, the blackbody, emission of the film, and emission of the ambient surroundings. Equations for the energy balances are given below for the apparent transmission test with/without the blackbody (Figure A.11a), and for the apparent reflection test with/without the blackbody (Figure A.11b), respectively:

Transmission:

$$E_{t,1} = \tau_{app,m\infty}\left(F_{\lambda_1-\lambda_2}\sigma {T_b}^4\right) + \varepsilon_{app,m-\infty}\left(F_{\lambda_1-\lambda_2}\sigma {T_m}^4\right) + \rho_{app,m-\infty}\left(F_{\lambda_1-\lambda_2}\sigma {T_\infty}^4\right) \tag{24}$$

$$E_{t,2} = \tau_{app,m-\infty}\left(F_{\lambda_1-\lambda_2}\sigma {T_\infty}^4\right) + \varepsilon_{app,m-\infty}\left(F_{\lambda_1-\lambda_2}\sigma {T_m}^4\right) + \rho_{app,m-\infty}\left(F_{\lambda_1-\lambda_2}\sigma {T_\infty}^4\right) \tag{25}$$

Reflection:

$$E_{r,1} = \tau_{app,m-\infty}\left(F_{\lambda_1-\lambda_2}\sigma {T_\infty}^4\right) + \varepsilon_{app,m-\infty}\left(F_{\lambda_1-\lambda_2}\sigma {T_m}^4\right) + \rho_{app,m-\infty}\left(F_{\lambda_1-\lambda_2}\sigma {T_b}^4\right) \tag{26}$$

$$E_{r,2} = \tau_{app,m\infty} - \left(F_{\lambda_1-\lambda_2}\sigma {T_\infty}^4\right) + \varepsilon_{app,m-\infty}\left(F_{\lambda_1-\lambda_2}\sigma {T_m}^4\right) + \rho_{app,m-\infty}\left(F_{\lambda_1-\lambda_2}\sigma {T_\infty}^4\right) \tag{27}$$

where $\varepsilon_{app,m-\infty}$ is the apparent emission of the film/substrate and $F_{\lambda_1-\lambda_2}$ is the fractional function defining the portion of Planck's function absorbed by the camera. Subtraction of eqn. (25) from eqn. (24) and eqn. (27) from eqn. (26) yields simplified relations for the apparent transmission and reflection of the film/substrate, which were used to simultaneously solve eqns. (22) and (23) for the actual transmissivity and reflectivity.

$$\tau_{app,m-\infty} = \frac{E_{t,1} - E_{t,2}}{\sigma\left(F_{\lambda_1-\lambda_2}{T_b}^4 - F_{\lambda_1-\lambda_2}{T_\infty}^4\right)} = \frac{\sigma\left(F_{\lambda_1-\lambda_2}{T_{t,1}}^4 - F_{\lambda_1-\lambda_2}{T_{t,2}}^4\right)}{\sigma\left(F_{\lambda_1-\lambda_2}{T_b}^4 - F_{\lambda_1-\lambda_2}{T_\infty}^4\right)} \quad (28)$$

$$\rho_{app,m-\infty} = \frac{E_{r,1} - E_{r,2}}{\sigma\left(F_{\lambda_1-\lambda_2}{T_b}^4 - F_{\lambda_1-\lambda_2}{T_\infty}^4\right)} = \frac{\sigma\left(F_{\lambda_1-\lambda_2}{T_{r,1}}^4 - F_{\lambda_1-\lambda_2}{T_{r,2}}^4\right)}{\sigma\left(F_{\lambda_1-\lambda_2}{T_b}^4 - F_{\lambda_1-\lambda_2}{T_\infty}^4\right)} \quad (29)$$

Uncertainties of the transmissivity and reflectivity of the polyimide tape and silicon tube were estimated by performing a perturbation analysis on the property determination procedure. This method entailed varying each of the inputs to determine their relative impact on the overall uncertainty. The major contributors were found to be temperatures measured by the camera and thermocouples, with uncertainties of 0.14ºC and 0.12ºC, respectively. Combining the influences of each input yielded the uncertainties summarized in Table A.3. The transmissivity of both silicon and polyimide tape was converted to the form of absorption coefficient (defined as $\alpha = -\frac{\ln(\tau_m)}{d}$, where d is the sample thickness) to be applied in heat transfer calculations. By doing so, the uncertainty in thickness of the samples tested was introduced. Scanning electron microscope (SEM) images were used to obtain high-resolution thickness measurements of the polyimide tape, while a dial micrometer was used for the silicon tube. Uncertainties in thickness of the polyimide tape and silicon tube were found to be 0.32 μm and 10 μm, respectively. Values of absorption coefficient are also included in Table A.3.

Table A.3: Uncertainties associated with optical property determination.

Parameter	Uncertainty	Typical Value
τ_{Si} [-]	0.0064	0.9
τ_{p} [-]	0.0072	0.74
ρ_{Si} [-]	0.0026	0.3
ρ_{p} [-]	0.0019	0.044
α_{Si} [m^{-1}]	6.5	103
α_{p} [m^{-1}]	167	5277

A.2.7 Effective T_∞ Calibration and Uncertainty

As described in Chapter 2, an in-situ calibration was completed during testing to determine an effective T_∞ to be used in the heat flux calculations. This calibration removed the effect of reflections within the tube, variation in optical properties due to thermal gradients within the multilayer, and non-uniformity in the surrounding temperature due to heating of the camera housing. The tube wall temperatures were measured as single-phase liquid flowed through the silicon tube, which was heated with a constant power input. In order to calibrate the effective surroundings temperature, knowledge of the heat transferred into the fluid was required. Losses from the tube included natural convection to the surroundings and conduction into the connections at each end, each of which was estimated using the outer tube wall temperature profile (an example is shown in Figure A.12). Conduction losses were approximated by measuring the thermal gradient at the outlet of the silicon tube. The temperature gradient at the inlet was not used for these calculations as the profile was dominated by thermal entry region effects. Instead, the inlet losses were assumed to be the same as the outlet given that the O-ring connections were identical. Including both ends, conduction losses were approximated to be $Q_{loss,caps} = 23\pm3\%$.

Losses to the surroundings by natural convection were estimated using a correlation by Churchill and Chu [49] for free convection from a vertical wall,

$$\overline{Nu}_y = 0.68 + 0.515 Ra_y^{1/4} \tag{30}$$

where $\overline{Nu}_y$ is the wall-averaged Nusselt number and Ra_y is the wall averaged Rayleigh number (based on the average wall temperature - calculated from the profile). Loss to the surroundings was approximated to be $Q_{loss,conv} = 9\pm1\%$. Together, the total power loss from the tube was $Q_{loss,IR} = 32\pm4\%$, which compare well with the fluid energy balance calculation of $Q_{loss,TC} = 35\pm12\%$.

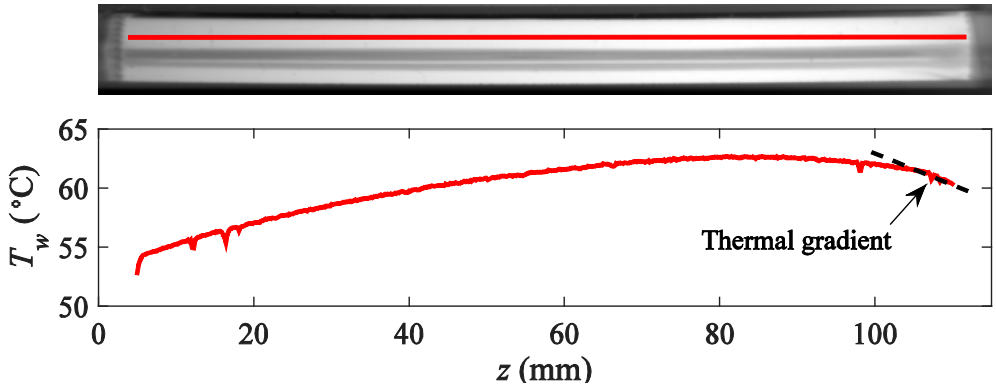

Figure A.12: Representative wall temperature profile showing thermal gradients at tube connections.

The net power entering the fluid was converted to heat flux using the geometric parameters of the tube and applied as an input to calculate the effective T_∞ from the data reduction MATLAB scripts. The uncertainty in the surroundings temperature was estimated to be ±0.2°C (±1%), accounting for potential error in the heat loss calculations.

A.2.8 Heat Transfer

The heat flux and heat transfer coefficient procedure outlined in Chapter 2 was carried out within a MATLAB script due to the complexity and breadth of the calculations. Uncertainty of these measurements was approximated using a perturbation analysis in which inputs to the calculations were perturbed slightly from the assumed value to determine the impact of each input's uncertainty on the overall uncertainty. The heat flux calculation was a function of several parameters related to the IR temperature measurement and the coupled optical/inverse conduction problem,

$$q" = f(T_{ci}, T_{co}, k_{Si}, k_p, k_{ad}, d_{Si}, d_p, d_{ad}, \rho_{Si-\infty}, \rho_{Si-p}, \alpha_{Si}, \alpha_p, \varepsilon_p, T_\infty)$$

where T_{ci} and T_{co} are the inner and outer wall temperatures measured by the IR camera; k_{Si}, k_p, and k_{ad} are the thermal conductivities of the silicon, polyimide, and adhesive; d_{Si}, d_p, and d_{ad} are the thicknesses of the silicon, polyimide, and adhesive layers; $\rho_{Si-\infty}$ and ρ_{Si-p} are the reflectivities of silicon to air and silicon to polyimide; α_{Si} and α_p are the absorption coefficients for silicon and polyimide; ε_p is the emissivity of the black paint; T_∞ is the effective temperature of the surroundings based on calibrations. A representative data set was selected and each input was independently varied by ±10% and ±20% to create a curve from which the slope $\left(\frac{\delta q"}{\delta ()}\right)$ could be calculated at the assumed value. The slopes were then used to calculate the overall bias uncertainty via the propagation of error method (see eqn. (16)) with the corresponding input uncertainties. Major contributors to the bias uncertainty were found to be T_{ci}, $\rho_{Si-\infty}$, ρ_{Si-p}, α_{Si}, and α_p. This procedure was repeated for six values of measured heat flux to determine if the uncertainty is a function of the

measurement itself. Figure A.13 illustrates that the bias heat flux uncertainty varies little over the range of heat fluxes tested, with percentages ranging from 110% at $q" = 0.2$ kW/m^2 down to 20% at $q" = 11.7$ kW/m^2.

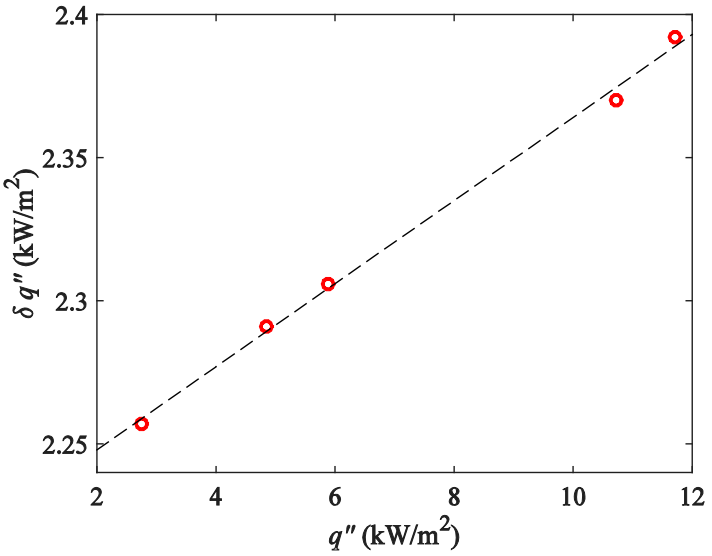

Figure A.13: Bias uncertainty in heat flux as a function of measured heat flux.

Estimation of the bias uncertainty in heat transfer coefficient was completed using a procedure similar to that used for the heat flux. Specifically, the local heat transfer coefficient was defined as

$$h = \frac{q"}{(T_{s,i} - T_m)} \tag{31}$$

where $q"$ and $T_{s,i}$ are calculated from the MATLAB script. As before, a perturbation analysis was completed to determine the relative impact of the various input parameters at several values of the heat transfer coefficient. Final values of heat transfer coefficient bias uncertainty are plotted in Figure A.14 as a function of heat transfer coefficient and include

contributions of q'', $T_{s,i}$, and T_m. The bias uncertainty was found to increase significantly with increasing heat transfer coefficient from 302 at h=266 W/m^{2}K (113%) to 733 at h=2315 W/m^{2}K (32%). These large uncertainties were partially negated in the presentation of results by offsetting h with h_{SP}, as described in the IR technique description.

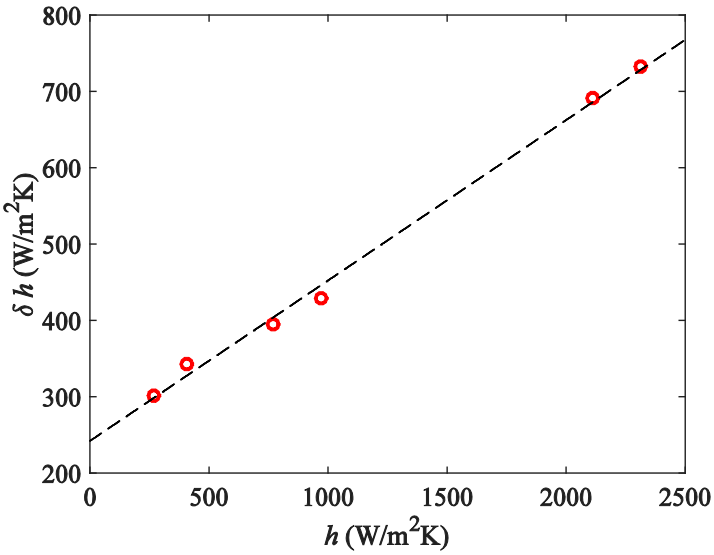

Figure A.14: Bias uncertainty in heat transfer coefficient as a function of measured heat transfer coefficient.

APPENDIX B: FILM VELOCITY DERIVATION

In order to determine the velocity of the liquid film moving toward the rear of the bubble, we employ a conservation of volumetric flow rate. This is done by setting the flow rate calculated at a control surface in front of the bubble equal to the flow rate at a control surface in the film.

$$Q = \int_0^R [U_l(r) - U_b] \cdot 2\pi r dr = \int_{R-\delta}^R \left[U_f + U_b\right] \cdot 2\pi r dr$$

$$\pi R^2 U_b - \int_0^R U_l(r) \cdot 2\pi r dr = -\int_{R-\delta}^R \left[U_f + U_b\right] \cdot 2\pi r dr$$

If we want the average film velocity at each z location then U_f is a function of z only. Additionally, U_b is a constant and can either be predicted or experimentally measured. The right hand side is given by,

$$-\int_{R-\delta}^R \left[U_f + U_b\right] \cdot 2\pi r dr = -\pi(U_f + U_b)(2R\delta - \delta^2)$$

Combine with the left hand side and simplify to obtain,

$$U_f = \frac{2\int_0^R U_l(r) r dr - U_b R^2}{(2R\delta - \delta^2)} - U_b$$

By integrating over the liquid velocity profile, equation (1) can be obtained.

$$U_f = \frac{(U_L - U_B)R^2}{(2R\delta - \delta^2)} - U_B$$

REFERENCES

[1] S.A. Hill, C. Kostyk, B. Motil, W. Notardonato, S. Rickman, T. Swanson, Thermal Management Systems Roadmap: Technology Area 14, 2012.

[2] M. Saito, N. Yamaoka, K. Miyazaki, M. Kinoshita, Y. Abe, Boiling two-phase flow under microgravity, Nucl. Eng. Des. 146 (1994) 451–461. doi:10.1016/0029-5493(94)90350-6.

[3] R. Lui, M. Kawaji, T. Ogushi, An experimental investigation of subcooled flow boiling heat transfer under microgravity conditions., in: 10th Int. Heat Transf. Conf., Brighton, 1994.

[4] L.B. Fore, L.C. Witte, J.B. McQuillen, Heat transfer to two-phase slug flows under reduced-gravity conditions, Int. J. Multiph. Flow. 23 (1997) 301–311. doi:10.1016/S0301-9322(96)00067-5.

[5] R.W. Rite, K.S. Rezkallah, Local and mean heat transfer coefficients in bubbly and slug flows under microgravity conditions, Int. J. Multiph. Flow. 23 (1997) 37–54. doi:10.1016/S0301-9322(96)00052-3.

[6] H. Ohta, Experiments on microgravity boiling heat transfer by using transparent heaters, Nucl. Eng. Des. 175 (1997) 167–180. doi:10.1016/S0029-5493(97)00172-6.

[7] G.P. Celata, G. Zummo, Flow Boiling in Microgravity, in: EBECEM 2008 - 1º Encontro Bras. Sobre Ebulição, Condens. E Escoamento Multifásico Líquido-Gás, Florianópolis, 2008.

[8] G. Zummo, C.M. Valencia, L. Saraceno, G.P. Celata, Flow Boiling Heat Transfer and Two-Phase Flow in Microgravity, in: Proc. 15th Int. Heat Transf. Conf., Kyoto, 2014.

[9] M. Narcy, E. de Malmazet, C. Colin, Flow Boiling in Straight Heated Tubes Under Microgravity Conditions, in: ECI 8th Int. Conf. Boil. Condens. Heat Transf., Lausanne, 2012.

[10] M. Narcy, E. de Malmazet, C. Colin, Flow boiling in tube under normal gravity and microgravity conditions, Int. J. Multiph. Flow. 60 (2014) 50–63. doi:10.1016/j.ijmultiphaseflow.2013.11.011.

[11] M. Narcy, C. Colin, Two-Phase Pipe Flow in Microgravity with and without Phase Change: Recent Progress and Future Prospects, Interfacial Phenom. Heat Transf. 3 (2015) 1–17. doi:10.1615/InterfacPhenomHeatTransfer.2015012413.

[12] D.T. Westheimer, G.P.B. Peterson, Visualization of Flow Boiling in an Annular Heat Exchanger Under Microgravity Conditions, J. Thermophys. Heat Transf. 15 (2001) 333–339. doi:10.2514/2.6612.

[13] F. Viana, R. Pardo, R. Yánez, J.L. Trallero, D.D. Joseph, Universal correlation for the rise velocity of long gas bubbles in round pipes, J. Fluid Mech. 494 (2003) 379–398. doi:10.1017/S0022112003006165.

[14] R.M. Davies, G. Taylor, The Mechanics of Large Bubbles Rising through Extended Liquids and through Liquids in Tubes, Proc. R. Soc. A Math. Phys. Eng. Sci. 200 (1950) 375–390. doi:10.1098/rspa.1950.0023.

[15] J. Fabre, A. Line, Modeling of Two-Phase Slug Flow, Annu. Rev. Fluid Mech. 24 (1992) 21–46. doi:10.1146/annurev.fl.24.010192.000321.

[16] D.J. Nicklin, J.O. Wilkes, J.F. Davidson, Two phase flow in vertical tubes, Trans. Inst. Chem. Eng. 40 (1962) 61–68.
[17] R. Collins, F.F. De Moraes, J.F. Davidson, D. Harrison, The motion of a large gas bubble rising through liquid flowing in a tube, J. Fluid Mech. 89 (1978) 497–514.
[18] E.T. White, R.H. Beardmore, The velocity of rise of single cylindrical air bubbles through liquids contained in vertical tubes, Chem. Eng. Sci. 17 (1962) 351–361.
[19] R.A.S. Brown, The mechanics of large gas bubbles in tubes: I. Bubble velocities in stagnant liquids, Can. J. Chem. Eng. 43 (1965) 217–223.
[20] A.S. Rattner, S. Garimella, Vertical upward intermediate scale Taylor flow: Experiments and kinematic closure, Int. J. Multiph. Flow. 75 (2015) 107–123. doi:10.1016/j.ijmultiphaseflow.2015.04.007.
[21] K.H. Bendiksen, On the motion of long bubbles in vertical tubes, Int. J. Multiph. Flow. 11 (1985) 797–812. doi:10.1016/0301-9322(85)90025-4.
[22] S. Polonsky, D. Barnea, L. Shemer, Averaged and time-dependent characteristics of the motion of an elongated bubble in a vertical pipe, Int. J. Multiph. Flow. 25 (1999) 795–812. doi:10.1016/S0301-9322(98)00066-4.
[23] J.B.L.M. Campos, J.R.F.G. De Carvalho, An experimental study of the wake of gas slugs rising in liquids, J. Fluid Mech. 196 (1988) 27–37. doi:10.1017/S0022112088002599.
[24] S. Nogueira, M.L. Riethmuler, J.B.L.M. Campos, a. M.F.R. Pinto, Flow in the nose region and annular film around a Taylor bubble rising through vertical columns of stagnant and flowing Newtonian liquids, Chem. Eng. Sci. 61 (2006) 845–857. doi:10.1016/j.ces.2005.07.038.
[25] H.L. Goldsmith, S.G. Mason, The movement of single large bubbles in closed vertical tubes, J. Fluid Mech. 14 (1962) 42. doi:10.1017/S0022112062001068.
[26] E.W. Llewellin, E. Del Bello, J. Taddeucci, P. Scarlato, S.J. Lane, The thickness of the falling film of liquid around a Taylor bubble, Proc. R. Soc. A Math. Phys. Eng. Sci. 468 (2011) 1041–1064. doi:10.1098/rspa.2011.0476.
[27] Y.-P. Liu, P.-Y. Wang, J. Wang, Z.-H. Du, Investigation of Taylor bubble wake structure in liquid nitrogen by PIV technique, Cryogenics (Guildf). 55-56 (2013) 20–29. doi:10.1016/j.cryogenics.2013.01.003.
[28] A.M.F.R. Pinto, M.N. Coelho Pinheiro, J.B.L.M. Campos, Coalescence of two gas slugs rising in a co-current flowing liquid in vertical tubes, Chem. Eng. Sci. 53 (1998) 2973–2983. doi:10.1016/S0009-2509(98)00121-3.
[29] M. Kawaji, J.M. DeJesus, G. Tudose, Investigation of flow structures in vertical slug flow, Nucl. Eng. Des. 175 (1997) 37–48. doi:10.1016/S0029-5493(97)00160-X.
[30] L. Shemer, a. Gulitski, D. Barnea, On the turbulent structure in the wake of Taylor bubbles rising in vertical pipes, Phys. Fluids. 19 (2007) 035108. doi:10.1063/1.2711478.
[31] G. Hetsroni, R. Rozenblit, Thermal patterns on a heated wall in vertical air–water flow, Int. J. Multiph. Flow. 26 (2000) 147–167. doi:10.1016/S0301-9322(99)00015-4.
[32] V. Babin, D. Barnea, L. Shemer, Heat Transfer Characteristics in a Slug Unit, in: IHTC14-22649, Washington D.C., 2010.
[33] V. Babin, L. Shemer, D. Barnea, Experimental investigation of the local heat

transfer in a vertical gas-liquid slug unit, in: 7th Int. Symp. Meas. Tech. Multiph. Flows, 2012: pp. 43–50. doi:10.1063/1.3694687.
[34] V. Babin, L. Shemer, D. Barnea, Local instantaneous heat transfer around a rising single Taylor bubble, Int. J. Heat Mass Transf. 89 (2015) 884–893. doi:10.1016/j.ijheatmasstransfer.2015.05.103.
[35] D. Barnea, N. Yacoub, Heat transfer in vertical upwards gas-liquid slug flow, Int. J. Heat Mass Transf. 26 (1983) 1365–1376. doi:10.1016/S0017-9310(83)80068-4.
[36] N. Brauner, D.M. Maron, Identification of the range of “small diameters” conduits, regarding two-phase flow pattern transitions, Int. Commun. Heat Mass Transf. 19 (1992) 29–39. doi:10.1016/0735-1933(92)90061-L.
[37] S.G. Kandlikar, Fundamental issues related to flow boiling in minichannels and microchannels, Exp. Therm. Fluid Sci. 26 (2002) 389–407. doi:10.1016/S0894-1777(02)00150-4.
[38] F.P. Bretherton, The motion of long bubbles in tubes, J. Fluid Mech. 10 (1961) 166–188. doi:10.1017/S0022112061000160.
[39] A.M. Jacobi, J.R. Thome, Heat Transfer Model for Evaporation of Elongated Bubble Flows in Microchannels, J. Heat Transfer. 124 (2002) 1131–1136. doi:10.1115/1.1517274.
[40] J.R. Thome, V. Dupont, a. M. Jacobi, Heat transfer model for evaporation in microchannels. Part I: presentation of the model, Int. J. Heat Mass Transf. 47 (2004) 3375–3385. doi:10.1016/j.ijheatmasstransfer.2004.01.006.
[41] M. Magnini, B. Pulvirenti, J.R. Thome, Numerical investigation of hydrodynamics and heat transfer of elongated bubbles during flow boiling in a microchannel, Int. J. Heat Mass Transf. 59 (2013) 451–471. doi:10.1016/j.ijheatmasstransfer.2012.12.010.
[42] M. Magnini, B. Pulvirenti, J.R. Thome, Numerical investigation of the influence of leading and sequential bubbles on slug flow boiling within a microchannel, Int. J. Therm. Sci. 71 (2013) 36–52. doi:10.1016/j.ijthermalsci.2013.04.018.
[43] V. Talimi, Y.S. Muzychka, S. Kocabiyik, A review on numerical studies of slug flow hydrodynamics and heat transfer in microtubes and microchannels, Int. J. Multiph. Flow. 39 (2012) 88–104. doi:10.1016/j.ijmultiphaseflow.2011.10.005.
[44] P.A. Walsh, E.J. Walsh, Y.S. Muzychka, Laminar Slug Flow - Heat Transfer Characteristics with Constant Heat Flux Boundary, in: Proc. ASME 2009 Heat Transf. Summer Conf., 2009: pp. HT2009–88428.
[45] P.A. Walsh, E.J. Walsh, Y.S. Muzychka, Heat transfer model for gas–liquid slug flows under constant flux, Int. J. Heat Mass Transf. 53 (2010) 3193–3201. doi:10.1016/j.ijheatmasstransfer.2010.03.007.
[46] B. Mehta, S. Khandekar, Measurement of local heat transfer coefficient during gas–liquid Taylor bubble train flow by infra-red thermography, Int. J. Heat Fluid Flow. 45 (2014) 41–52. doi:10.1016/j.ijheatfluidflow.2013.12.001.
[47] T.H. Kim, E. Kommer, S. Dessiatoun, J. Kim, Measurement of two-phase flow and heat transfer parameters using infrared thermometry, Int. J. Multiph. Flow. 40 (2012) 56–67. doi:10.1016/j.ijmultiphaseflow.2011.11.012.
[48] M. Al-Arabi, Turbulent Heat Transfer in the Entrance Region of a Tube, Heat Transf. Eng. 3 (1982) 76–83.
[49] S.W. Churchill, H.H.S. Chu, Correlating equations for laminar and turbulent free

convection from a vertical plate, Int. J. Heat Mass Transf. 18 (1975) 1323–1329. doi:10.1016/0017-9310(75)90243-4.
[50] F.P. Incropera, D.P. DeWitt, T.L. Bergman, A.S. Lavine, Fundamentals of Heat and Mass Transfer, 6th ed., Wiley, 2007.
[51] R.K. Shah, A.L. London, Laminar Flow Forced Convection in Ducts, in: Adv. Heat Transf., Academic Press, New York, 1978.
[52] L.P. Davis, J.J. Perona, Development of free convection flow of a gas in a heated vertical open tube, Int. J. Heat Mass Transf. 14 (1971) 889–903. doi:10.1016/0017-9310(71)90116-5.
[53] M. Narcy, A. Scammell, C. Colin, J. Kim, Flow Boiling Under Microgravity Conditions: Comparative study of two experimental data sets, in: Proc. 15th Int. Heat Transf. Conf., Kyoto, 2014: pp. IHTC15–9072.
[54] J.C. Chen, Correlation for Boiling Heat Transfer to Saturated Fluids in Convective Flow, Ind. Eng. Chem. Process Des. Dev. 5 (1966) 322–329.
[55] A. Cioncolini, J.R. Thome, Algebraic turbulence modeling in adiabatic and evaporating annular two-phase flow, Int. J. Heat Fluid Flow. 32 (2011) 805–817. doi:10.1016/j.ijheatfluidflow.2011.05.006.
[56] J.R. Taylor, An Introduction to Error Analysis, 2nd ed., University Science Books, 1982.
[57] MATLAB version 8.4 (R2014b), (2014).
[58] C. Colin, J. Fabre, A.E. Dukler, Gas-liquid flow at microgravity conditions—I. Dispersed bubble and slug flow, Int. J. Multiph. Flow. 17 (1991) 533–544. doi:10.1016/0301-9322(91)90048-8.
[59] W.S. Rasband, ImageJ, (1997). http://imagej.nih.gov/ij/.
[60] D.T. Dumitrescu, Strömung an einer Luftblase im senkrechten Rohr, ZAMM - Zeitschrift Für Angew. Math. Und Mech. 23 (1943) 139–149. doi:10.1002/zamm.19430230303.
[61] J. Ratulowski, H.-C. Chang, Transport of gas bubbles in capillaries, Phys. Fluids A. 1 (1989) 1642–1655.
[62] R.K. Edvinsson, S. Irandoust, Finite-element analysis of Taylor flow, AIChE J. 42 (1996) 1815–1823. doi:10.1002/aic.690420703.
[63] M. Kawaji, J.M. Dejesus, G. Tudose, Investigation of flow structures in vertical slug flow, Nucl. Eng. Des. 175 (1997) 37–48.
[64] L. Shemer, A. Gulitski, D. Barnea, Experiments on the Turbulent Structure and the Void Fraction Distribution in the Taylor Bubble Wake, Multiph. Sci. Technol. 17 (2005) 103–122. doi:10.1615/MultScienTechn.v17.i1-2.60.
[65] H. Lamb, Hydrodynamics, 6th ed., Dover publications, New York, 1945.
[66] M. Magnini, J.R. Thome, Computational Study of Saturated Flow Boiling Within a Microchannel in the Slug Flow Regime, J. Heat Transfer. 138 (2015) 021502. doi:10.1115/1.4031234.
[67] A. Scammell, M. Magnini, J.R. Thome, J. Kim, Heat transfer and flow characteristic of rising Taylor bubbles, in: Proc. 9th Int. Conf. Boil. Condens. Heat Transf., Boulder, 2015.
[68] A.P. Colburn, A method of correlating forced convection heat-transfer data and a comparison with fluid friction, Int. J. Heat Mass Transf. 7 (1964) 1359–1384. doi:10.1016/0017-9310(64)90125-5.

[69] J.R. Barbosa, G.F. Hewitt, A Thermodynamic Nonequilibrium Slug Flow Model, J. Heat Transfer. 127 (2005) 323. doi:10.1115/1.1857945.
[70] H.K. Forster, N. Zuber, Dynamics of vapor bubbles and boiling heat transfer, AIChE J. 1 (1955) 531–535. doi:10.1002/aic.690010425.
[71] K.R. Chun, R.A. Seban, Heat Transfer to Evaporating Liquid Films, J. Heat Transfer. 93 (1971) 391. doi:10.1115/1.3449836.
[72] A. Orell, R. Rembrand, A model for gas-liquid slug flow in a vertical tube, Ind. Eng. Chem. Fundam. 25 (1986) 196–206. doi:10.1021/i100022a004.
[73] G. Bittlinger, A. Schulz, S. Wittig, Film Cooling Effectiveness and Heat Transfer Coefficients for Slot Injection at High Blowing Ratios, in: Vol. 4 Heat Transf. Electr. Power; Ind. Cogener., ASME, The Hague, 1994: p. V004T09A032. doi:10.1115/94-GT-182.
[74] R.A. Seban, Heat Transfer and Effectiveness for a Turbulent Boundary Layer With Tangential Fluid Injection, J. Heat Transfer. 82 (1960) 303. doi:10.1115/1.3679938.
[75] Y.Y. Hsu, On the Size Range of Active Nucleation Cavities on a Heating Surface, J. Heat Transfer. 84 (1962) 207. doi:10.1115/1.3684339.
[76] A. Fershtman, L. Shemer, D. Barnea, Instantaneous heat transfer rate around consecutive Taylor bubbles, Int. J. Heat Mass Transf. 95 (2016) 865–873. doi:10.1016/j.ijheatmasstransfer.2015.12.045.
[77] T.G. Beckwith, R.D. Marangoni, J.H. Lienhard V, Assessing and Presenting Experimental Data, in: Mech. Meas., 6th ed., Pearson Education Inc., 2007: pp. 34–107.